PEPTIDE-BASED METHODS FOR ASSEMBLING AND CONTROLLING THE MORPHOLOGIES, METRICS, AND PROPERTIES OF GOLD NANOPARTICLE SUPERSTRUCTURES

By

Chen Zhang

B.S., Anhui University, 2009

Submitted to the Graduate Faculty of

the Kenneth P. Dietrich School of Arts and Sciences

in partial fulfillment

of the requirements for the degree of

Doctor of Philosophy

University of Pittsburgh

2015

UNIVERSITY OF PITTSBURGH

FACULTY KENNETH P. DIETRICH SCHOOL OF ARTS AND SCIENCES

This dissertation was presented

by

Chen Zhang

It was defended on

February 16th, 2015

and approved by

Stephen G. Weber, PhD, Professor, Department of Chemistry

Alexander Star, PhD, Associate Professor, Department of Chemistry

Bruce Armitage, PhD, Professor, Department of Chemistry, Carnegie Mellon University

Dissertation Advisor: Nathaniel L. Rosi, PhD, Associate Professor, Department of Chemistry

PEPTIDE-BASED METHODS FOR ASSEMBLING AND CONTROLLING THE MORPHOLOGIES, METRICS, AND PROPERTIES OF GOLD NANOPARTICLE SUPERSTRUCTURES

Chen Zhang, PhD

University of Pittsburgh, 2015

This dissertation describes new peptide-based methods for assembling and controlling the morphologies, metrics, and properties of gold nanoparticle superstructures. The aim of this research is to develop the peptide-based method by modifying the peptide sequences and controlling the reaction conditions for the synthesis and assembly of gold nanoparticle superstructures to achieve reliable control over their morphology and metrics, and furthermore study their properties and applications.

With this goal in mind, the C-terminus of a gold-binding peptide was modified with different numbers of hydrophobic phenylalanines to affect peptide assembly and ultimately nanoparticle assembly. The addition of hydrophobic phenylalanines to the C-terminus of peptide conjugates promoted fiber bundling which in turn lead to the formation of thick or intertwined 1-D nanoparticle superstructures. Furthermore, I prepared spherical gold nanoparticle superstructures with varied diameters (~40nm, ~75nm, and ~150nm) and visible to near-infrared optical properties by using a single peptide conjugate molecule yet varied reaction conditions. Theoretical simulation and experiment were coupled to further understand their optical properties. Finally, I studied and demonstrated the drug storage and release properties of hollow spherical gold nanoparticle superstructures; this was the first demonstrated application of this class of nanoparticle superstructure.

TABLE OF CONTENTS

LIST OF TABLES

LIST OF FIGURES

LIST OF SCHEMES

PREFACE

Acknowledgements

I would like to give my special thanks to my research advisor and mentor, Prof. Nathaniel L. Rosi for guiding and overseeing me through my Ph.D. study. Without his expertise, guidance, encouragement and patience, I would not have achieved what I have achieved and I would not be well-prepared for my future career.

I would also like to thank my committee members, Prof. Stephen G. Weber, Prof. Alexander Star, and Prof. Bruce Armitage for their continuous support and mentorship during my graduate study.

I would also like to thank Dr. Leekyoung Hwang, Dr. Chengyi Song and Dr. Tao Li for helping me when I was a junior graduate student and I would like to thank Chong Liu, Alex Spore, Andrea Merg, Tianyi Luo, Yicheng Zhou, and Ryan Ruenroeng for being great colleagues.

In addition, I would like to thank Prof. George C. Schatz and his postdoc, Dr. Yong Zhou for their collaboration in studying the optical properties of hollow spherical gold nanoparticle superstructures.

I would also like to thank Prof. Sean Garrett-Roe and his graduate student, Thomas Brinzer for their collaboration in studying the drug storage and release properties of hollow spherical gold nanoparticle superstructures.

I also need to thank all the scientists who have worked with me and/or helped to analyze my samples: Dr. Susheng Tan for facilities in NFCF; Cole M. Van Ormer and Thomas Harper for

TEM; Dr. Joel Gillespie for AFM measurements; Dr. Bhaskar Godugu for MALDI and LC-MS; Dr. Steven J. Geib for single crystal X-ray diffraction; Dr. H. Christopher Fry for the peptide synthesis.

Lastly, I would also like to thank my wife (Yang Cheng), my parents, and my younger brother for their continuous support and encouragement. I wish I could spend more time with them. Thanks for their understanding.

Thanks!

1.0 INTRODUCTION

1.1 GOLD NANOPARTICLES AND THEIR OPTICAL PROPERTIES

Nanostructures are materials that have at least one dimension within 1-100 nm. Materials confined to the nanometer size regime exhibit very different mechanical, electronic, magnetic, optical, and chemical properties compared to those of bulk materials.[1] Recently, nanoparticles composed of metals, semiconductors, or metal oxides have attracted broad interest due to their unique properties and potential applications in various areas including electronic devices,[2] bio-imaging tools,[3] drug delivery vehicles,[4] biosensors,[5] etc.

As a class of noble metal nanoparticles, gold nanoparticles can be dated as far back as the 5th century B.C. when the term "colloidal gold" was in existence, long before the development of modern gold chemistry.[6] Due to their unique optical, electronic, and catalytic properties, gold nanoparticles are the subject of substantial research.[6] One of the most interesting and powerful properties of gold nanostructures is their surface plasmon resonance (SPR).[7] When gold nanoparticles are irradiated by light of a certain wavelength, the conduction electrons of gold nanoparticles begin to oscillate, creating a dipole, which gives the so-called "dipole SPR" of gold nanoparticles.[7] **Figure 1** illustrates this phenomenon for a spherical gold nanoparticle. The SPR can be observed using UV-Vis spectroscopy. The instrument detects both scattering and absorption, which together represents the 'extinction'. The SPR creates strong electric fields close to the surface of gold nanoparticles, which can be directly applied to surface-enhanced Raman scattering (SERS).[8]

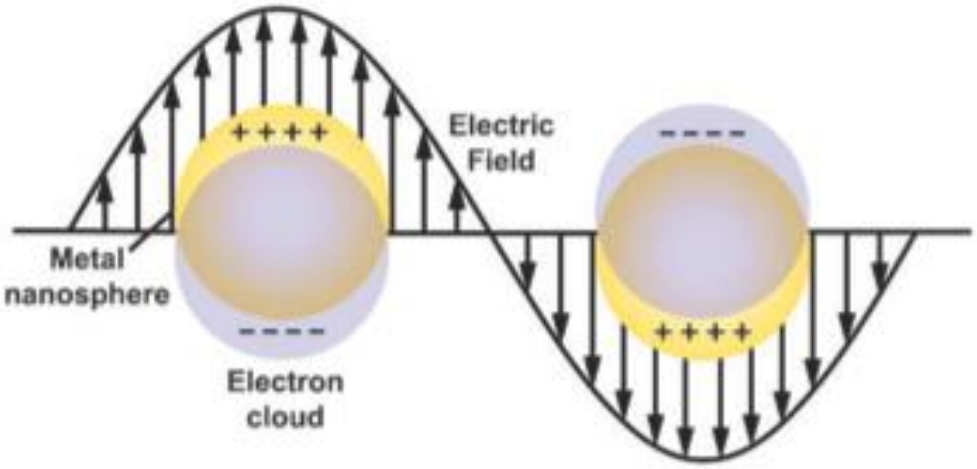

Figure 1. Surface plasmon resonance (SPR) is a critical property of gold nanostructures that results from the collective oscillation of delocalized electrons in response to an external electric field. (Adapted from ref.8).

Gold nanoparticles exhibit unique size-, shape- and composition-dependent properties. For instance, compared with the yellow color of bulk gold, gold nanospheres of diameter ~100 nm or smaller appear crimson when suspended in water, and gold nanoparticles of diameter less than ~3 nm are no longer "noble", but show catalytic properties.[6] The SPR of gold nanostructures depends on the size, shape, and morphology of the nanostructure, as well as the dielectric environment,[7] which provide a good variety of routes to control SPR response. The SPR extinction of spherical gold nanoparticles red shifts as their diameters increase. Consequently, gold nanoparticle colloidal solutions have different colors depending on their size (**Figure 2a-b**).[9] Non-spherical shaped gold nanoparticles such as rods, cubes, wires, belts, and tubes are found to possess properties dependent not only on the size but also shape.[7] Compared with spherical gold nanoparticles, gold nanorods have two distinctive peaks in their UV-Vis spectrum, which correspond to the transverse and longitudinal SPR modes (**Figure 2c-d**).[10-13] Another way to control the SPR response and introduce more properties is by tuning the

composition of gold nanoparticles, for example, preparing core-shell or alloyed structures. Tuning the shell thickness of core-shell structures or the ratio between the constituent compositions in alloy structures have a pronounced effect in their SPR response.[14,15] For instance, gold nanoshells were synthesized and developed by Halas and co-workers in the late 1990's. The SPR for these materials could be adjusted from visible to NIR region by tuning the ratio between the diameter of the whole particle and the thickness of gold nanoshell (**Figure 2e**).[15]

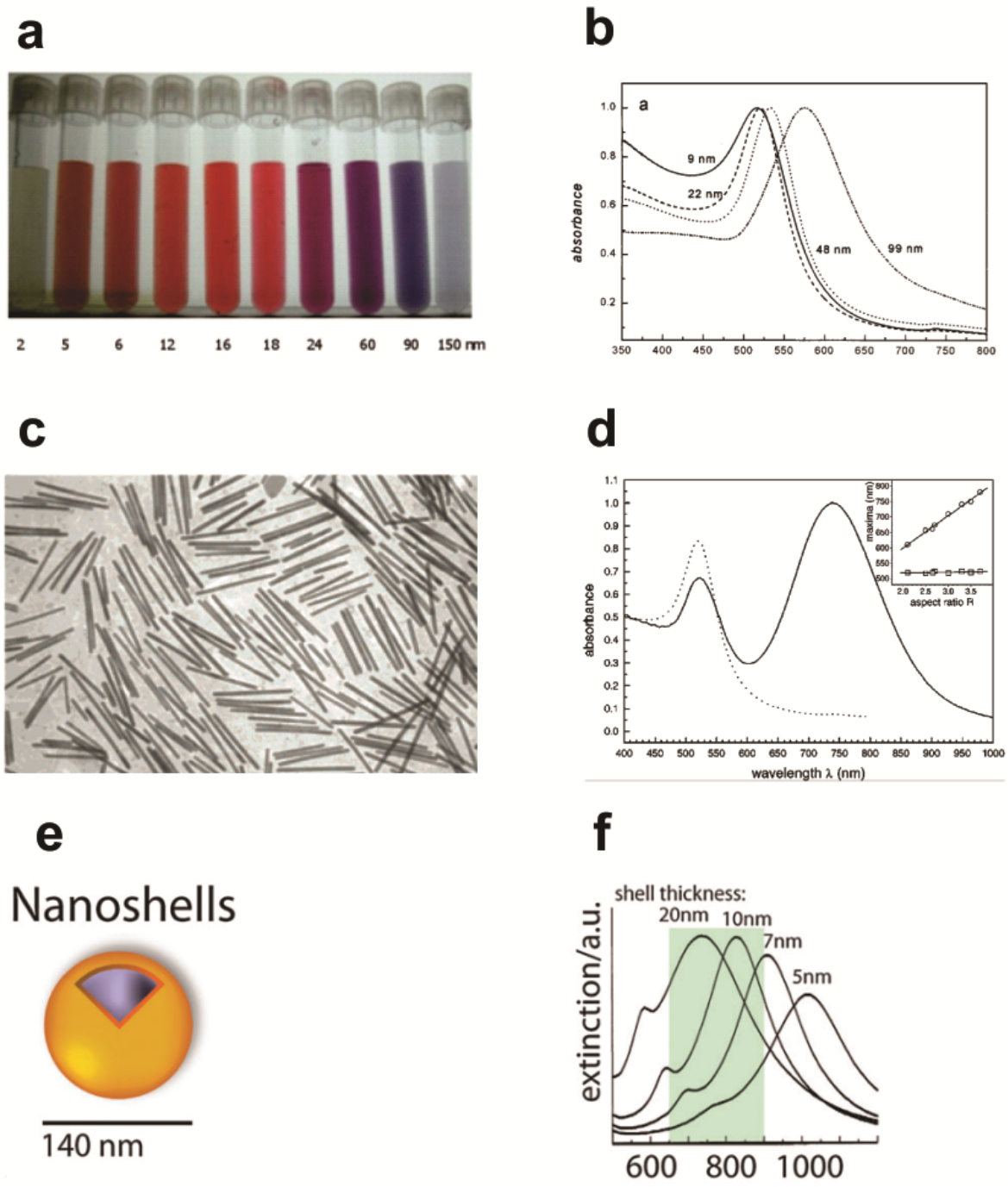

Figure 2. (a) Solutions of gold nanoparticles with different diameters and (b) UV-vis spectrum of gold nanoparticles with different diameters (Adapted from ref.9); (c) Transmission electron microscope (TEM) image of gold nanorods and (d) UV-vis spectrum of gold nanorods (Adapted from ref.10); (e) Graphical illustrations, and (f) synthetically tunable extinction spectra for gold nanoshells (Adapted from ref.14).

For biomedical applications, gold nanostructures that absorb strongly in the near-infrared (NIR) window (650–900 nm) attract the most interest, as light can penetrate deeply into tissue in this region due to the low absorption from blood and water.[16] Changes in the size can lead to a shift of the SPR band, however, to achieve strong extinction in the NIR region it is necessary to fabricate new morphologies and structures with more tunable plasmonic properties.[14] One of the general strategies utilized to shift the SPR into the NIR region is to carefully control the aspect ratio for solid structures or tune the shell thickness of hollow or core–shell structures.[17] Three widely studied types of gold nanostructures with tunable vis-NIR absorbance have been prepared: gold nanorods (**Figure 3a**),[13] gold nanoshells (**Figure 2e**),[15] and gold nanocages (**Figure 3b**)[18]. Spectral red-shifts can be achieved by increasing aspect ratio, decreasing shell thickness, and increasing gold content percent, respectively.

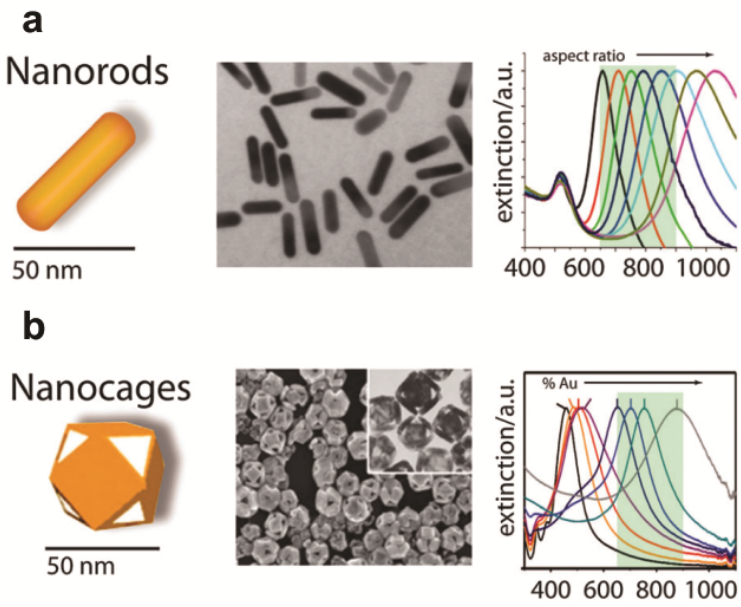

Figure 3. Graphical illustrations, transmission electron micrographs, and synthetically tunable extinction spectra for (a) gold nanorods, (b) gold nanocages. The near infrared (NIR) tissue transmission window is depicted as a green box in each of the spectra (Adapted from ref.14).

1.2 GOLD NANOPARTICLE ASSEMBLIES AND THEIR PROPERTIES

When nanoparticles are assembled together into superstructures, new collective properties emerge.[19,20] These collective properties depend not only on the size, shape, and composition of the constituent particles (building blocks), but also on how the nanoparticles are assembled, including the morphology of the assembly, particle placement, and interparticle distances. These collective properties are a result of the coupling of the excitons,[21,22] magnetic moments,[23,24] and surface plasmons[25-27] of individual nanoparticles.

It is well-known that the intrinsic properties of individual nanoparticles are mainly dominated by their size, shape, and compositions. However, when gold nanoparticles are placed close to each other within an assembly, the interparticle coupling effect becomes increasingly prominent. Besides the intrinsic properties of nanoparticles (size, shape, composition, etc.), the collective properties will be also affected by how the nanoparticles are assembled. For example, by controlling the distance between gold nanoparticles, one can tune the color from pink to violet to blue, which manifests itself as a continuing red shift in the UV-Vis spectrum.[28] Well-defined 1-D, 2-D, and 3-D assemblies of gold nanoparticles prepared from finely-controlled nanoparticle building blocks present the opportunity to optimize the properties of materials and realize new or potentially useful collective properties, leading to extensive applications in many different areas, such as optics, sensor, catalysis, biomedicine, etc.[29]

As an example of 1-D gold nanoparticle assemblies in optics, linear waveguides of 10 nm gold nanoparticles were prepared by Kuang *et al* by employing a DNA-origami-templated self-assembly (**Figure 4a-b**).[30] Using DNA origami as a template, they were able to precisely control both interparticle distances and spatial arrangement, leading to distinctive optical properties. A multi-scaffold, two-nanotube nanorail structure was used to improve the mechanical rigidity and

linearity of the waveguides. Their results demonstrated the use of DNA origami for the synthesis of relatively large and complex optical waveguides.

In the meantime, tubular assemblies of gold nanoparticles were reported for their potential as catalyst for organic reactions. Huang *et al* used gold nanoparticles stabilized by an amphiphilic pillar[5]arene to construct composite microtubes in water without any external assistance (**Figure 4c**).[31] These tubular assemblies of gold nanoparticles exhibited high stability at high temperature or in the presence of strong acid and base. More importantly, they were used to catalyze the borohydride reduction of p-nitroaniline to 1,4-diaminobenzene with a yield loss within 3% for 20 cycles.

In the area of sensors, Halas *et al* applied a convenient approach to prepare highly-ordered gold nanoparticle 2-D arrays with sub-10 nm interparticle gaps as SERS substrates (**Figure 4d-e**).[32] These interparticle gaps lead to enhanced near-field and create the so-called "hot spots" within the periodic arrays which can be utilized for large SERS enhancements. As SERS substrates, these gold nanoparticle arrays exhibited very high SERS sensitivity, long-term stability, and consistent reproducibility.

Assembling gold nanoparticles into hollow spherical superstructures is an effective way to achieve NIR extinction for biological applications. Duan *et al* fabricated biodegradable theranostic plasmonic vesicles of amphiphilic gold nanorods (**Figure 4f-h**).[33] These vesicular assemblies of gold nanorods could be either degraded by enzymes or NIR photothermal heating. Coupled with Raman probes, these nanorod assemblies gave highly active SERS signals. Furthermore, the hollow features offered opportunities for carrying anti-cancer drugs to kill targeted cancer cells. Integrated with the photothermal effect of gold nanorods, these vesicular assemblies have potential applications as theranostic materials. By using a peptide-based method,

I have successfully prepared hollow spherical gold nanoparticle superstructures. In the third and fourth chapter of this thesis, these spherical gold nanoparticle superstructures with tunable Vis-NIR extinction and their drug release properties will be discussed.

a

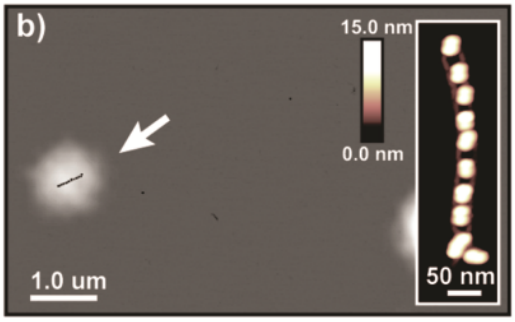
b)
15.0 nm
0.0 nm
1.0 um
50 nm

b

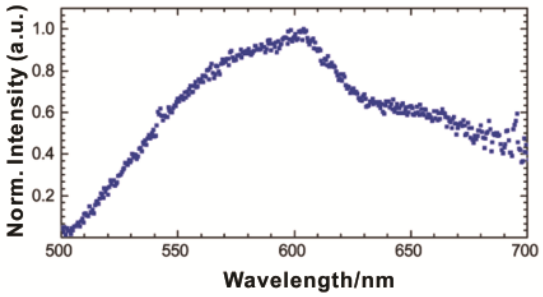
Norm. Intensity (a.u.)
1.0
0.8
0.6
0.4
0.2
500
550
600
650
700
Wavelength/nm

c

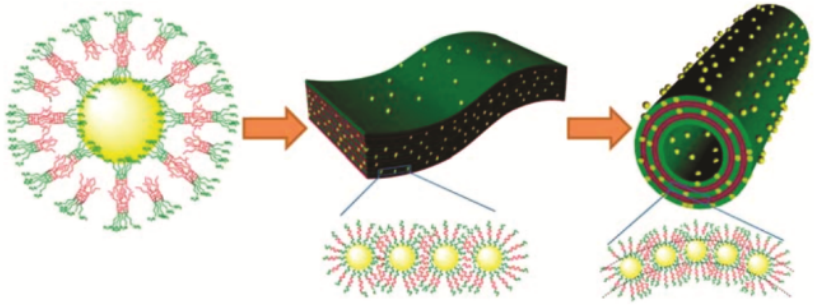

d

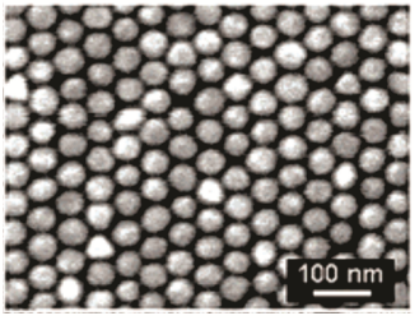
100 nm

e

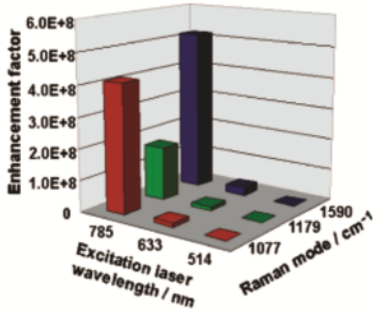
Enhancement factor
6.0E+8
5.0E+8
4.0E+8
3.0E+8
2.0E+8
1.0E+8
0
785
633
514
Excitation laser wavelength / nm
1590
1179
1077
Raman mode / cm-1

f

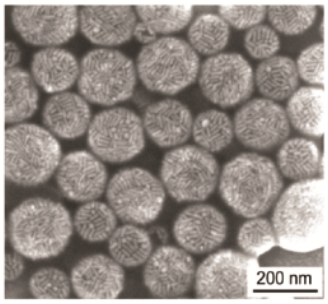
200 nm

g

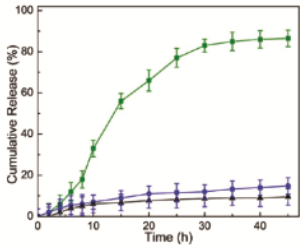
Cumulative Release (%)
100
80
60
40
20
0
0
10
20
30
40
Time (h)

h

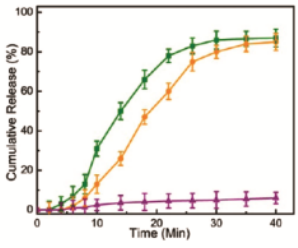
Cumulative Release (%)
100
80
60
40
20
0
0
10
20
30
40
Time (Min)

Figure 4. (a) The combined height atomic force microscope (AFM), darkfield, and magnified AFM scan of the characterized waveguides images of the waveguides and (b) the measured scattering spectra of the waveguides shown in the AFM inset (Adapted from ref.30); (c) Schematic illustration of the self-assembly process of water-soluble gold nanoparticles into self-assembled composite microtubes (Adapted from ref.31); (d) Scanning electron microscope (SEM) images of gold nanoparticle arrays and (e) Empirical SERS enhancement factors obtained on the basis of different Raman modes under different laser excitations (Adapted from ref.32); (f) SEM images of gold nanorod vesicles, (g) release profiles of drug-loaded vesicles in PBS with enzyme (green line), pH 5.0 acetate buffer (blue line), and pH 7.4 PBS (black line) and (h) release profiles of drug-loaded vesicles without (purple line) and with laser at 1.0 W/cm^2 (orange line) and 2.5 W/cm^2 (green line) for 8 min irradiation (Adapted from ref.33).

1.3 CHALLENGES IN NANOPARTOCLE ASSEMBLY

Although nanoscientists have accomplished a lot in terms of fabrication and property control of nanoparticle assemblies, there is still room for improvement and exploration. First, I still need to explore more methods for the fabrication of nanoparticle assemblies with well-defined and more complex morphologies. Second, control over the metrics of nanoparticle assemblies, such as the diameter of individual nanoparticles and the entire structure and interparticle distances remains crucial for tuning the properties. Third, more studies on nanoparticle assemblies with various and multiple compositions should be explored. By addressing these challenges, researchers would be able to understand and better control the properties of nanoparticle assemblies, and ultimately realize their potential applications. My research is mainly focused on developing new methods for controlling the morphology and metrics of gold nanoparticle superstructures and studying their properties and applications.

1.4 METHODS FOR ASSEMBLING NANOPARTICLES

Inorganic nanomaterials are typically prepared by using either a "top-down" approach or a "bottom-up" approach.[34] 'Top down' approaches offer fine control over the size, shape, and morphology and allow for control over the local order of the nanoparticles; however, they are relatively time-consuming and costly, and generally cannot be used for the construction of complex 3-D structures. In contrast, like most assembly processes in nature, the "bottom-up" approaches are simple and versatile, where building blocks are linked together through self-assembly. These building blocks can be designed precisely to facilitate the self-assembly of nanostructures with tunable features. Moreover, the "bottom-up" approaches can be used for constructing 1-D, 2-D, and very complex 3-D nanostructures.[35]

One of the most common "bottom-up" approaches is the template-based method, in which pre-assembled templates can direct the subsequent assembly of nanoparticles. Most template-based approaches require multiple synthetic steps, involving: 1) template synthesis and assembly, 2) nanoparticles preparation, and finally 3) using the template to direct the assembly of nanoparticles. Various templates can be utilized, such as carbon nanotubes,[36,37] polymers,[38] viruses[39] or biomolecules[40]. For example, Matsui *et al* have fabricated gold nanoparticle superstructures by using histidine-rich peptide nanotubes as templates. They coated these templates with monodisperse gold nanoparticles (**Figure 5**).[40]

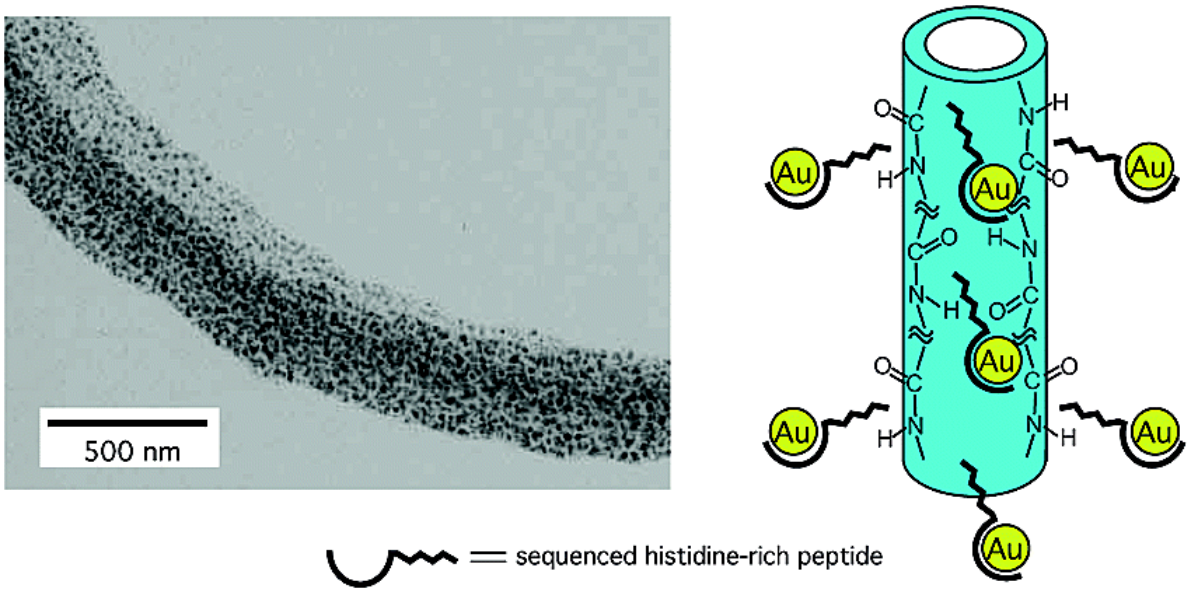

Figure 5. Fabrication of gold nanoparticle superstructure by using histidine-rich peptide nanotubes as templates (Adapted from ref.40).

Another method is to assemble nanoparticles at liquid-liquid, liquid-air, or liquid-solid interfaces using Langmuir-Blodgett techniques,[41-43] sedimentation, or evaporation[44-46]. These methods are very convenient and can be used for preparing large-scale structures. Nanoparticle assemblies with various compositions can be made using such methods. These methods can provide well-ordered assemblies. For instance, **Figure 6** shows different types of binary superlattices assembled from nanoparticles with different compositions, induced by solvent evaporation.[44]

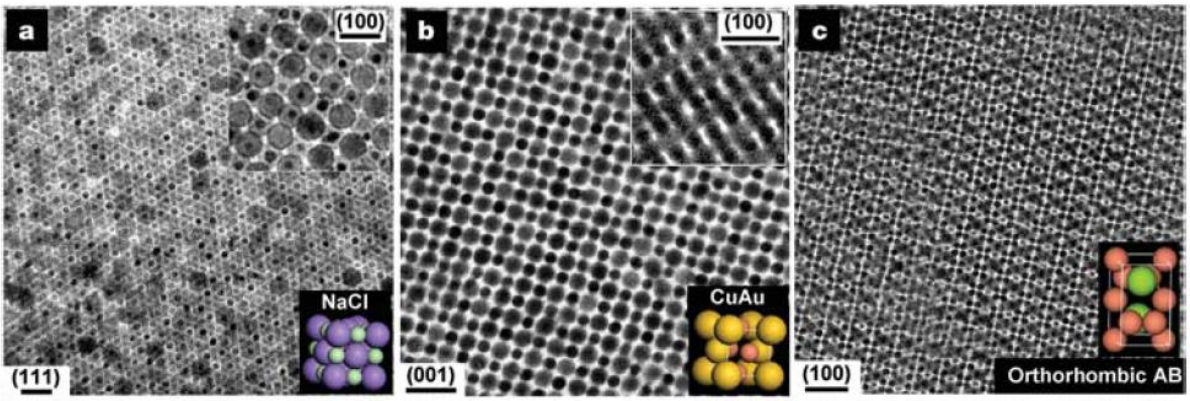

Figure 6. TEM images of the binary superlattices self-assembled from different nanoparticles and modeled unit cells of the corresponding three-dimensional structures. The superlattices are assembled from (a) 13.4 nm Fe_2O_3 and 5.0 nm Au, (b) 7.6 nm PbSe and 5.0 nm Au, and (c) 6.2 nm PbSe and 3.0 nm Pd (Adapted from ref.44).

In addition, assembly of nanoparticles can be realized under external forces, such as electric fields, magnetic fields, or light. These methods are classified as 'assisted-assembly'.[47] **Figure 7** shows chain-like assemblies of iron oxide nanoparticles aligned under a magnetic field.[48]

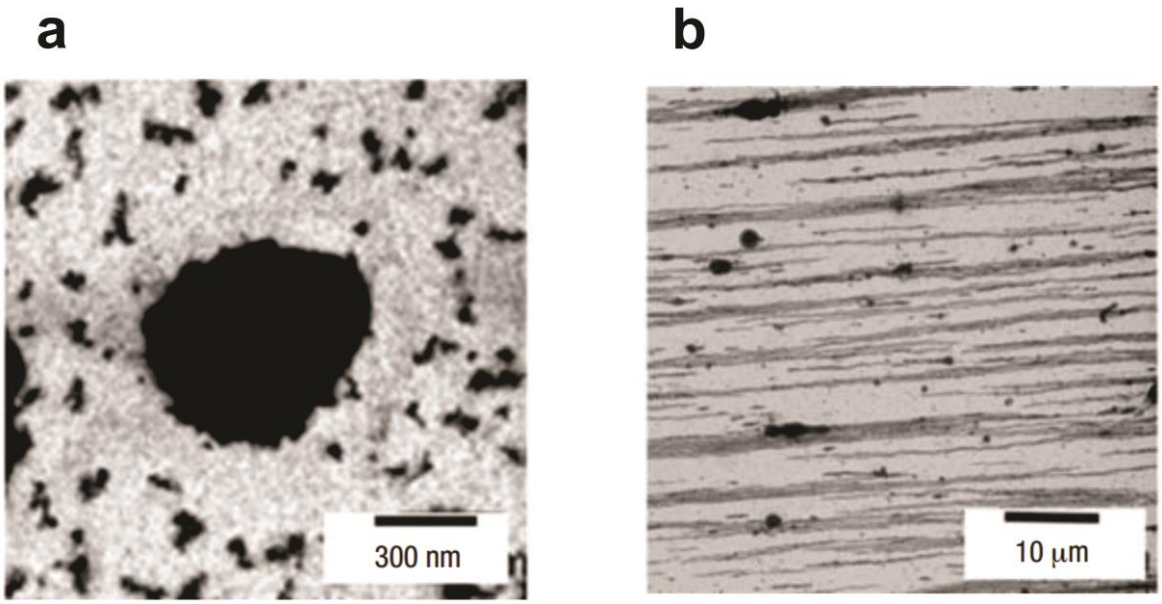

Figure 7. TEM images of nanocrystals deposited (a) without and (b) with a magnetic field form isotropic clusters during the evaporation process (Adapted from ref.48).

Many solution-based methods for assembling nanoparticles also exist and some yield well-defined nanoparticle assemblies. These assemblies are formed using dipole-dipole interactions, electrostatic interactions, steric forces, covalent or hydrogen bonding, depletion forces, hydrophobic-hydrophilic interactions, etc.[47,49] For instance, as shown in **Figure 8**, Nie *et al* prepared end-by-end or side-by-side assemblies of gold nanorods driven by the attraction between the distinct ligands attached to the long and short facets of the nanorod assemblies in different solvents.[50]

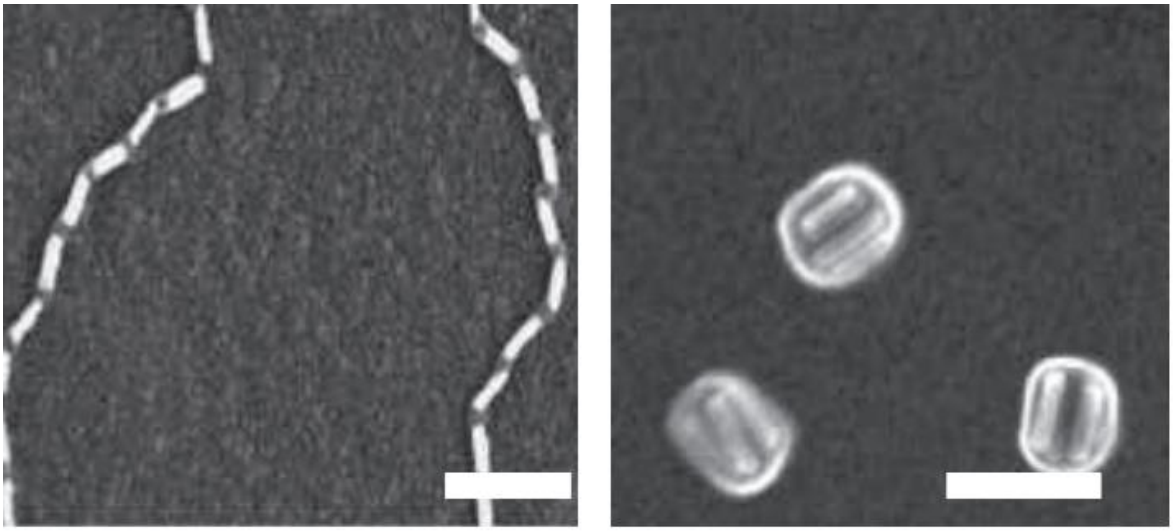

Figure 8. SEM images of self-assembly of gold nanorods end-terminated at both ends with polystyrene molecules in selective solvents in chains (left) and side-to-side aggregated bundles (right). Scale bar is 100 nm (Adapted from ref.50).

1.5 PEPTIDE-BASED METHOD FOR THE SYNTHESIS AND ASSEMBLY OF GOLD NANOPARTICLES

The control over the collective properties of nanoparticle assemblies is crucial for realizing applications, and requires precise control over the morphology, metrics and composition of nanoparticle superstructures. However, with current methodologies there still exist limitations in achieving control of nanoparticle assemblies. For instance, template-based methods yield superstructures with well-defined shapes, but often times lack control over the local order of nanoparticles. Moreover, self-assembly of nanoparticles at interfaces does not allow for the synthesis of complex multi-dimensional structures. Lastly, assisted-assembly of nanoparticles requires external driving forces and cannot target complex structures either. Therefore,

development of facile and efficient methodologies for rational design and fabrication of well-organized nanoparticle superstructures still remains challenging. Our group has developed a new peptide-based method that involves the simultaneous synthesis, growth, and assembly of nano-architectures.

Peptides exhibit unique properties that make them ideal for directing the growth and self-assembly of inorganic nanoparticles. The intrinsic structures of peptides, including their primary sequences and lengths, endow them with specific recognition capabilities and unique self-assembly capabilities.

Recognition Capabilities of Peptides. Through observations in nature or applications of phage display technology,[51] many peptides are found to have highly specific recognition capabilities, which allow them to selectively bind to specific inorganic surfaces. Peptides having high binding affinities to gold,[40,52,53] silver, [54] zinc sulfide,[55] and other inorganic materials[56-61] have already been found. In addition, computational simulation and experiment have been employed to study and assess their binding ability.[62-65]

Self-Assembly Capabilities of Peptides. In addition to their unique recognition properties, peptides also exhibit interesting self-assembly capabilities. Intrinsic structures readily drive peptides to fold into one or more spatial conformations such as α-helix and β-sheet conformations. A number of non-covalent interactions, such as hydrogen bonding, ionic interactions, van der Waals forces, hydrophobic packing (aliphatic residues) and $\pi-\pi$ stacking (aromatic residues) between residues play an instrumental role in both peptide self-assembly and stabilization of the secondary structures. Various molecules can be designed and coupled to peptides to affect self-assembly and add functionality. Such modified peptides are often called "peptide conjugates".[34] For instance, peptide amphiphiles represent a simple category of peptide

conjugate molecules designed to self-assemble. These peptide amphiphiles possess similar structure and chemical properties with lipids and surfactants. Typically, they are composed of a hydrophobic alkyl tail and hydrophilic peptide head which can self-assemble in aqueous solution to form well-defined nanostructures such as peptide bilayers, nanotubes, nanorods, nanoribbons, fibers, vesicles, and micelles (**Figure 9**).[66-69] When these molecules assemble in water, they generally form highly ordered structures with hydrophobic alkyl tails in the core and hydrophilic peptides in the exterior.[70,71]

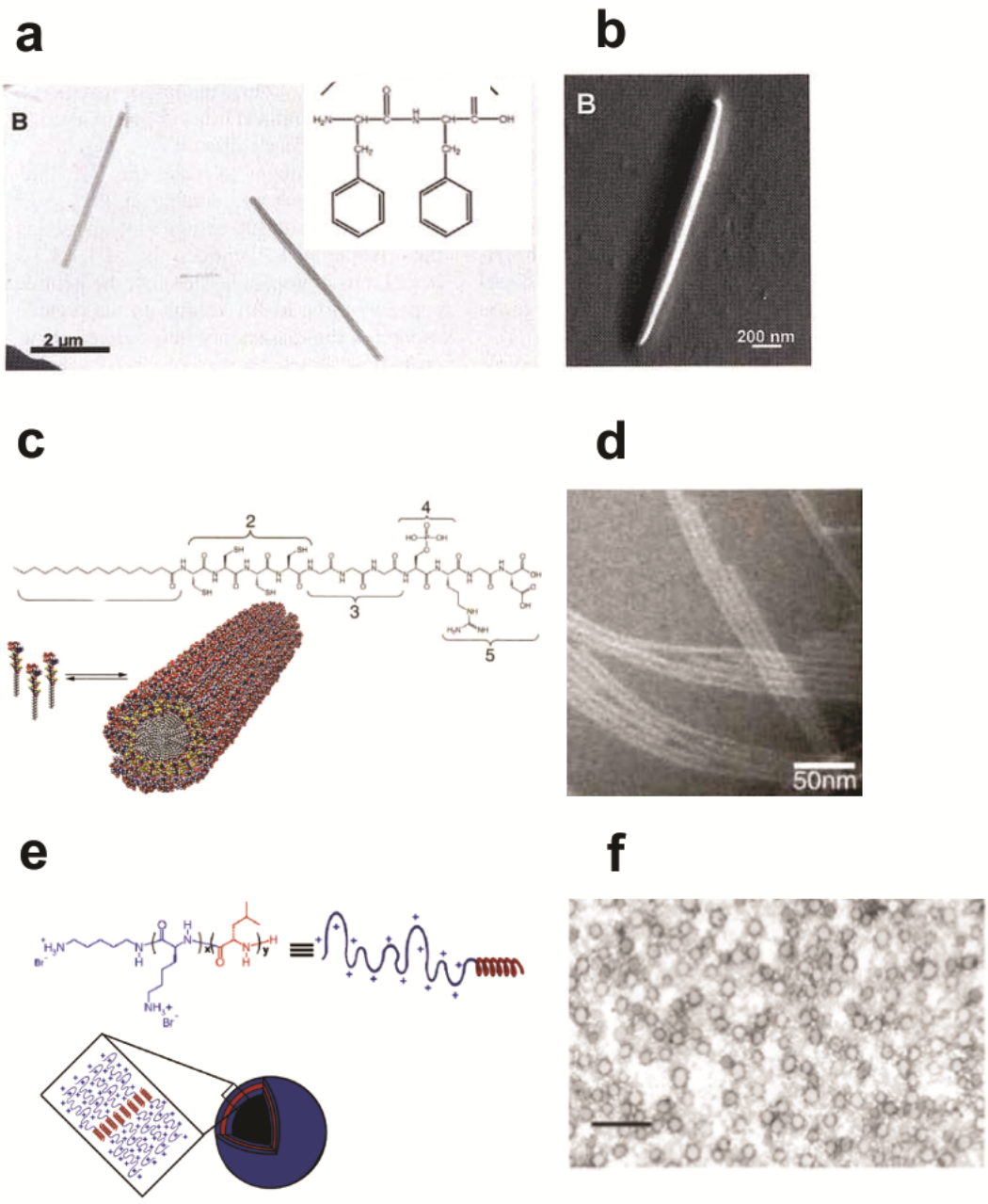

Figure 9. (a) Negatively stained TEM image and (b) SEM image of nanotubes formed by diphenylalanine peptide (Adapted from ref.66); (c) Chemical structure and schematic showing the self-assembly of peptide amphiphile molecules into a cylindrical micelle, and (d) TEM image of the fibers formed by peptide amphiphile molecules (Adapted from ref.67); (e) Schematic drawing showing proposed self-assembly of $K_{60}L_{20}$ into vesicle and (f) negatively stained TEM image of $K_{60}L_{20}$ vesicles (the scale bar is 350 nm) (Adapted from ref.69).

The Rosi Group has developed a new peptide-based method, which aims to address the challenges of nanoparticle assembly by promoting the simultaneous synthesis, growth and assembly of nanoparticles. The group began with attaching a hydrophobic aliphatic tail (C_{12} = $C_{12}H_{23}O$) to a specific gold-binding peptide (PEP_{Au} =AYSSGAPPMPPF),[59] and developed a one-pot reaction to prepare 1-D double-helical gold nanoparticle superstructures with precise local order (**Figure 10**). It is hypothesized that the self-assembly of the peptide and the growth of gold nanoparticles are coupled into a simultaneous process.[53,72] After this initial result, the group demonstrated the careful control over the metrics of the double helical gold nanoparticle superstructures (e.g. the size and density of the nanoparticles within the assembly, and interhelical distances) by tuning the synthetic conditions.[72] In a later report, the group prepared double-helical gold nanoparticle superstructures with controllable handedness and structural metrics, and revealed their tailorable chirooptical properties by coupling theoretical simulation and experimental measurement.[73] These studies illustrate the utility of our peptide-based method for designing and preparing complex plasmonic materials with tailorable structural metrics and chirooptical properties.

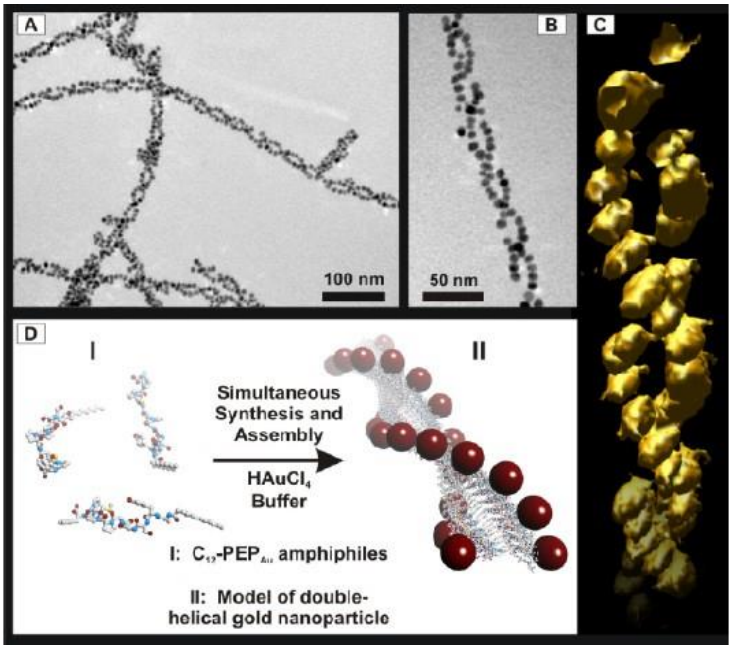

Figure 10. (a) and (b) TEM images of left-handed gold nanoparticle double helices; (c) Tomographic 3-D reconstruction image of left-handed gold nanoparticle double helices; (d) Schematic view of the formation of left-handed gold nanoparticle double helices (Adapted from ref. 53).

In addition to the 1-D gold nanoparticle superstructures, hollow spherical gold nanoparticle superstructures were also prepared in a similar manner. In 2010, the group reported that C_6-AA-PEP_{Au} conjugates (C_6 = $C_6H_{11}O$, A = alanine) could direct the synthesis and assembly of hollow spherical gold nanoparticle superstructures **(Figure 11a**).[74] These structures consisted of a monolayer shell of ~8 nm gold nanoparticles around a vesicular self-assembled peptide conjugate core. After this initial report, the group demonstrated that BP-A_x-PEP_{Au} ($C_{12}H_9CO–A_x–$AYSSGAPPMPPF; x = 2 or 3; BP = biphenyl) could also direct the formation of hollow spherical gold nanoparticle superstructures with controllable diameters (large, >100 nm or small, ~30 nm) by tuning the number of additional alanine residues at the N-terminus (2 or 3)

(**Figure 11b**).[75] Unique features of these spherical structures include their small diameter and hollow interior, which suggest their potential application in biomedicine.

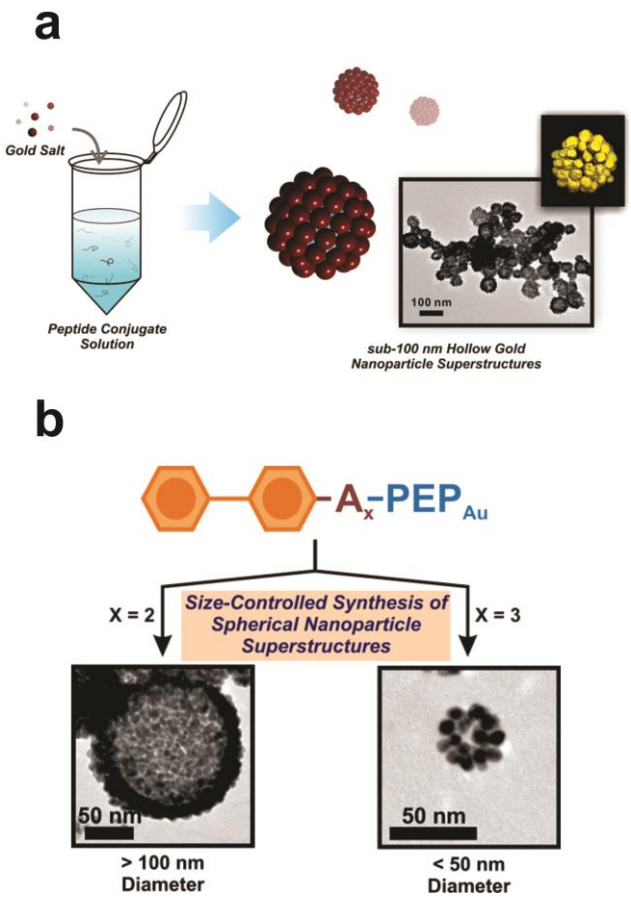

Figure 11. (a) Synthetic scheme and TEM images for spherical gold nanoparticle superstructures using C_6-AA-PEP_{Au} (Adapted from ref.74); (b) Synthetic scheme and TEM images for spherical gold nanoparticle superstructures using C_6-AA-PEP_{Au} (Adapted from ref.75).

1.6 RESEARCH OBJECTIVES

The Rosi Group have already demonstrated that the new peptide-based method can be used to construct gold nanoparticle superstructures with various morphologies and controlled metrics. However, several research directions remain unexplored. For example, all the gold nanoparticle superstructures previously reported were prepared by using peptides modified at their N-terminus. Modification of the peptide at the C-terminus could have a dramatic effect on the assembling behaviour of the peptide conjugate molecules and in turn lead to the assembly of nanoparticle superstructures with new morphologies. In addition, the hollow spherical gold nanoparticle superstructures previously synthesized are not suitable for studying their optical properties due to the low yield. Furthermore, using this class of spherical assemblies for real applications is an attractive research direction. Therefore, the objectives of this dissertation are as follows: 1) preparation of peptide conjugate molecules with C-terminal modifications and using them for the synthesis of gold nanoparticle superstructures; 2) preparing high quality spherical gold nanoparticle superstructures, systematically adjusting their structural metrics, and exploring their optical properties; and 3) using spherical gold nanoparticle superstructures as cargo carriers and studying their drug release properties.

2.0 PEPTIDE CONJUGATES FOR DIRECTING THE MORPHOLOGY AND ASSEMBLY OF NANOPARTICLE SUPERSTRUCTURES

A portion of this work, written in collaboration with Chengyi Song, H. Christopher Fry, and Nathaniel L. Rosi*, was published in *Chem. Eur. J.* 2014, *20*, 941.

2.1 INTRODUCTION

Inorganic nanoparticles are important structural and functional building blocks for the assembly of new advanced materials.[6,12,34,47,76-82] Any given material may have a hierarchy of structural and functional domains, including, for example, nanoparticles, nanoparticle superstructures, and finally assemblies of nanoparticle superstructures. Controlling each level of this hierarchy is essential for controlling material properties and, ultimately, application. Numerous methods exist for preparing discrete nanoparticles of various size, shape, and composition,[6,12,76-78] and the number of viable methods for carefully assembling nanoparticles into nanoparticle superstructures is rapidly growing.[34,47,79-82] Ideally, nanoparticle assembly methods should permit control over each level of a material's structural hierarchy: i) the size, shape, and composition of the nanoparticle building blocks; ii) the metrics, shape, and topology of the nanoparticle superstructure; and iii) the co-assembly of the nanoparticle superstructures into larger scale

structures. In this chapter, I present assembly methods that address i)-iii) in the context of constructing and assembling 1-D gold nanoparticle superstructures.

The Rosi Group has developed synthetic methods that utilize peptide conjugate molecules to direct the simultaneous synthesis and assembly of inorganic nanoparticles.[53,72-75,83,84] The peptide conjugates consist of a peptide having a particular sequence of amino acids for binding to a specific inorganic surface[34,51] and a particular organic moiety attached to the peptide N-terminus that influences peptide assembly. Such peptide conjugates can be used to prepare a diverse collection of complex nanoparticle assemblies having well-defined structures with tailorable shapes, metrics, and properties.[53,72-75,83,84] One can make numerous modifications to the peptide conjugate molecule (**Scheme 1**) that may affect its assembly. Existing modifications include: i) incorporating structure-directing moieties, such as peptide sequences that induce α-helix[85] or β-sheet[86] conformations; ii) attaching stimuli-responsive groups, such as those responsive to oxidation or reduction,[87] metal ions,[88-90] pH,[91] light,[92] and temperature[93], to induce structure assembly. For example, Pires *et al.* reported a collagen triple helical peptide modified with a His_2 moiety at the C-terminus and a nitrilotriacetic acid unit at the N-terminus. This peptide conjugate can rapidly and reversibly assemble with the addition of metal ions.[94] However, almost all of these modifications aim to influence the intermolecular interaction; few examples exist for controlling the interaction between preformed assemblies and lead to the subsequent co-assembly of these assemblies into larger-scale structures. Studies that explore how modifications to the peptide backbone affect the morphology of *nanoparticle superstructures* are not common, with the exception of prior work from the Rosi Group (*vide infra*).

Much of the previous work in the Rosi Group has focused on modifying the N-terminus with various aliphatic carbon chains or π-conjugated molecules, such as C_{12} carbon chain

($C_{12}H_{23}O$-) and biphenyl group (**R** in **Scheme 1**).[53,74,75,83,84] One can also modify the peptide sequence, provided that these modifications do not alter the peptide's inorganic recognition sequence and therefore its inorganic binding capabilities. Along these lines, prior group members have introduced alanine residues to the N-terminus ($\mathbf{X_m}$ in **Scheme 1**) of a gold-binding peptide (PEP_{Au} = AYSSGAPPMPPF)[52] and shown how these additional amino acids influence peptide conjugate assembly and ultimately nanoparticle superstructure assembly.[74,75] When such conjugates are allowed to assemble in aqueous conditions, the hydrophobic organic molecule and the amino acids at the N-terminus are expected to locate in the core of the peptide assembly while the bulk of the peptide and its C-terminus are expected to locate on the surface of the assembly, exposed to the aqueous buffer solution.[67,95-98] Based on this assembly paradigm, I predict that modifications to the C-terminus ($\mathbf{Y_n}$ in **Scheme 1**) should significantly affect conjugate assembly and possibly lead to new nanoparticle superstructures.

Scheme 1. Illustration of a peptide conjugate detailing the different potential regions for modification: **R** = organic tails; $\mathbf{X_m}$ and $\mathbf{Y_n}$ = additional amino acids; $\mathbf{PEP_{Au}}$ = AYSSGAPPMPPF.

Previously, the Rosi group demonstrated that C_{12}-PEP_{Au} (PEP_{Au} having a C_{12} chain attached to its N-terminus; C_{12} = $C_{12}H_{23}O$) assembles into 1-D twisted fibers and directs the synthesis and assembly of left-handed gold nanoparticle double-helical superstructures.[53] These helical superstructures exhibit plasmonic circular dichroism properties,[73] which could ultimately be useful for the preparation of chiral metamaterials,[99,100] provided that individual double helices

could be aggregated together into an extended array. It is well-established that hydrophobic F residues can impact peptide assembly in aqueous conditions,[101,102] and that F_2 alone, for example, assembles into nanotubular structures.[66] My hypothesis in this work is that the addition of extra phenylalanine (F) residues to the C-terminus of C_{12}-PEP_{Au} could promote inter-fibril interactions in buffer that would lead to the formation of fiber bundles, which could in turn serve to direct the formation of thick linear nanoparticle superstructures or possibly even bundles of double-helical superstructures. Thus, the C-terminus might potentially be used as a handle for controlling the co-assembly of 1-D nanoparticle superstructures into larger scale structures.

2.2 RESULTS AND DISCUSSION

To explore this hypothesis, I designed the following series of peptide conjugate molecules: C_{12}-AYSSGAPPMPP (**1**), C_{12}-AYSSGAPPMPPF (**2**),[53] C_{12}-AYSSGAPPMPPFF (**3**), and C_{12}-AYSSGAPPMPPFFF (**4**). I first studied the assembly of these peptide conjugates in 0.1 M HEPES buffer (pH= 7.3 ± 0.1; HEPES = 4-(2-hydroxyethyl)-piperazineethanesulfonic acid). I dissolved samples of **1**-**4** in 0.1 M HEPES to yield 150 μM peptide conjugate solutions, which were allowed to sit at room temperature for various specific time periods (30 min, 1 day, 3 days, and 7 days). After these time periods, I spotted transmission electron microscopy (TEM) grids with samples from each solution, applied a phosphotungstic acid stain, and then imaged each sample via TEM to monitor the progress of assembly (**Figure 12**). Several general conclusions can be drawn from the microscopy data. First, after a short incubation period (30 min), no assembly is observed for **1**, while **2** and **3** both assemble into spherical structures (diameter of **2** = 21.3 ± 3.4 nm, based on 100 counts; diameter of **3** = 21.0 ± 3.8 nm, based on 100 counts), and

4 assembles into 1-D fibers (width = 6.5 ± 0.8 nm, based on 100 counts) (see **Figure 13** for distribution diagrams). With increasing time, **1**-**4** all form fibers. For each conjugate, I observed an increasing number of fibers with increased incubation time, and also with increasing number of C-terminal F residues. Finally, I observed fiber bundling for both **2** and **3** after longer incubation times in HEPES buffer. Significant bundling for **3** was first observed after 1 day, and many thick bundles (width = 35.7 ± 12.4 nm) were observed after 1 week, as observed by both TEM (**Figure 12**) and tapping-mode atomic force microscopy (AFM) studies (**Figure 14**). The AFM data reveal fiber bundles having a height of ~20 nm, which indicates that these bundles are intertwined fibers rather than thick flat sheets of individual fibers. **2** required a longer incubation time to form bundles: significant fiber bundling was only observed after 3 days and after 1 week the bundling was not nearly as significant as **3**. **4**, which contain 3 terminal F residues, forms fibers most rapidly, and some of these fibers bundle together; however, fewer and thinner fiber bundles were observed for **4** than **3**. Since **4** rapidly assembles into fibers, the fibers may precipitate from solution before having sufficient time to interact with each other during assembly to allow formation of large quantities of fiber bundles.

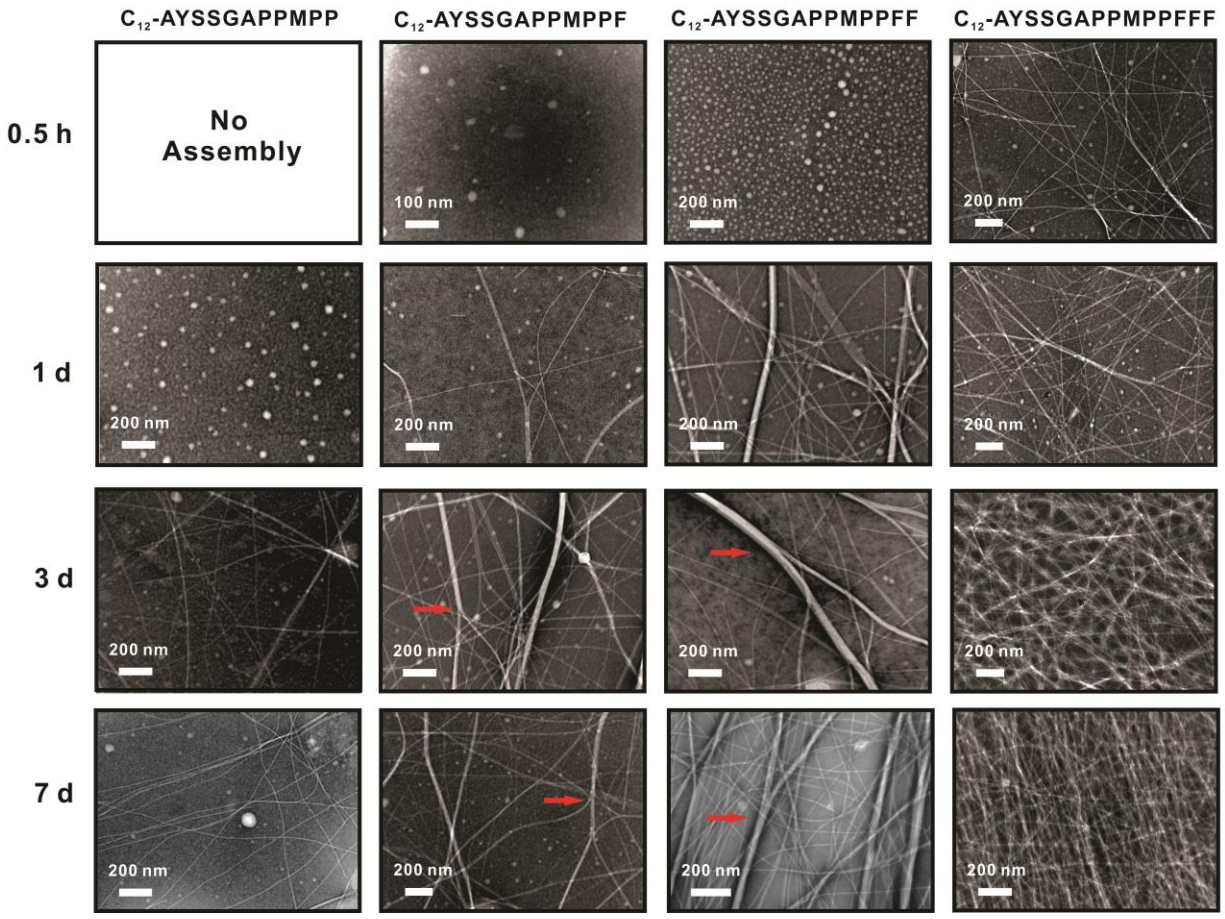

Figure 12. TEM images of soft assemblies prepared using peptide conjugates **1**, **2**, **3**, or **4** in HEPES buffer at different time points (0.5 h, 1 d, 3 d, and 7 d). Arrows indicate points where individual or thin fibers merge to form thick fiber bundles.

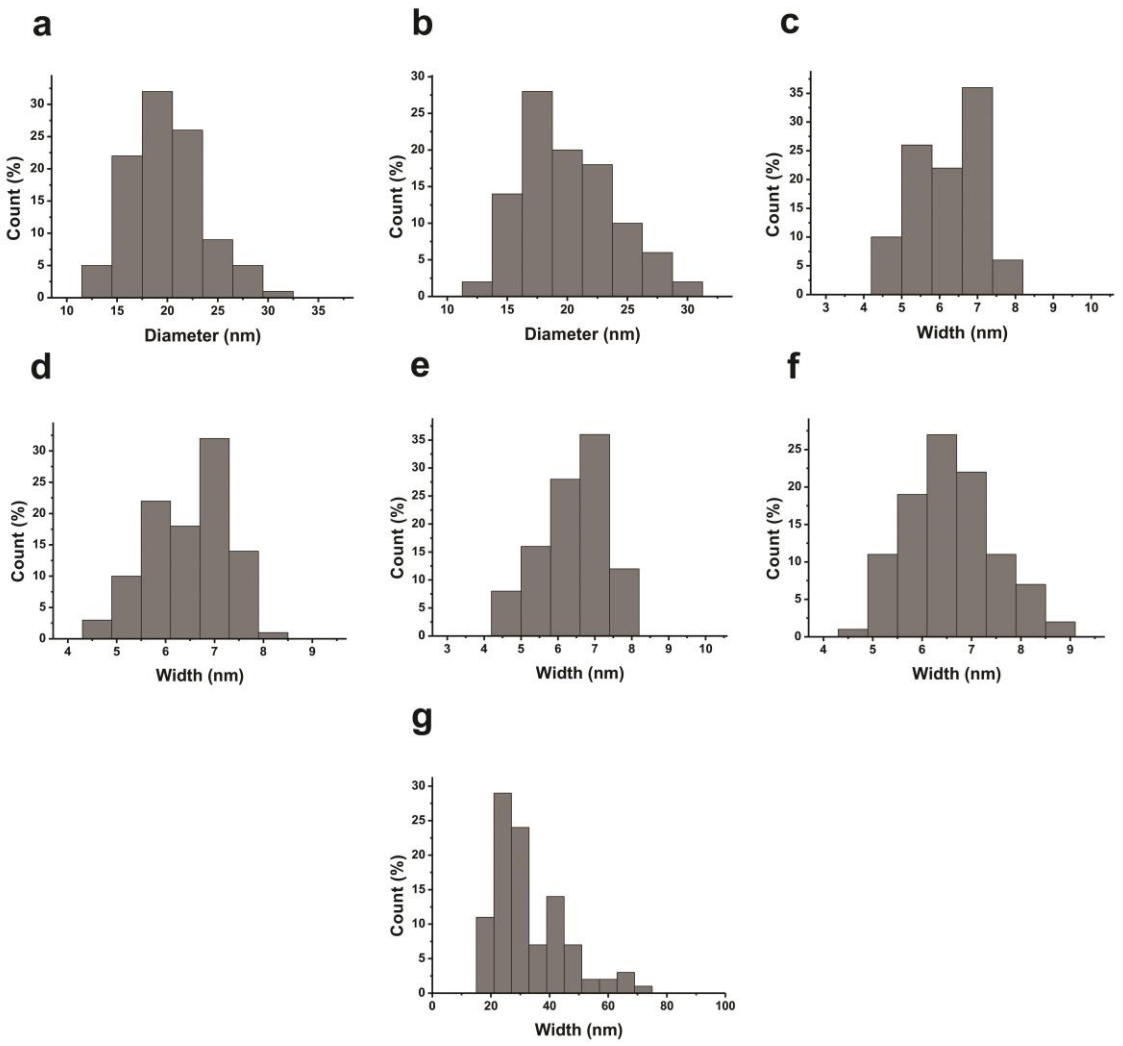

Figure 13. Diameter (spheres) or width (fibers or fiber bundles) distribution of all soft assemblies. (a) Diameter distribution of small spherical assemblies of **2**: 21.3 ± 3.4 nm, based on 100 counts; (b) Diameter distribution of small spherical assemblies of **3**: 21.0 ± 3.8 nm, based on 100 counts; (c) Width distribution of fibers formed using **1**, 6.6 ± 0.8 nm, based on 100 counts; (d) Width distribution of fibers formed using **2**, 6.7 ± 0.9 nm, based on 100 counts; (e) Width distribution of fibers formed using **3**, 6.8 ± 0.8 nm, based on 100 counts; (f) Width distribution of fibers formed using **4**, 6.5 ± 0.8 nm, based on 100 counts; (g) Width distribution of thick bundles using **3**, 35.7 ± 12.4 nm, based on 100 counts.

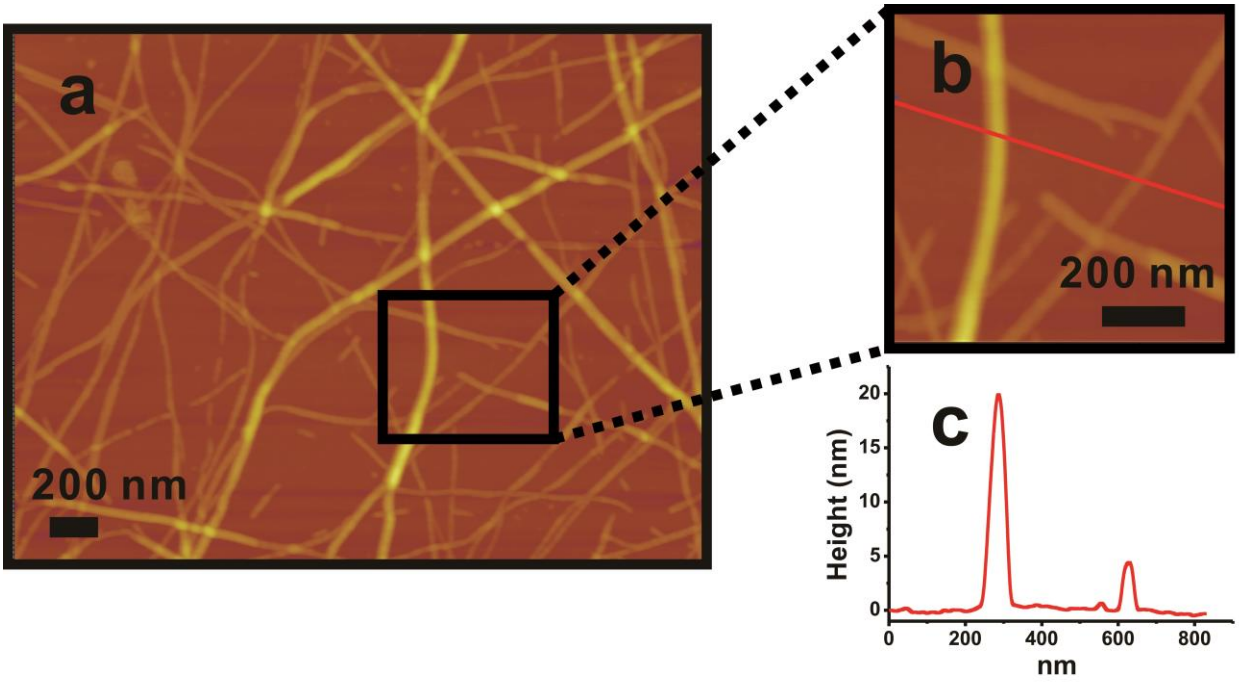

Figure 14. Tapping-mode AFM image for fibers formed using peptide conjugate **3** (a, b are height images and c is the cross-section analysis). The AFM data reveal fiber bundles having a height of ~20 nm, which indicates that these bundles are intertwined fibers rather than thick flat sheets of individual fibers.

The peptide conjugate assembly studies detailed above were performed in the absence of gold salt, an integral component of our nanoparticle superstructure syntheses.[53,72-75,83] From previous studies, it is known that Au^{3+} (as well as other multivalent cations, such as Ca^{2+}) can significantly accelerate and affect peptide conjugate assembly.[53,89,90,103] Once gold salts are added to solutions of peptide conjugates in HEPES, however, fiber growth rapidly occurs and gold nanoparticles form and assemble along with the peptide conjugates into gold nanoparticle superstructures, because HEPES can reduce Au^{3+} to Au^{0}.[52,104] The gold nanoparticle superstructures can obscure observation of conjugate assembly. Therefore, in order to study conjugate assembly in the presence of metal cations, I added 1.5 μL of 0.1 M calcium chloride to

150 μM solutions of **1**-**4** in 125 μL 0.1 M HEPES (**Figure 15**). After incubating for 30 min at room temperature with added Ca^{2+}, **1**-**4** each formed fibers. The degree of fiber formation increased with increasing number of C-terminal F residues and, again, some bundling was observed for **2** and **3**, with **3** exhibiting much more significant bundling than **2**. These results mirror what was observed after 7 day incubation without Ca^{2+}, which suggests that increasing the ionic strength by adding Ca^{2+} accelerates the assembly process. I anticipated that assembly of **1**-**4** in the presence of Au^{3+} would be similar to their assembly in the presence of Ca^{2+}.

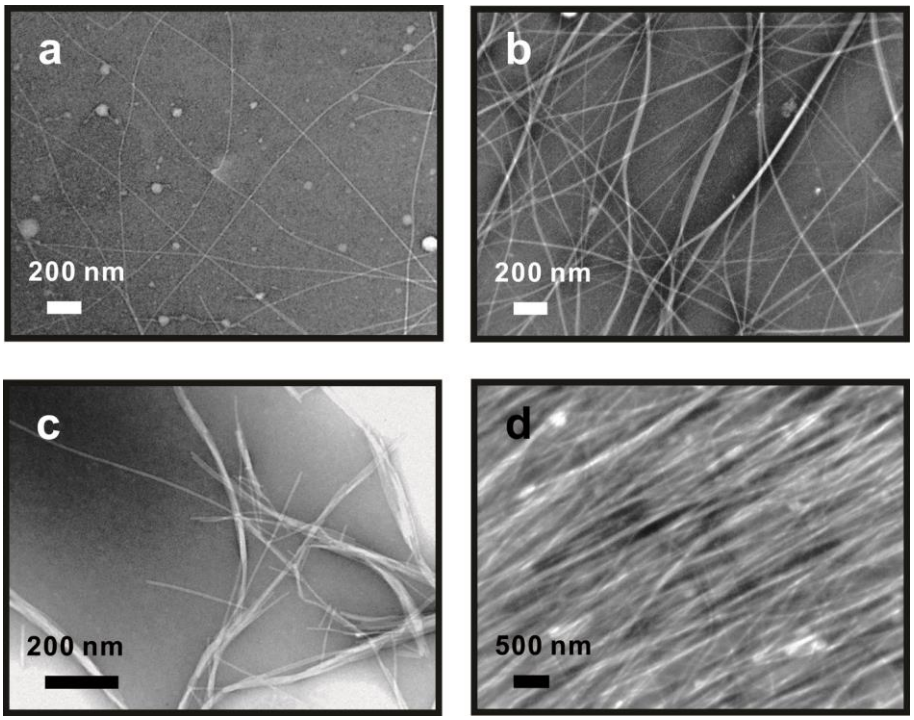

Figure 15. Negative Stained TEM images of peptide conjugates **1** (a), **2** (b), **3** (c), or **4** (d) incubating in HEPES buffer for 30 min in the presence of Ca^{2+}.

Having established that the addition of C-terminal F residues significantly affects fiber assembly and bundling, I next proceeded to explore the impact of these modifications on nanoparticle superstructure formation in the presence of gold salt. For these studies, I followed the group's established synthetic protocol.[53] 1 μL of a chloroauric acid solution (0.1 M $HAuCl_4$ in 1.0 M TEAA; TEAA = triethylammonium acetate) was added to a solution of peptide conjugate (**1**-**4**) in 0.1 M HEPES buffer. After incubating these solutions for 1 day at room temperature, the reaction products were imaged using TEM (**Figure 16**-**20**). **1** yielded aggregates of 1-D gold nanoparticle superstructures (**Figure 16a** and **Figure 17**, width: 24.1 ± 4.1 nm, based on 100 counts; nanoparticle diameter: 8.1 ± 1.3 nm, based on 100 counts), while **2** yielded well-defined gold nanoparticle double helices, as previously reported (**Figure 16b** and **Figure 18**, width: 20.1 ± 1.8 nm, based on 100 counts; nanoparticle diameter: 7.3 ± 1.4 nm, based on 100 counts). **3** yielded thick, branched 1-D nanoparticle superstructures (**Figure 16c** and **Figure 19**, width: 61.4 ± 15.7 nm, based on 100 counts; nanoparticle diameter: 6.3 ± 1.2 nm, based on 100 counts). **4** resulted in thin intertwined 1-D nanoparticle superstructures (**Figure 16d** and **Figure 20**, width: 20.5 ± 4.9 nm, based on 100 counts; nanoparticle diameter: 6.0 ± 1.1, based on 100 counts). These results are illustrated and summarized in **Scheme 2**.

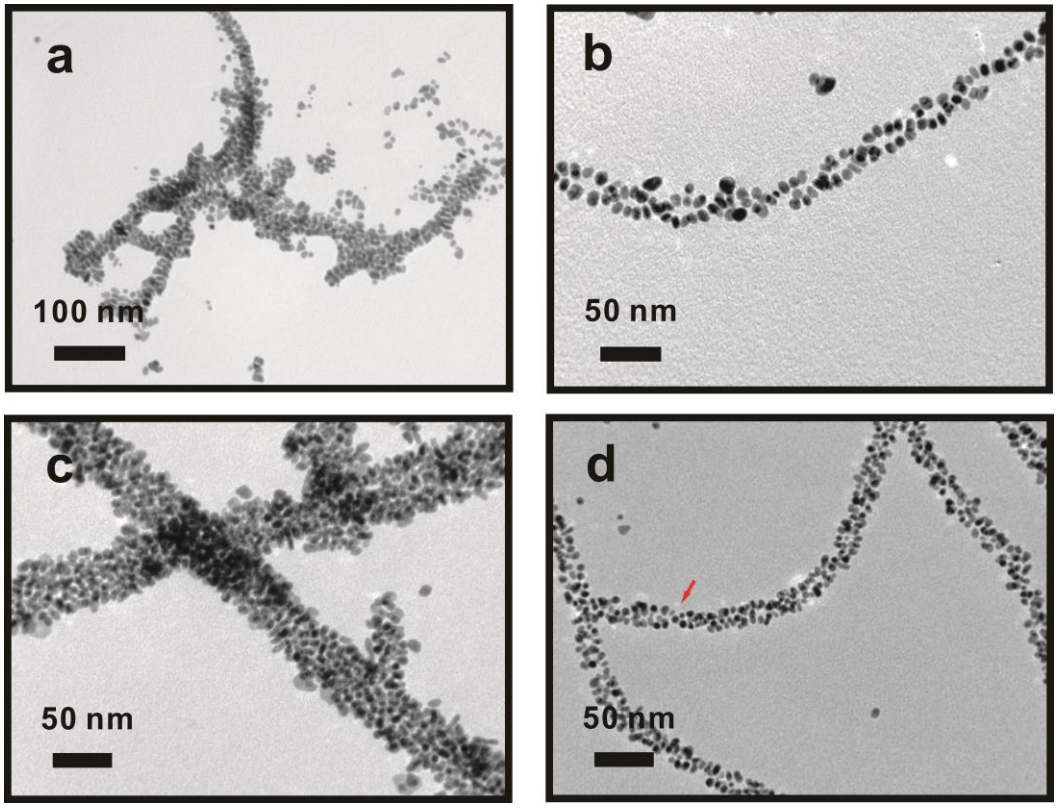

Figure 16. Zoomed-in TEM images of nanoparticle superstructures formed using peptide conjugates **1** (a), **2** (b), **3** (c), and **4** (d). Red arrows indicate the regions of the structure that appear to exhibit a helical arrangement of the nanoparticles.

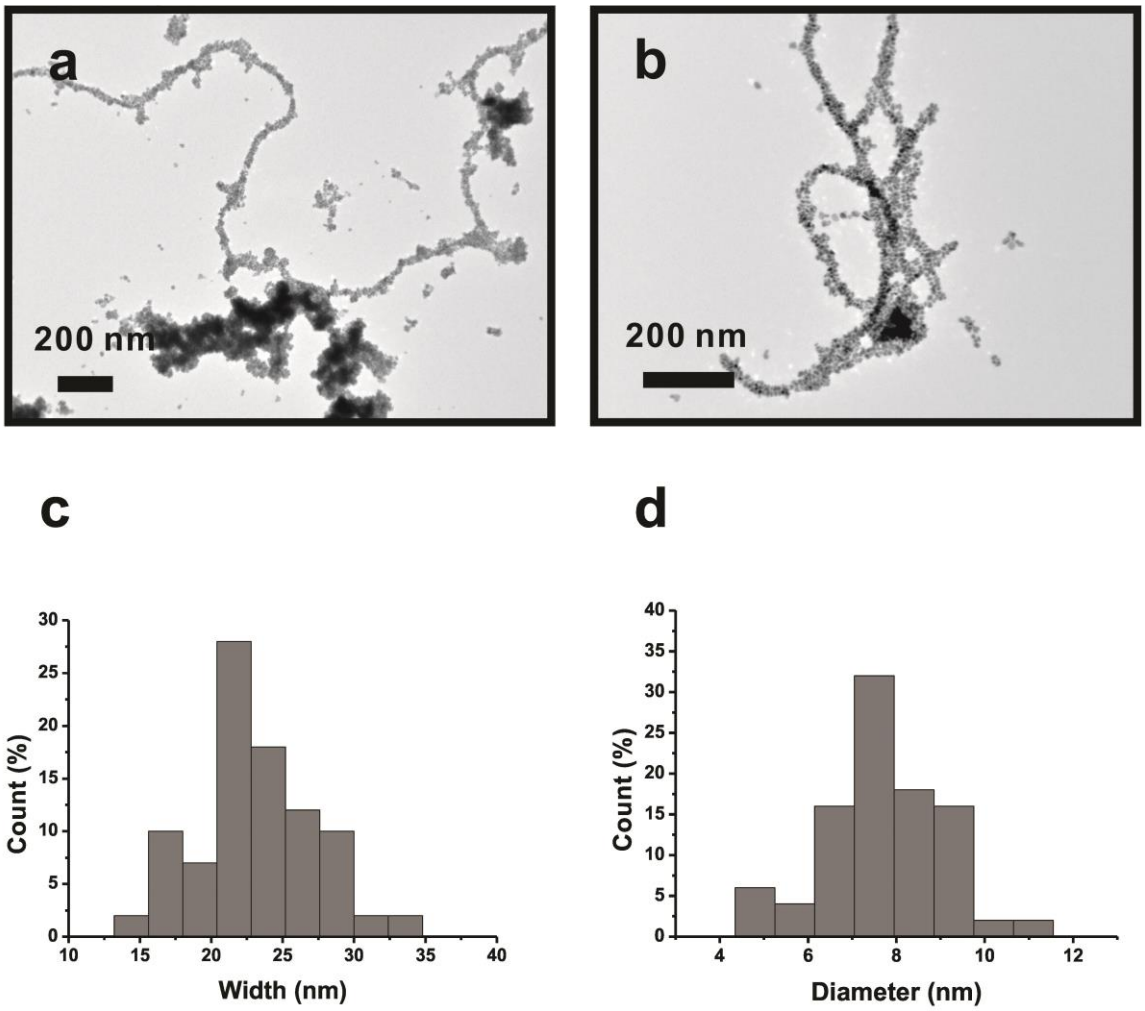

Figure 17. (a-b) TEM images of aggregates of 1-D gold nanoparticle superstructures formed using **1**; (c) Width distribution of superstructures: 24.1 ± 4.1 nm, based on 100 counts; (d) Diameter distribution of gold nanoparticle within the superstructures: 8.1 ± 1.3 nm, based on 100 counts.

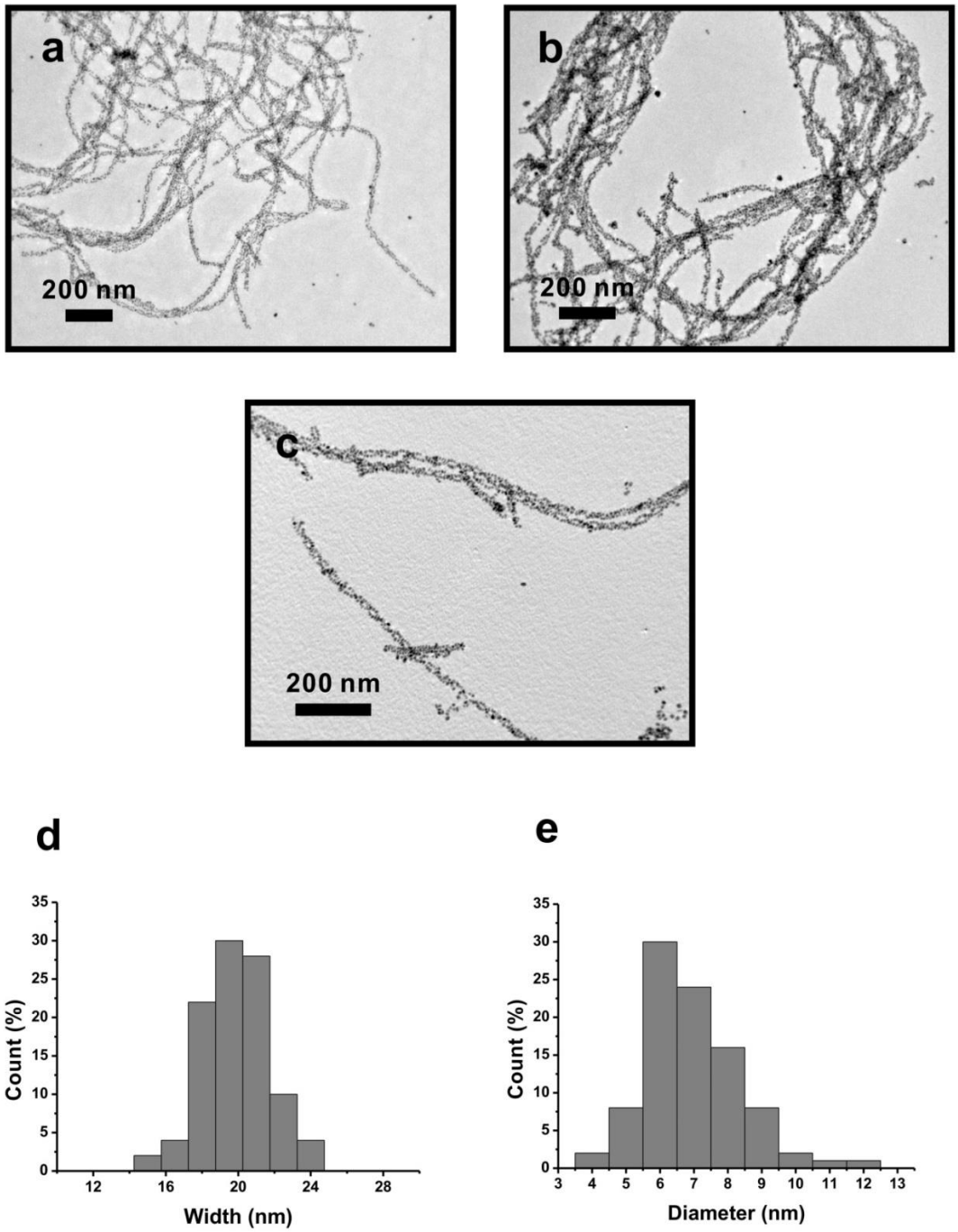

Figure 18. (a-c) TEM images of gold nanoparticle double helices formed using **2**; (d) Width distribution of gold nanoparticle double helices: 20.1 ± 1.8 nm, based on 100 counts; (e) Diameter distribution of gold nanoparticles within the superstructures: 7.3 ± 1.4 nm, based on 100 counts.

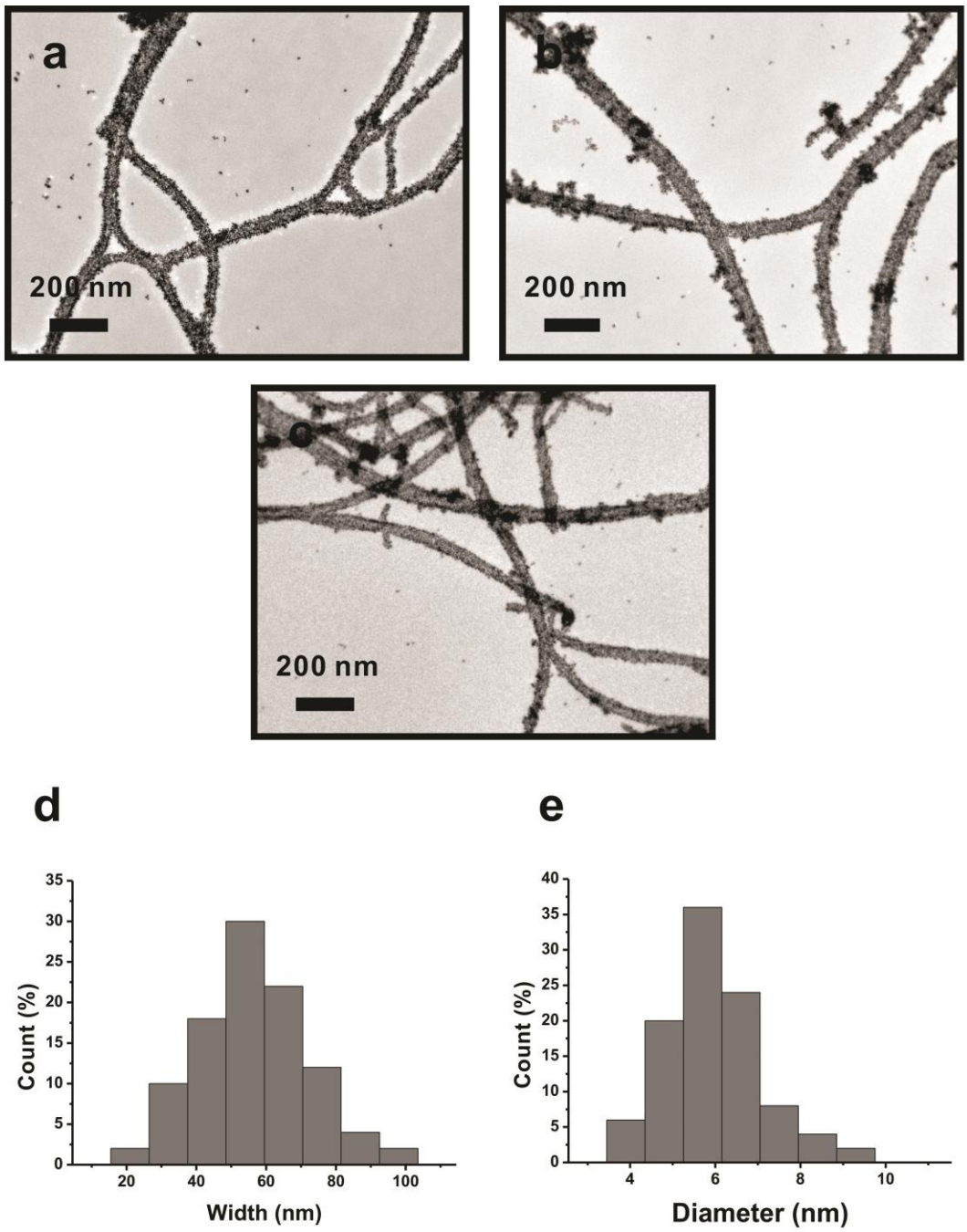

Figure 19. (a-c) TEM images of thick, branched 1-D nanoparticle superstructures formed using **3**; (d) Width distribution of superstructures: 61.4 ± 15.7 nm, based on 100 counts; (e) Diameter distribution of gold nanoparticles within the superstructures: 6.3 ± 1.2 nm, based on 100 counts.

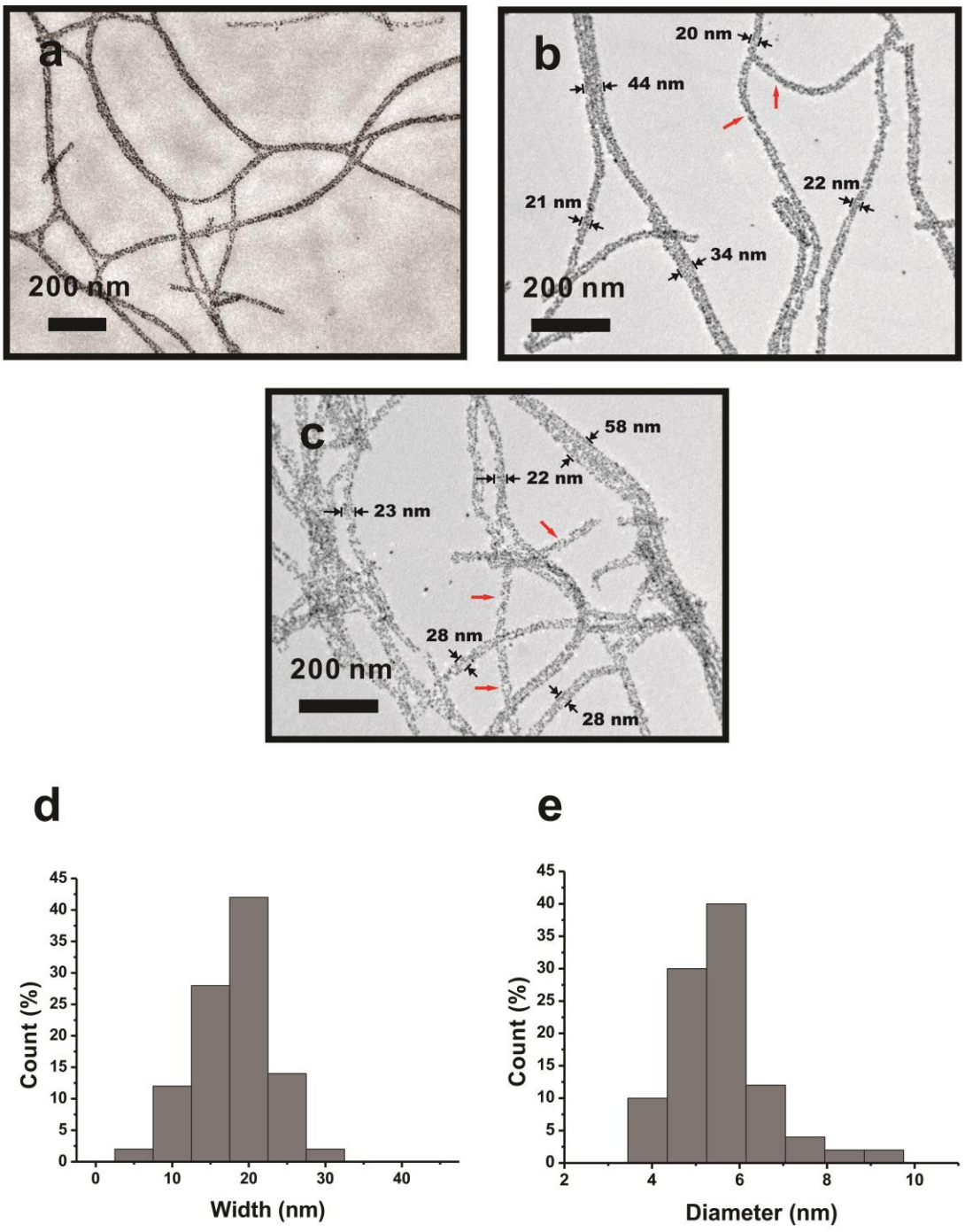

Figure 20. (a-c) TEM images of thin, intertwined 1-D nanoparticle superstructures formed using **4**; (d) Width distribution of superstructures: 20.5 ± 4.9 nm, based on 100 counts; (e) Diameter distribution of gold nanoparticle within the superstructures: 6.0 ± 1.1 nm, based on 100 counts. Red arrows indicate the regions of the structure that appear to exhibit a helical arrangement of the nanoparticles.

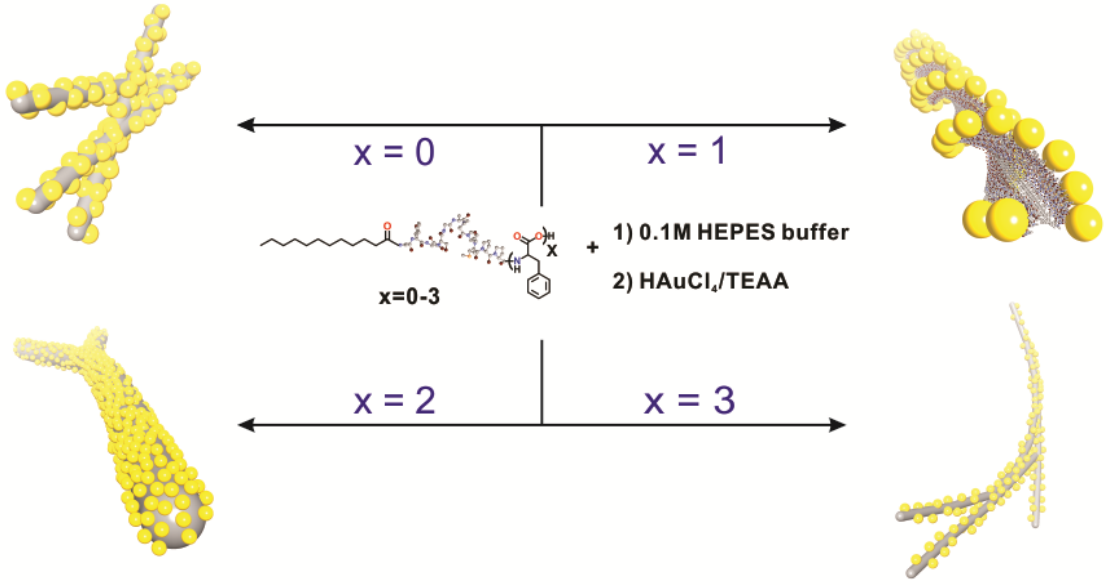

Scheme 2. The number of F_x residues (x= 0-3) at the C-terminus of C_{12}-AYSSGAPPMPPF$_x$ determines the structure of 1-D gold nanoparticle superstructures. x=0: aggregated 1-D structures; x=1: double helices; x=2: thick, branched 1-D structures; x=3: thin, intertwined structures.

The results from these studies are generally consistent with our peptide conjugate assembly studies. Superstructures formed using **1** are linear, yet very irregular (**Figure 17**). Here, the terminal F residue of PEP_{Au} has been deleted; this may negatively affect the formation of discrete nanoparticles and lead to irregular or aggregated nanoparticles. In fact, previous studies have demonstrated that the terminal F residue of PEP_{Au} is important for binding to the Au surface.[65,105] **3** predominantly forms thick bundles of fibers, which leads to the formation of thicker 1-D nanoparticle assemblies (**Figure 19**). In this case, I collected images of superstructure formation after 50 minutes of reaction (**Figure 21**). It is clear that multiple individual fibers bundle together to form thick fibers, and nanoparticle growth is observed on these thick bundles. At this stage, it is unclear why the nanoparticles only decorate the fiber

bundles rather than individual fibers; studies are currently underway that investigate the mechanism of superstructure formation using **3**, which may provide insight into this observation.

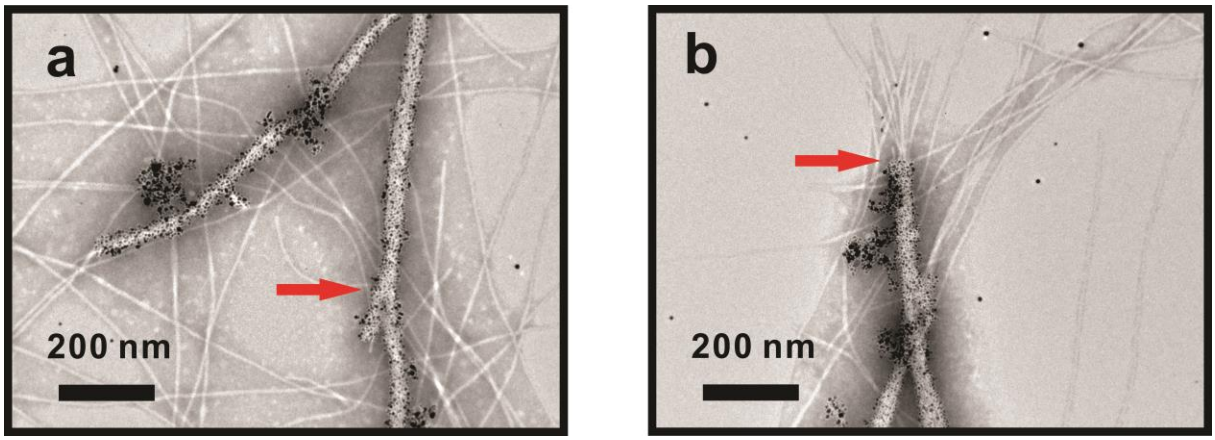

Figure 21. Negatively-stained TEM images of nanoparticle superstructures formed using peptide conjugate **3** after 50 minutes of reaction. These images reveal that multiple fibrils bundle together, to form thick fiber bundles. The nanoparticle superstructures form upon these thick bundles.

I observed some important similarities between the nanoparticle superstructure products of **2** and **4** (**Figure 18** and **20**). Consistent with previous studies,[53,72,73] **2** predominantly assembles into non-aggregated fibers, which lead ultimately to the formation of isolated double-helical nanoparticle assemblies as the major product and some bundled and intertwined double helices. **4** forms a mixture of fibers and fiber bundles, which leads to the formation of some isolated yet a majority of intertwined 1-D nanoparticle superstructures. The widths of these thin nanoparticle superstructures (**2**: 20.1 ± 1.8 nm; and **4**: 20.5 ± 4.9 nm) are consistent with having a single fiber (**2**: 6.7 ± 0.9 nm; and **4**: 6.5 ± 0.8 nm) decorated with nanoparticles (**2**: 7.3 ± 1.4 nm; and **4**: 6.0 ± 1.1 nm). The nanoparticle arrangement in the superstructures formed with **4** is difficult to discern, although some regions of the structure appear to exhibit a helical

arrangement of the nanoparticles (Red arrow in **Figure 20**). Superstructures from **4** assemble together to form larger scale structures with diameters ranging from ~20 nm to ~60 nm (**Figure 20**). These data indicate that the addition of F residues (in the case of **4**) provides a way to assemble helical nanoparticle assemblies into larger scale structures.

To investigate whether C-terminal F residues are important for fiber formation and fiber bundling, I studied the assembly of C_{12}-PEP_{Au}-E (**5**; C_{12}-AYSSGAPPMPPFE). E, glutamic acid, is hydrophilic. 150 μM solutions of **5** in 0.1 M HEPES buffer were allowed to stand for 1 week. Negatively-stained TEM images of the assembly product revealed only spherical assemblies (**Figure 22**). In the presence of Ca^{2+}, only spherical assembly was observed after 30 min incubation. These data suggest that C-terminal hydrophobicity may be important for directing fiber formation and bundling.

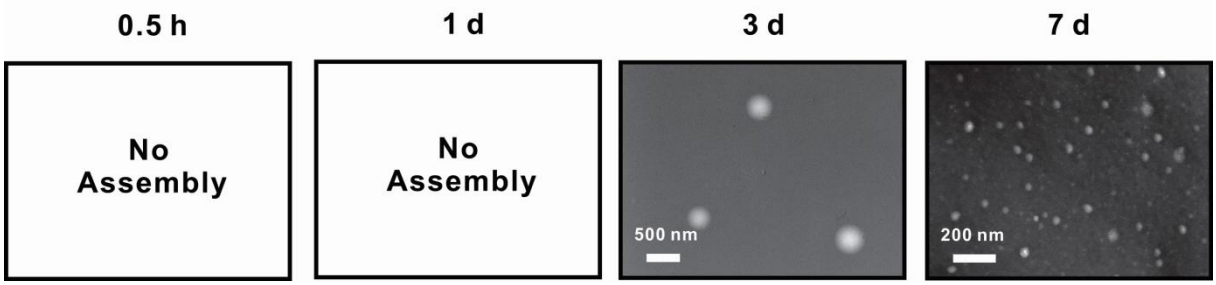

Figure 22. Negatively-stained TEM images of soft-assemblies prepared using peptide conjugate **5**, after various incubation periods.

2.3 CONCLUSION

In this study I investigated the impact that modifications to the C-terminus of C_{12}-PEP_{Au} have on the soft assembly of peptide conjugates and the structure and assembly of 1-D nanoparticle superstructures. I discovered that the addition of hydrophobic F residues can lead to fiber bundling which in turn leads to the formation of thick or intertwined 1-D nanoparticle superstructures. Compared with previous studies, in which modifications were made at the N-terminus to affect the intermolecular interaction and in turn lead to the formation of diverse nanoparticle assemblies, modifying the C-terminus of peptide conjugates not only influence the intermolecular interaction but also promote the interaction between their superstructures. These results indicate that C-terminal modifications to peptide conjugates represent another category of synthetically-addressable features that can be carefully tuned to impact both the structure of nanoparticle superstructures and the co-assembly of these structures. Finally, these studies, when grouped with previous studies on these systems, demonstrate that peptide conjugates are a highly tailorable class of molecules whose structures and compositions can be carefully programmed to direct the synthesis and assembly of a diverse array of complex hierarchical nanoparticle-based structures.

2.4 EXPERIMENTAL SECTION

2.4.1 Materials and methods

All solvents and chemicals were obtained from commercial sources and used without further purification. 0.1 M HEPES Buffer (HEPES = 4-(2-hydroxyethyl)-1-piperazineethanesulfonic acid) was made by directly diluting 1.0 M HEPES buffer (pH = 7.3 ± 0.1; Fisher Scientific) with water (NANOpure, Barnstead DiamondTM System.; 18.2 MΩ). Peptides with sequences of AYSSGAPPMPP, AYSSGAPPMPPF, AYSSGAPPMPPFF, and AYSSGAPPMPPFFF were synthesized and purified by New England Peptide with final purity of 99%. AYSSGAPPMPPFE was prepared by Argonne National Laboratory with final purity of 99 %. Reverse-phase high-pressure liquid chromatography (HPLC) was performed at ambient temperature with an Agilent 1200 liquid chromatographic system equipped with diode array and multiple wavelength detectors using a Grace Vydac protein C4 column (214TP1010, 1.0 cm × 25 cm). Matrix-assisted laser desorption ionization time-of-flight (MALDI-TOF) mass spectra were obtained on an Applied Biosystem Voyager System 6174 MALDI-TOF mass spectrometer using α-cyano-4-hydroxy cinnamic acid (CHCA) as the matrix. Transmission electron microscopy (TEM) samples were prepared by pipetting one drop of solution onto a 3-mm-diameter copper grid coated with carbon film; 2% aqueous phosphotungstic acid was used for negative staining. TEM was conducted on either a JEOL 200CX instrument operated at 200 kV and equipped with a Gatan CCD image system or FEI Morgagni TEM operated at 80kV and equipped with an AMT side mount CCD camera system. Samples for atomic force microscopy (AFM) were prepared on freshly peeled MICA substrates. Tapping-mode AFM was performed on a Veeco Dimension V SPM.

2.4.2 Preparation of N-hydroxyl-succinimide ester and peptide conjugates

N-hydroxyl-succinimide ester. Dodecanoic acid (696 mg, 6 mmol) and N-hydroxysuccinimide (725 mg, 6.3 mmol) were dissolved in 30 mL dry ethyl acetate under an argon atmosphere. After addition of dicyclohexyl carbodiimide (DCC) (1341 mg, 6.5 mmol) at 0 ℃, the solution was stirred overnight at room temperature. The reaction mixture was processed by removing the precipitate via filtration. The solvent was removed under reduced pressure and the crystalline residue recrystallized from isopropanol (iPrOH) to yield the N-hydroxyl-succinimide ester (211 mg, 1 mmol, 17%).

Peptide Conjugates. Peptide conjugates (**1-5**) were synthesized and purified using established methods.[53] Briefly, for **1**, AYSSGAPPMPP (1.20 mg, 8.80 $\times 10^{-7}$ mol) was dissolved in 60 μL DMF. After the addition of dodecanoic N-hydroxyl-succinimide ester (0.6 mg, 2.81×10^{-6} mol) in 60 μL DMF and 1 μL Et_3N under stirring, the solution was stirred at room temperature for 16 hours. Pure peptide conjugate **1** was obtained by conducting reversed-phase HPLC eluting with a linear gradient of 0.05% formic acid in CH_3CN and 0.1% formic acid in water (5/95 to 95/5 over 30 min). The molecular weight for each peptide conjugate was confirmed by MALDI-TOF mass spectrometry. Concentration of the peptide was determined spectrophotometrically in water/acetonitrile (1:1) using the molar extinction coefficient of tyrosine (1280 $M^{-1}cm^{-1}$) at 280 nm.

Note: Peptide conjugates **2**, **3**, **4** and **5** were prepared, purified, and characterized in a similar fashion.

2.4.3 Peptide conjugate soft assembly

Lyophilized peptide conjugate **1** (~ 3.74×10^{-8} mol) was completely dissolved in 250 μL of 0.1 M HEPES buffer in a plastic vial. The above solution was incubated at room temperature and negatively stained TEM samples were prepared at different time points (0.5 h, 1 d, 3 d, and 7 d). The vial was capped to minimize evaporation of solvent.

Note: Soft assembly of peptide conjugates **2**, **3**, **4** and **5** were studied in a similar fashion.

2.4.4 Preparation of gold nanoparticle superstructures

A gold ion precursor solution was prepared: 0.1 M chloroauric acid ($HAuCl_4$) in 1.0 M triethylammonium acetate (TEAA; pH = 7.0) buffer was incubated for 10 minutes at room temperature. Thereafter, this mixture was centrifuged (10 min., 5K rpm). Lyophilized peptide conjugate **1** (~ 3.74×10^{-8} mol) was completely dissolved in 250 μL of 0.1 M HEPES buffer in a plastic vial. After 30 min, 2 μl of the supernatant of the centrifuged gold ion precursor solution was added to the peptide conjugate solution. The mixture was vortexed for a few seconds and then left undisturbed at room temperature for one day and TEM samples were prepared.

Note: When peptide conjugates **2**, **3**, **4** and **5** were used, similar reaction conditions were employed.

3.0 HOLLOW SPHERICAL GOLD NANOPARTICLE SUPERSTRUCTURES WITH TUNABLE DIAMETERS AND VISIBLE TO NEAR-INFRARED EXTINCTION

A portion of this work, written in collaboration with Yong Zhou, Andrea Merg, Chengyi Song, George C. Schatz and Nathaniel L. Rosi*, was published in *Nanoscale* 2014, *6*, 12328.

3.1 INTRODUCTION

Hollow spherical nanoparticle assemblies [33,74,83,84,106-115] are attracting widespread interest from multiple research communities because of their potential use as theranostic materials,[33,106-112,115] heterogeneous catalysts,[116] and metamaterials.[117,118] Hollow spherical gold nanoparticle assemblies, for example, have shown promise for drug delivery and as agents for photothermal therapy;[33,106,108,109,112] for the latter, structures absorbing in the near-infrared (NIR) window (~650-900 nm) are particularly relevant, because biological tissue does not significantly absorb in this region of the spectrum.[3] In addition, large spherical assemblies of gold nanoparticles are known to display a significant magnetic dipole response in the visible, an important property for 'perfect imaging'.[117,118] Spherical assemblies of catalytic nanoparticles can show improved properties compared to individual nanoparticles. For example, the Rosi Group recently

demonstrated that hollow spherical CoPt nanoparticle superstructures exhibit enhanced catalytic properties compared to discrete, non-assembled CoPt nanoparticles.[116] Here, I present straightforward methods for preparing hollow spherical gold nanoparticle superstructures having three different diameters: ~40 nm, ~75 nm, and ~150 nm. I report the size-dependent optical extinction properties for this class of nanoparticle assemblies, which are tunable from the visible and into the NIR. Additionally, I present computational models developed by our collaborators that assist in understanding these important collective optical properties. This work provides a practical route for preparing a family of spherical nanoparticle superstructures having tailorable diameters and optical properties.

My motivation for fabricating spherical nanoparticle assemblies derives not only from their potential practical importance, but also from a fundamental interest in designing nanoparticle superstructures and controlling their compositions, morphologies, structural metrics, and physical properties. It is understood that the properties of nanoparticle superstructures originate from the size, shape, and compositions of the component nanoparticles as well as the precise organization of the nanoparticles within the superstructures.[79,81,119] In order to design and prepare unique nanoparticle superstructures and control their physical properties, the Rosi Group has developed a peptide-based method for directing the synthesis and assembly of inorganic nanoparticles.[53] Briefly, this method utilizes peptide conjugate molecules that are designed to not only bind to the surface of specific inorganic nanoparticles, but also direct the assembly of these nanoparticles into particular target nanoparticle superstructures. The peptide portion of the peptide conjugate molecule binds to the nanoparticle surface,[34,51,52,120-122] while an organic molecule (e.g. an aliphatic chain) tethered to the peptide's N-terminus influences the assembly of the peptide conjugate. The group has successfully used this methodology to prepare a diverse

collection of nanoparticle superstructures with tunable compositions, morphologies, metrics, and properties.[53,72-75,83,116,123]

In 2010, the Rosi Group reported that C_6-AA-PEP_{Au} conjugates (C_6 = $C_6H_{11}O$, A = alanine, PEP_{Au} = AYSSGAPPMPPF)[52] direct the synthesis and assembly of hollow spherical gold nanoparticle superstructures.[74] These structures consisted of ~8 nm gold nanoparticles arranged in a monolayer shell around a spherical vesicular self-assembled peptide conjugate core. Unique aspects of these structures included their small diameter (~50 nm) and hollow interior, which pointed toward their potential application as nanoscale carriers for drugs or other cargo. After this initial report, the group also demonstrated that BP-A_x-PEP_{Au} ($C_{12}H_9CO$–A_x–AYSSGAPPMPPF; x = 2 or 3; BP = biphenyl) could also direct the formation of spherical gold nanoparticle superstructures and that the number of additional alanine residues at the N-terminus (2 or 3) controls the diameter of the spherical superstructures (large, >100 nm or small, ~30 nm).[75] Based on this prior work, one can fabricate hollow spherical nanoparticle superstructures with three different diameters; however, each superstructure requires synthesis of a unique peptide conjugate molecule, which is practically limiting. Ideally, a single peptide conjugate should be capable of directing the formation of spherical superstructures with different diameters, provided that one can control the assembly conditions of the peptide conjugate and the diameter of its resulting spherical soft assembly (micelle or vesicle, for example) and the synthetic conditions for preparing the nanoparticle superstructure. In this chapter, I demonstrate that C_6-AA-PEP_{Au} can be used to direct the synthesis and assembly of three different size classes of hollow spherical gold nanoparticle superstructures. I highlight the role of synthesis and assembly conditions in controlling the diameter of the spheres; I use UV-Vis spectroscopy to study their

diameter-dependent optical properties; and I present computational models to understand their visible and NIR extinction.

3.2 RESULTS AND DISCUSSION

The sphere syntheses are straightforward and require minimal synthetic effort. The three principal components of the syntheses are i) the peptide conjugate (in this case C_6-AA-PEP_{Au}), which serves as the particle binding agent and as the structure-directing agent; ii) 4-(2-hydroxyethyl)-piperazineethanesulfonic acid (HEPES) buffer (pH= 7.3 ± 0.1), which serves as the medium for self-assembly and as the primary reducing agent for Au^{3+};[52,124] and iii) a solution of chloroauric acid in 1.0 M triethylammonium acetate buffer ($HAuCl_4$/TEAA), which is the source of gold ions.[74] These components are combined together in one pot to yield a product nanoparticle superstructure. In order to prepare batches of spherical nanoparticle superstructures having different average diameters using C_6-AA-PEP_{Au}, I systematically varied conditions such as the concentrations of C_6-AA-PEP_{Au}, HEPES buffer, and $HAuCl_4$/TEAA. Careful adjustment of these conditions should allow for control over the diameter of the spherical C_6-AA-PEP_{Au} soft assembly that would ultimately serve as the underlying 'template' onto which the nanoparticles would assemble. I began by studying the effect of HEPES buffer concentration on the soft assembly of a fixed amount of C_6-AA-PEP_{Au}. I dispersed 1.87×10^{-8} mol C_6-AA-PEP_{Au} in 125 μL of four different concentrations of HEPES buffer (0.1, 0.05, 0.01, and 0.005 M) and studied their assemblies using transmission electron microscopy (TEM). At specific time points, samples of each solution were spotted onto formvar-coated copper TEM grids and stained using phosphotungstic acid. At the highest concentration of HEPES (0.1 M), no assemblies were

observed, even after 1 week of incubation at room temperature. Large spherical structures (~500 nm diameter) were observed for the 0.05 M sample after 1 day, and a distribution of spherical structures of different diameters were observed after 6 hours and 30 minutes for the 0.01 M and 0.005 M samples, respectively (**Figure 23**). From these data, I conclude that the assembly of C_6-AA-PEP_{Au} occurs more rapidly at lower HEPES concentrations than at higher concentrations. From previous studies,[53,72-75,79,81,83,116,119,123] I determined that the HEPES buffer assists in dissolving the peptide conjugates; therefore, I reason that the conjugates assemble more rapidly at lower HEPES concentrations because they are less soluble at these concentrations. I concluded that HEPES concentration is an important variable that influences the assembly of C_6-AA-PEP_{Au}.

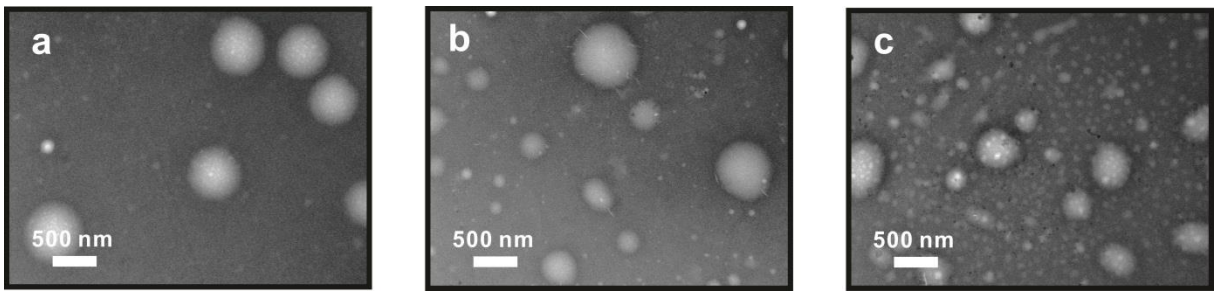

Figure 23. Negatively-stained TEM images of peptide conjugate assemblies at varied HEPES concentrations and incubation periods: a) 0.05 M of HEPES buffer, 1 day; b) 0.01 M of HEPES buffer, 6 h; c) 0.005 M of HEPES buffer, 30 min.

I next studied the assembly of C_6-AA-PEP_{Au} dissolved in a fixed amount and concentration of HEPES buffer (125 μL, 0.05 M) and with the addition of a fixed amount of $HAuCl_4$/TEAA (0.6 μL of a 0.1 M solution of $HAuCl_4$ in 1.0 M TEAA buffer, pH = 7.0). After 30 minutes of incubation at room temperature, I observed large spherical assemblies (diameter = 109 ± 21 nm) at C_6-AA-PEP_{Au} concentrations between 100 and 150 μM and smaller spherical

assemblies (diameter = 27 ± 8 nm) at C_6-AA-PEP_{Au} concentrations between 25 and 75 μM (**Figure 24**). After 4 hours of incubation, I only observed smaller spherical assemblies for each of the studied peptide conjugate concentrations. In the negatively-stained TEM images, I observe gold nanoparticles assembling around the smaller assemblies. I concluded from these data that, at 0.05 M HEPES buffer concentration and in the presence of $HAuCl_4$/TEAA, C_6-AA-PEP_{Au} will, over time, assemble into small spherical assemblies. Moreover, these assemblies will gradually be coated by gold nanoparticles. In fact, after 24 hours of incubation, all of the small spherical assemblies are fully coated with gold nanoparticles. These observations revealed a clear path to the synthesis and assembly of 'small' spherical nanoparticle superstructures. Thus, dissolving C_6-AA-PEP_{Au} (3.74×10^{-8} mol) in 0.05 M HEPES buffer, adding an aliquot of $HAuCl_4$/TEAA solution, and incubating the resulting mixture for 24 h at room temperature yielded small spherical nanoparticle superstructures with an average diameter of 40.4 ± 5.9 nm (**Figure 24a-b and Figure 25**). The gold nanoparticles have an average diameter of 6.2 ± 0.9 nm and the average observable interparticle distance (gap) is 2.4 ± 0.6 nm (**Figure 26**). While I observe some free nanoparticles in the TEM images, the spherical superstructures comprise the major product. A negatively-stained image of a sample from the reaction after 4 hours of incubation indicates that the structures consist of nanoparticles surrounding peptide conjugate cores; I therefore describe the product as hollow spherical nanoparticle superstructures (**Figure 27**).

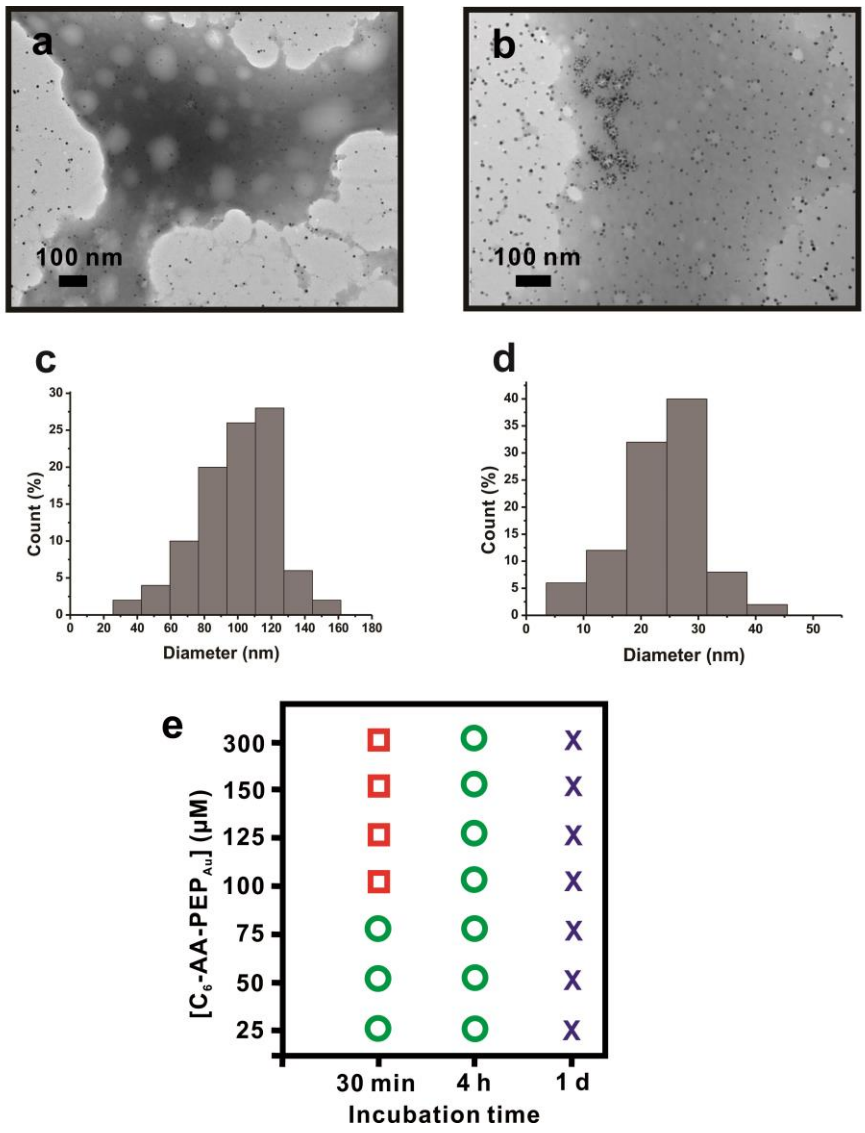

Figure 24. (a) Negatively-stained TEM images of peptide conjugate assemblies after adding $HAuCl_4$/TEAA and incubating at room temperature for 30 min. The concentration of C_6-AA-PEP_{Au} is 100 μM; (b) Negatively-stained TEM images of peptide conjugate assemblies after adding $HAuCl_4$/TEAA and incubating at room temperature for 30 min. The concentration of C_6-AA-PEP_{Au} is 25 μM; (c) Diameter distribution for image (a): 109 ±21 nm, based on 100 counts; (d) Diameter distribution for image (b): 27 ±8 nm, based on 100 counts; (e) Diagram summarizing peptide conjugate assembly in the presence of $HAuCl_4$/TEAA (incubation time versus concentration of C_6-AA-PEP_{Au}): red square, large spheres; green circle, small spheres; navy X, free nanoparticles and small spherical nanoparticle superstructures.

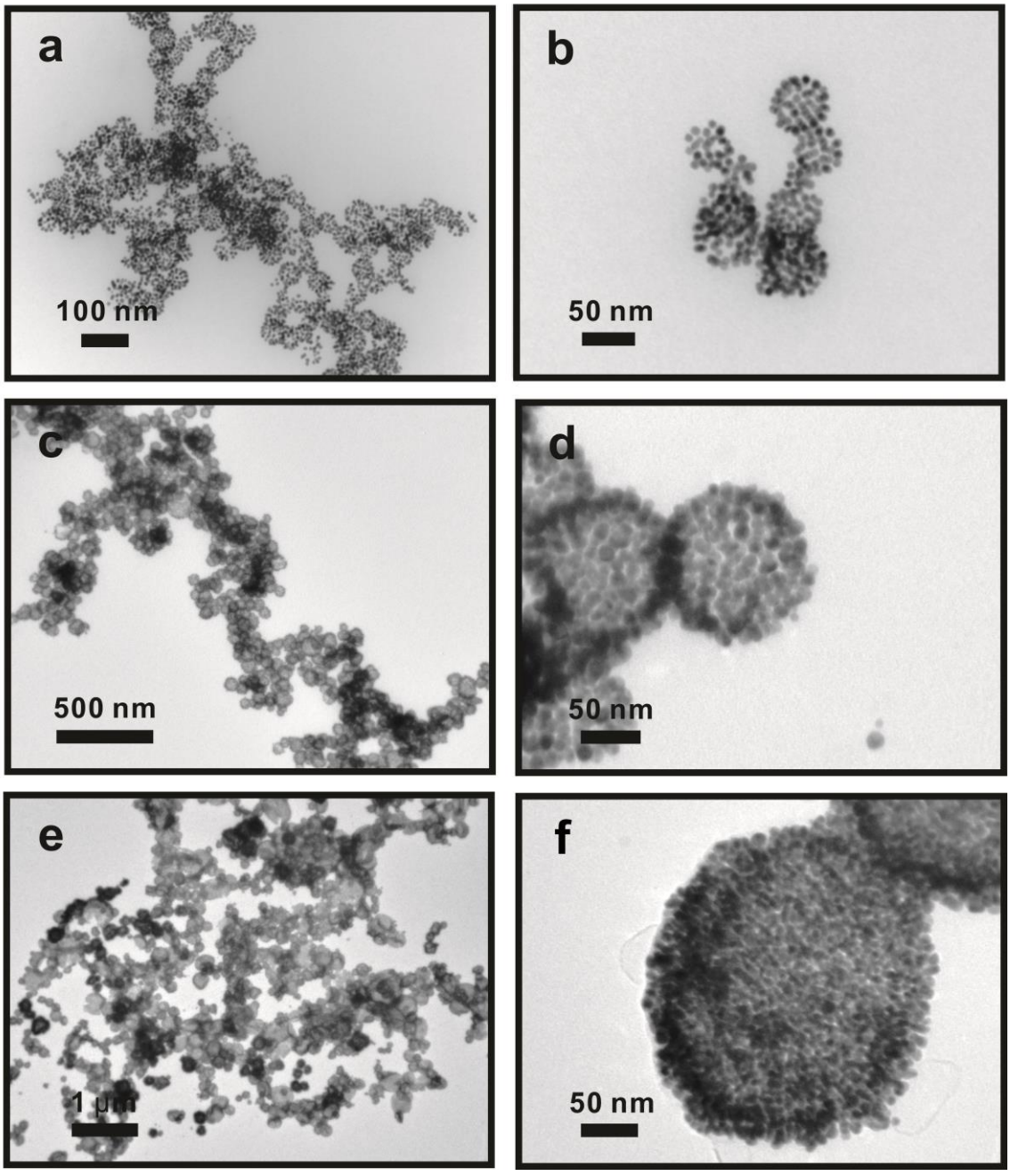

Figure 25. TEM images of hollow spherical gold nanoparticle superstructures. (a,b) Small, (c,d) medium, and (e,f) large.

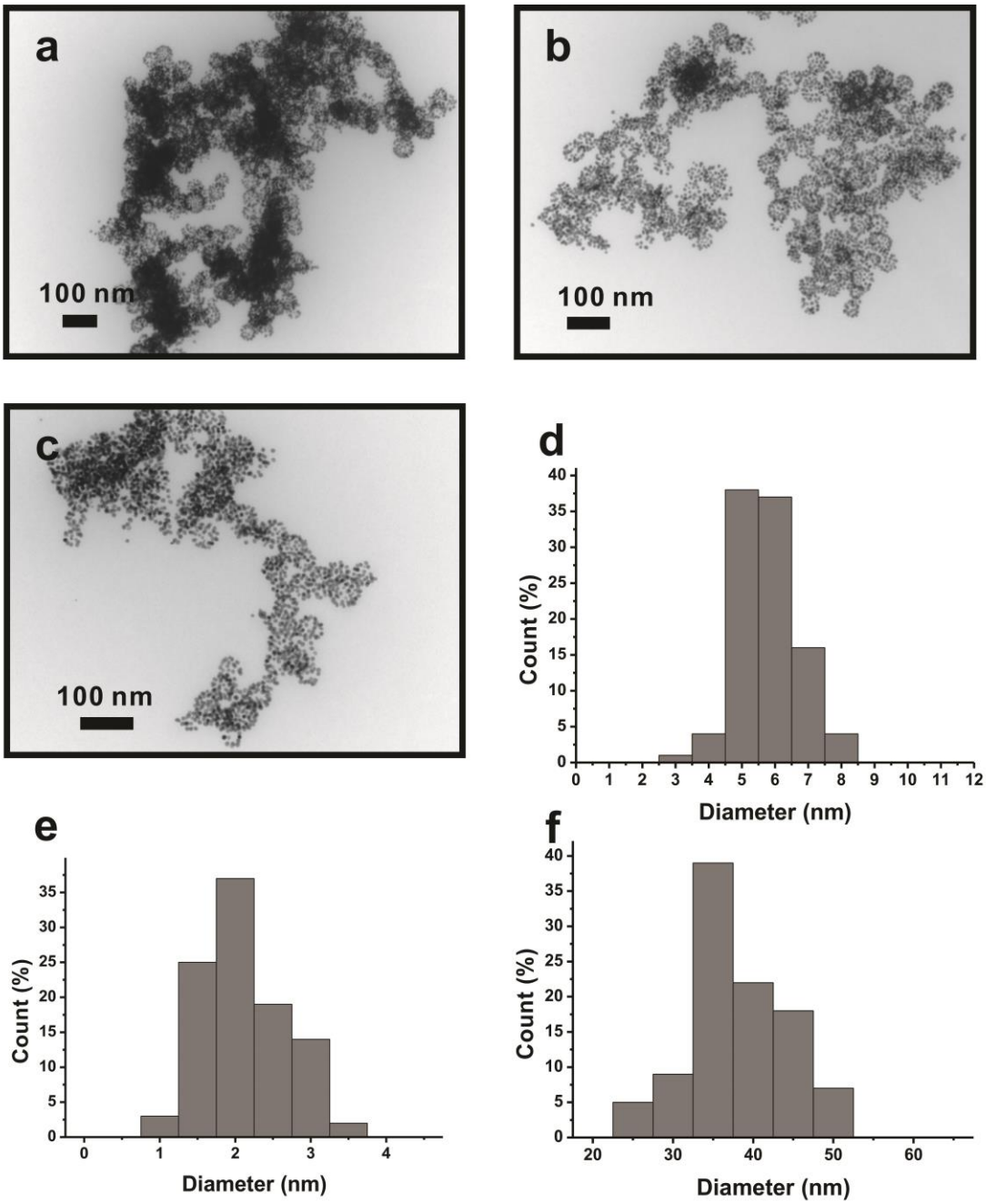

Figure 26. (a-c) Additional TEM images of small spherical nanoparticle superstructures. (d) Distribution of gold nanoparticle diameter within the superstructures: 6.2 ± 0.9 nm, based on 100 counts; (e) Distribution of interparticle distances (gap) within the superstructures: 2.4 ± 0.6 nm, based on 100 counts; (f) Diameter distribution: 40.4 ± 5.9 nm, based on 100 counts. Note: these TEM images, along with those in Figure 1 of the manuscript, were obtained from multiple different sphere syntheses.

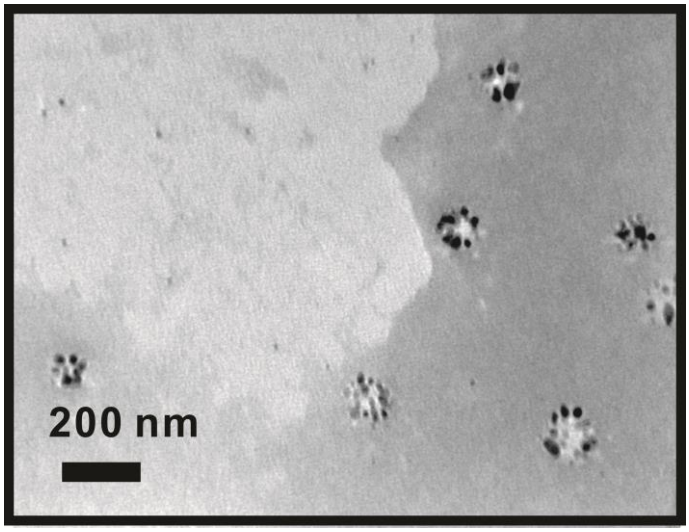

Figure 27. Negatively-stained TEM image of small spherical nanoparticle superstructures in 0.05 M of HEPES after adding $HAuCl_4$/TEAA and incubating at room temperature for 4 hours.

While I do not observe C_6-AA-PEP_{Au} assemblies in 0.1 M HEPES buffer (*vide supra*), I do observe the formation of hollow spherical nanoparticle assemblies after the addition of $HAuCl_4$/TEAA and subsequent incubation at room temperature (**Figure 28**). Because I do not observe peptide conjugate assembly prior to the addition of $HAuCl_4$/TEAA, I suspect that C_6-AA-PEP_{Au} assembly and nanoparticle formation occur simultaneously and that nanoparticle synthesis and assembly is a coupled process; however, at this stage, this is a hypothesis. Hollow spherical nanoparticle superstructures with average diameter of 75.3 ± 12.4 nm were formed after dissolving C_6-AA-PEP_{Au} (1.87×10^{-8} mol) in 0.1 M HEPES (125 μL), adding an aliquot of $HAuCl_4$/TEAA, and incubating for 3 days at room temperature. To minimize aggregation of the product structures, cetyl trimethylammonium bromide (CTAB) was added to the solution after 3 days.[125] During optimization of the synthesis, I observed that very small differences in the amount of added $HAuCl_4$/TEAA significantly affect structural factors such as particle size and

particle density within the product. I found that smaller amounts of $HAuCl_4$/TEAA yield more well-defined and well-dispersed spherical superstructures, while larger amounts of $HAuCl_4$/TEAA yield aggregated superstructures that are more densely loaded with nanoparticles (**Figure 29).** Ultimately, I determined that the addition of 0.7 μL of the $HAuCl_4$/TEAA solution yields the most uniform product (**Figure 25c-d** and **Figure 30**). The average size of the nanoparticles comprising these structures is 8.5 ± 1.5 nm and the observable interparticle distance (gap) is 1.5 ± 0.3 nm (**Figure 30**).

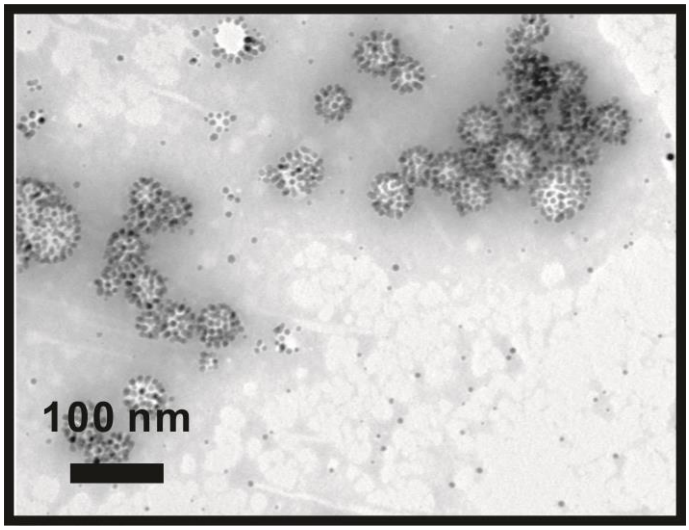

Figure 28. Negatively-stained TEM image of medium spherical nanoparticle superstructures after adding $HAuCl_4$/TEAA and incubating at room temperature for 4 hours.

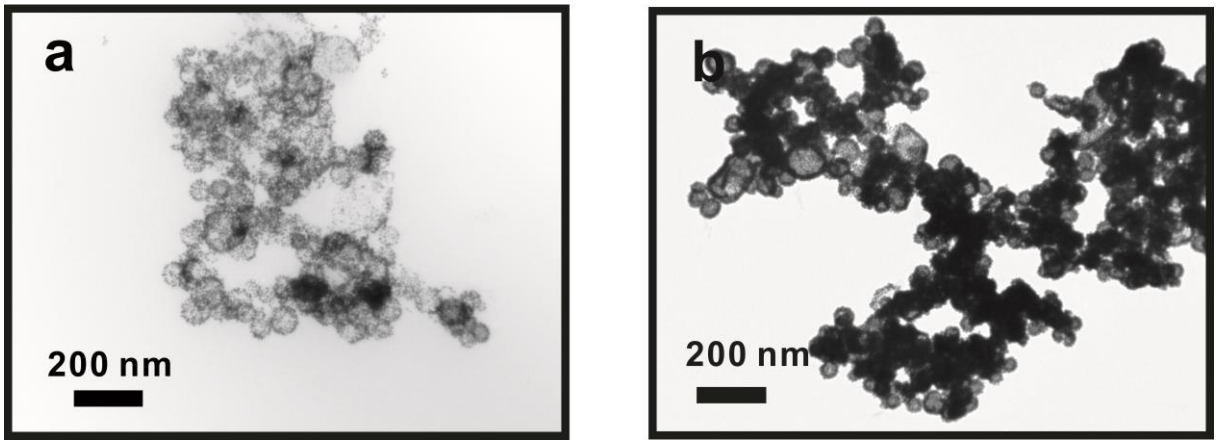

Figure 29. TEM image of medium spherical nanoparticle superstructures prepared using different amounts of $HAuCl_4$/TEAA after one day of incubation at room temperature: a) 0.5 μL $HAuCl_4$/TEAA; b) 1.0 μL $HAuCl_4$/TEAA.

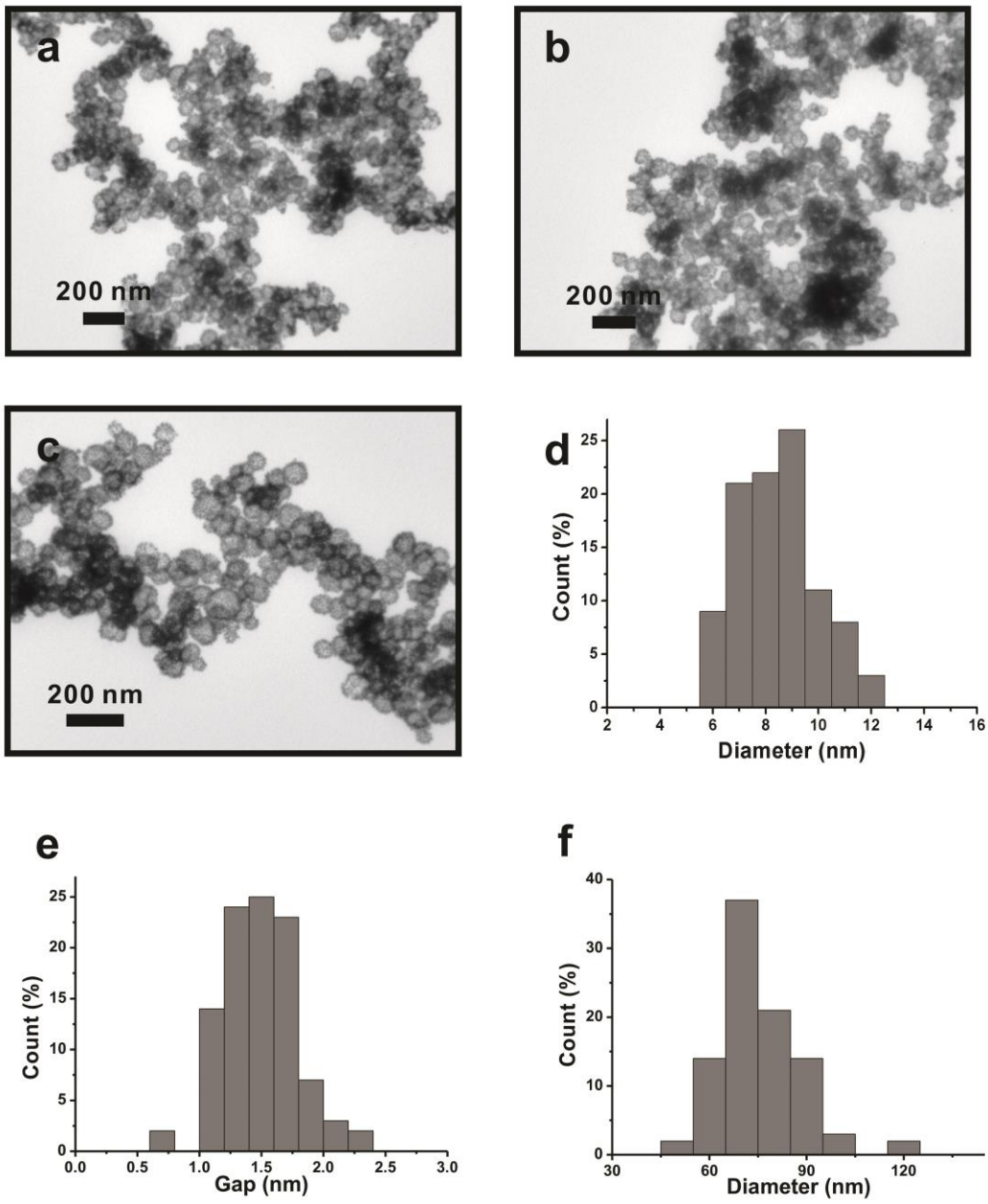

Figure 30. (a-c) Additional TEM images of medium spherical nanoparticle superstructures. (d) Distribution of gold nanoparticle diameter within the superstructures: 8.5 ± 1.5 nm, based on 100 counts; (e) Distribution of interparticle distances (gap) within the superstructures: 1.5 ± 0.3 nm, based on 100 counts; (f) Diameter distribution: 75.3 ± 12.4 nm, based on 100 counts. Note: these TEM images, along with those in Figure 1 of the manuscript, were obtained from multiple different sphere syntheses.

Having prepared both small (~40 nm) and medium (~75 nm) diameter spherical superstructures, I next explored the synthesis of larger spheres (>100 nm) using the same C_6-AA-PEP_{Au} peptide conjugate. I observed that C_6-AA-PEP_{Au} assembles into large spherical assemblies (diameter = 240 ± 81 nm) when dissolved in mixtures of 0.1 M HEPES and 1.0 M TEAA buffer (**Figure 31**), which stands in contrast to what I observed in pure 0.1 M HEPES (*vide supra*). When an aliquot of aqueous $HAuCl_4$ is added to the solution of C_6-AA-PEP_{Au} in HEPES/TEAA, I again observe the formation of large spheriocal peptide conjugate assemblies (diameter = 236 ± 75 nm, **Figure 32**) after 4 hours of incubation at room temperature. After 24 hours of incubation, large hollow spherical gold nanoparticle superstructures having an average diameter of 149.7 ± 30.8 nm were observed (**Figure 25e-f**, and **Figure 33**). These structures consist of gold nanoparticles with an average diameter of 9.9 ± 1.6 nm and an average observable interparticle distance (gap) of 1.6 ± 0.3 nm (**Figure 33**). I conclude that the particles assemble around the peptide conjugate spherical assembly based on examination of negatively-stained images of a sample taken from the reaction after 10 hours of incubation (**Figure 34**). The thickness of the gold nanoparticle shell suggests that ~2 layers of nanoparticles surround the peptide conjugate core. In summary, I have shown that a single peptide conjugate, C_6-AA-PEP_{Au}, can be used to prepare small, medium, and large spheres simply by modifying the synthesis and assembly conditions (**Scheme 3**).

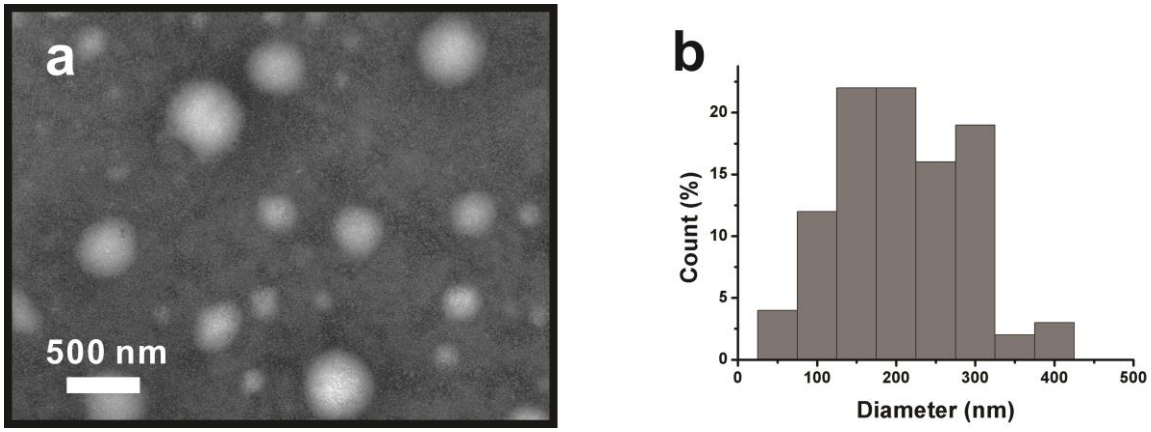

Figure 31. (a) Negatively-stained TEM images of 150 μM C6-AA-PEP_{Au} assembly in HEPES/TEAA mixture after 4 hour incubation at room temperature; (b) Diameter distribution of these assemblies: 240 ± 81 nm, based on 100 counts.

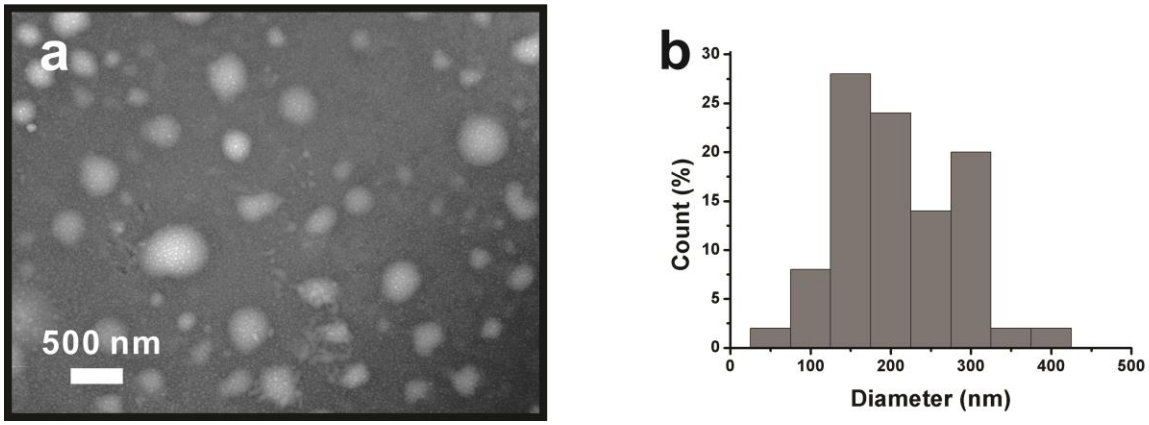

Figure 32. (a) Negatively-stained TEM image of C_6-AA-PEP_{Au} assembly in HEPES/TEAA mixture after adding aqueous $HAuCl_4$ solution and incubating for 4 hours at room temperature; (b) Diameter distribution of these assemblies: 236 ± 75 nm, based on 100 counts.

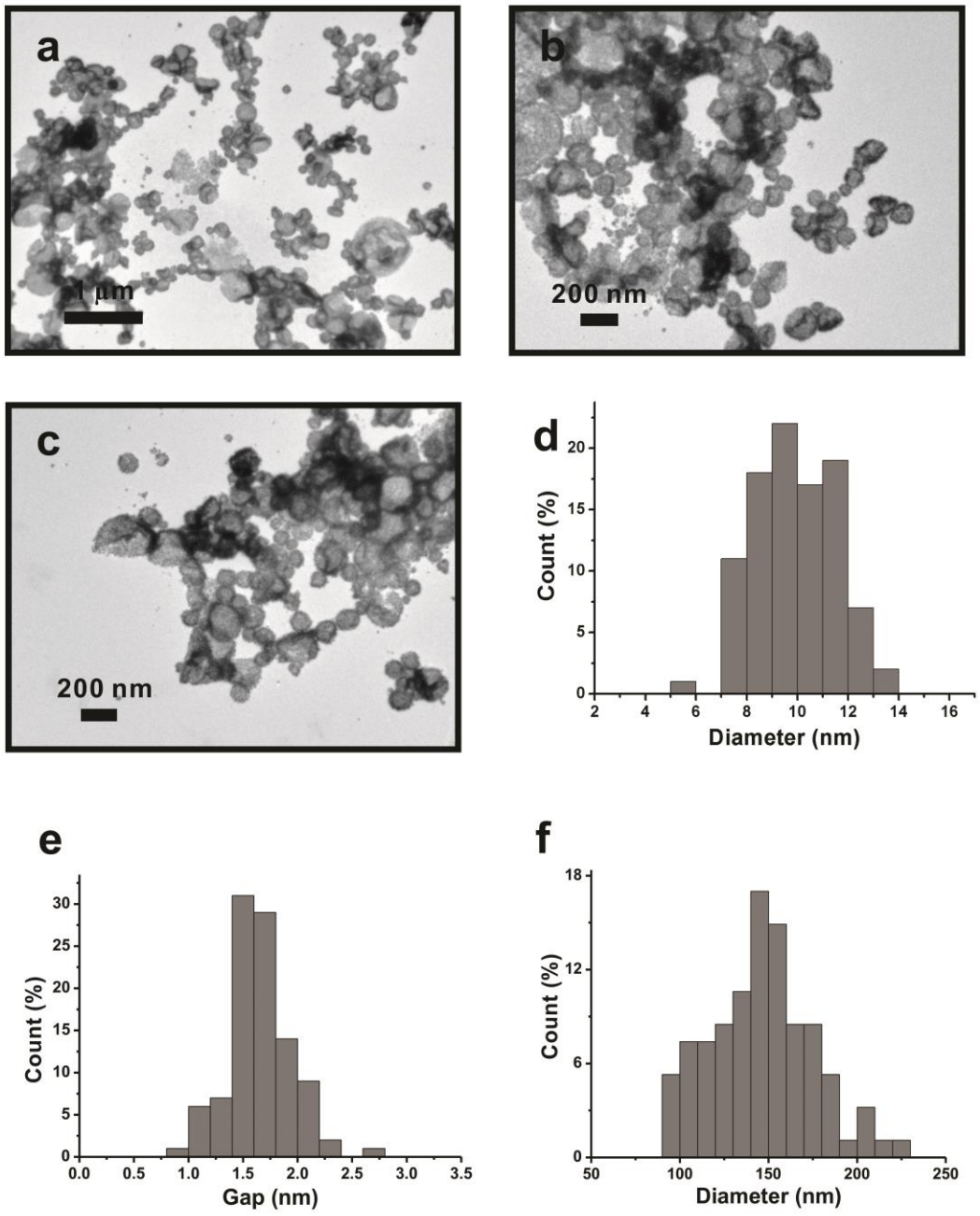

Figure 33. (a-c) Additional TEM images of large spherical nanoparticle superstructures. (d) Distribution of gold nanoparticle diameter within the superstructures: 9.9 ± 1.6 nm, based on 100 counts; (e) Distribution of interparticle distances (gap) within the superstructures: 1.6 ± 0.3 nm, based on 100 counts; (f) Diameter distribution: 149.7 ± 30.8 nm, based on 100 counts. Note: these TEM images, along with those in Figure 1 of the manuscript, were obtained from multiple different sphere syntheses.

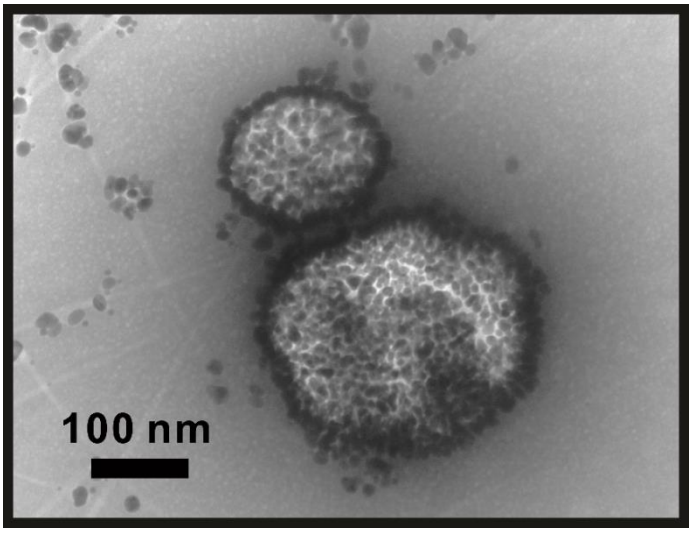

Figure 34. Negatively-stained TEM image of large spherical nanoparticle superstructures in HEPES/TEAA mixture after adding $HAuCl_4$ aqueous solution and incubating for 10 hours at room temperature.

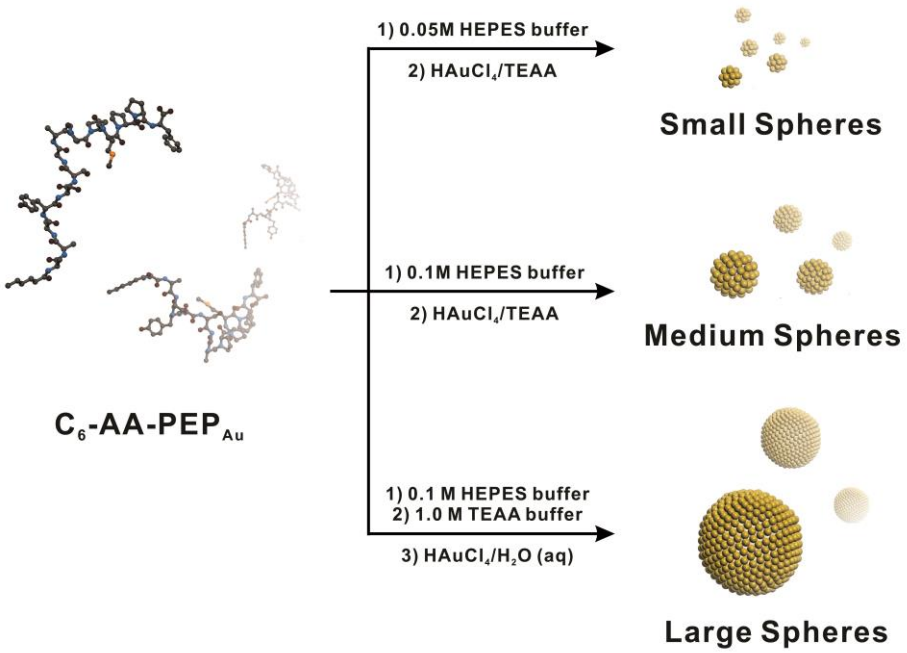

Scheme 3. Direct preparation of hollow spherical gold nanoparticle superstructures with different diameters using C_6-AA-PEP_{Au} (yellow spheres = Au nanoparticles).

Assemblies of plasmonic nanoparticles often exhibit emergent collective optical behavior dependent on the composition and structure of the assembly.[19,20] Moreover, continuous gold nanoshells grown on spherical silica bead templates are known to have NIR extinction.[15] I was keen to measure the absorption properties of the prepared hollow spherical nanoparticle superstructures and to understand the origin of these properties. The UV-Vis spectra for each sample were found to have maxima at 545 nm, 670 nm, and 740 nm, respectively (**Figure 35a**), indicating substantial shifts from the isolated gold nanoparticle plasmon wavelength of 520 nm, and increasing red-shift with increasing superstructure size. The extinction peak for the small spheres was much narrower than that observed for the medium and large spheres, which both exhibited very broad extinction ranging from 500-950 nm. I attribute this broad signal to

polydispersity of the samples and coupling between the surface plasmons of the individual nanoparticles. I note that the extinction maximum for the large spheres (740 nm) lies in the NIR, which may prove useful for biological applications.[33,106-109]

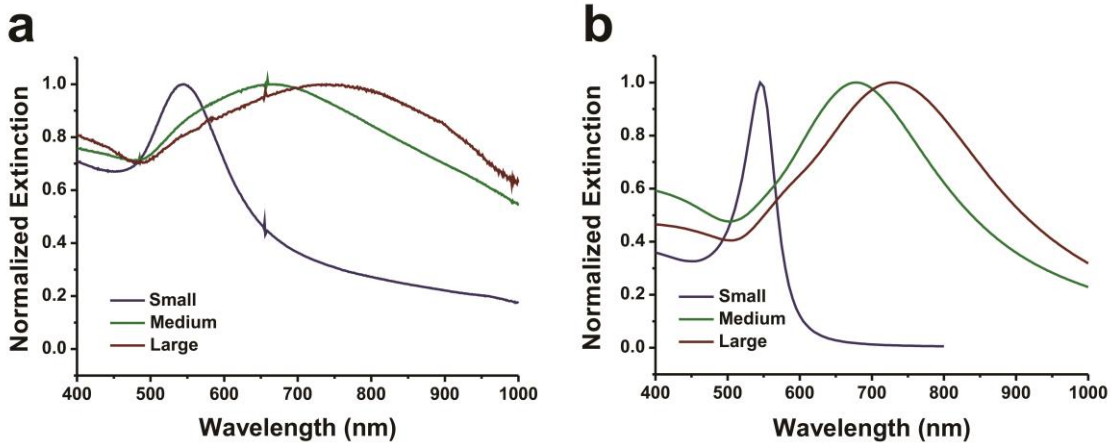

Figure 35. (a) Experimental UV-Vis spectra of hollow spherical gold nanoparticle superstructures with varied sizes. The extinction maxima of small, medium and large gold nanospherical superstructures are observed at 545 nm (blue), 670 nm (green) and 740 nm (red) respectively. (b) Theoretical extinction spectra for the same superstructures, where the small superstructure is modeled using GMM (taking gap parameters from **Table 1**) and the medium and large superstructures are modelled using Mie theory for a spherical metal shell structure.

Electrodynamics calculations have been carried out so as to relate the experimentally observed UV-Vis spectra to structural details of the assemblies. Given that the superstructures appeared to be composed of closely spaced but not necessarily overlapping gold particles, the General Multiparticle Mie (GMM) method[126-129] was first adopted for these calculations as this

provides an exact solution to Maxwell's equations for an assembly of non-overlapping spherical nanoparticles.

The structural parameters used in the simulations are from the experimental measurements, as summarized in **Table 1**. In the absence of structural details beyond what is pictured in the TEM images (e.g. **Figure 25**), it is justified to assume that the nanoparticles are randomly distributed on the surface of the superstructure. This leads to approximately 32, 132, and 764 gold nanoparticles for the small, medium, and large superstructures, respectively. Also, the observations suggest that the small and medium superstructures have monolayer coverage of gold nanoparticles while the large superstructures are consistent with two layers of nanoparticles. Tabulated gold dielectric constants from Johnson and Christy were used, with a correction to the imaginary part of the dielectric constant to include for surface scattering of the conduction electrons.[130-133] The refractive index n of the peptide core was chosen to be 1.6, a typical value used previously.[134] The surrounding medium was assumed to be water with n=1.33.

Table 1. Diameters of the superstructures, diameters of the gold nanoparticles , and observable interparticle distances (gaps).

Superstructures	Spheres (nm)	Nanoparticles (nm)	Gaps (nm)
Small	40.4 ± 5.9	6.2 ± 0.9	2.4 ± 0.6
Medium	75.3 ± 12.4	8.5 ± 1.5	1.5 ± 0.3
Large	149.7 ± 30.8	9.9 ± 1.6	1.6 ± 0.3

Normalized extinction spectra calculated using the GMM method are shown in **Figure 36**. The simulated extinction spectra for the small superstructures peak at 540 nm, which is quite

close to the experimental value, 550 nm. The plasmon maxima for the larger superstructures are red-shifted as expected, however the red shift is significantly smaller than what is observed in the experiments (**Figure 35a**). One possible explanation for this difference in the amount of plasmon band red-shifting is that the real size of the interparticle gaps may be smaller than those measured in the TEM images. Indeed, most interparticle gaps are not clearly defined in the TEM images. To modify the electrodynamics modelling calculations using GMM with smaller gaps were performed. As shown in **Figure 36**, even with gaps decreased down to 1 nm, the calculated SPRs, located at 570 nm and 640 nm for medium and large superstructures, are still far from the experimental observations (670 nm and 740nm).

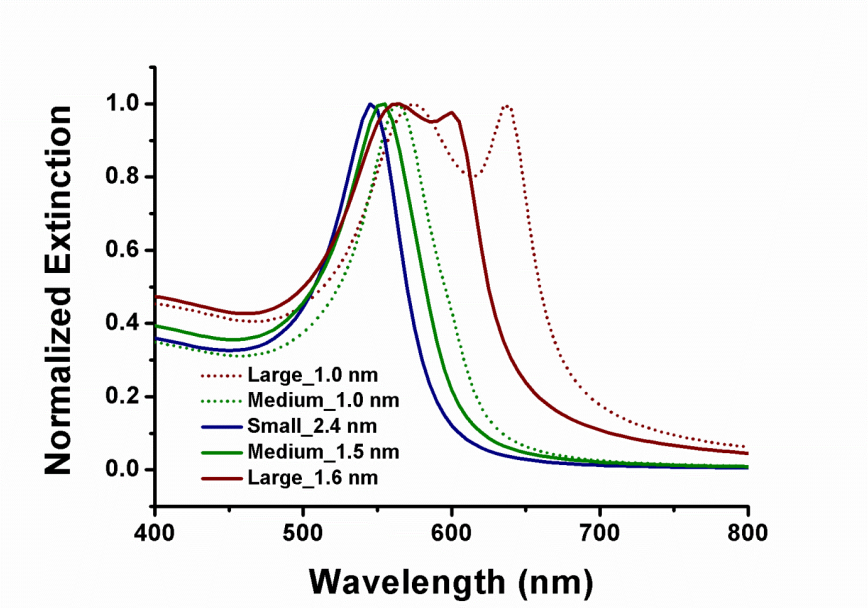

Figure 36. Extinction spectra of hollow spherical gold nanoparticle superstructures calculated using General Multiparticle Mie method. Component nanoparticles are assumed to be fully isolated in the simulation, with interparticle gaps from experimental measurement (see **Table 1**).

For gaps of less than 1 nm, classical theories such as the GMM method are no longer valid due to the onset of quantum effects. Nordlander and co-workers studied the plasmon resonance properties of a nanoparticle dimer using time-dependent density functional theory (TD-DFT), and found that the red-shifting trend with decreasing interparticle gap is reversed for dimer separations below 1 nm.[135] There is also experimental evidence supporting this result.[129,136] Additional resonances, denoted charge transfer plasmons, also appear for small gaps,[137] including one that is red-shifted relative to the red-most classical resonance. Charge transfer plasmons are often described as arising from electron tunnelling between the nanoparticles, and as a consequence there is extreme sensitivity of the energies of these resonances to gap size. Because of this, it is impractical to estimate spectra based on such models.

A much simpler explanation is that the gold nanoparticles are touching or may be partially fused together instead of being fully isolated from each other (**Figure 25b, d, and f**). This leads to the formation of a quasi-continuous gold shell with defects such as pinholes. In a previous study on the optical properties of metal nanoshells, Hao *et al* found that the effect of such small pinholes on the extinction maxima is small.[138] Thus, in the extinction spectrum simulation, the defected quasi-continuous gold shell can be simplified to a perfect continuous spherical shell. The thickness of the equivalent gold shell is determined by the average diameter of the component gold nanopartlces which was taken to be 8.5 nm and 20 nm for the medium and large superstructures, respectively. The optical response of the resulting core-shell structure can readily be studied by Mie theory.[139]

The extinction spectra calculated using this continuous shell model are shown in **Figure 37**. The medium and large superstructures show plasmon resonances at 675 nm and 730 nm, respectively, which are in quite good agreement with the experimentally observed values (670

nm and 740 nm). **Figure 35b** shows calculated spectra analogous to the corresponding experiments in **Figure 35a**, with the small superstructure calculated using GMM while the medium and large superstructures are from Mie theory (and it is noted that the small superstructure is also well-described as a continuous shell with a 7.0 nm thickness). The comparison between theory and experiment is excellent, thus indicating that the continuous shell model is an accurate representation of the plasmonic properties of the superstructures. Differences in the plasmon widths in **Figure 35a** and **35b** are due to polydispersity, as mentioned earlier.

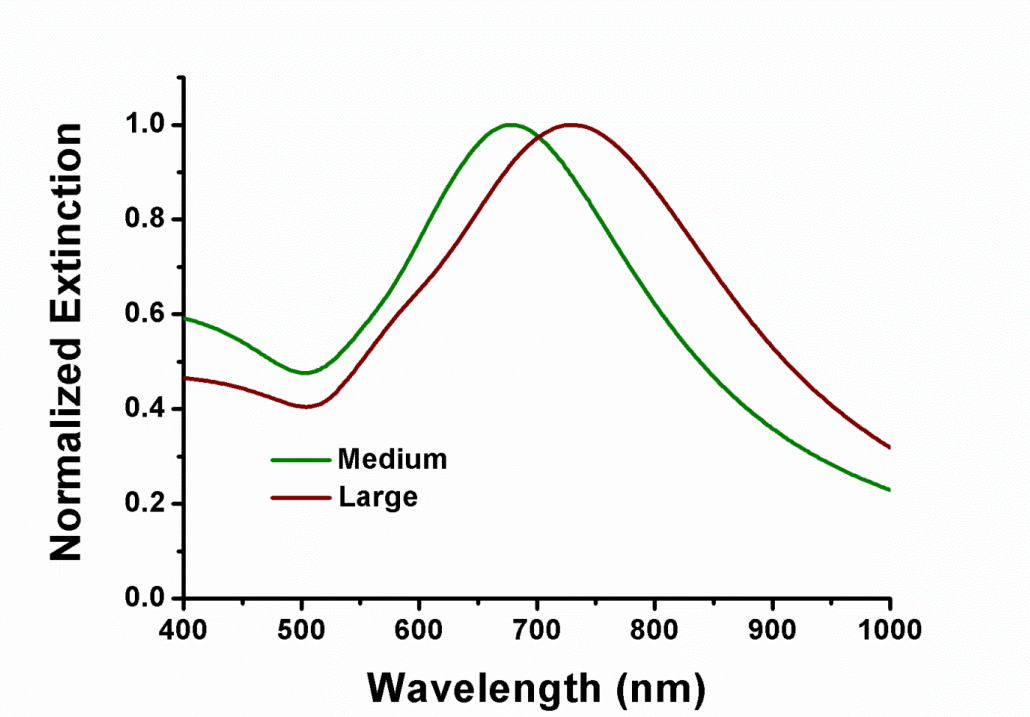

Figure 37. Extinction spectra of hollow spherical gold nanoparticle superstructures calculated using Mie theory. Component nanoparticles are assumed to be fused together. The spherical layer of gold nanoparticles is simplified as a continuous gold shell in the simulation, with the shell thickness determined by the average diameter of gold nanoparticles (see **Table 1**).

3.3 CONCLUSION

In summary, hollow gold nanoparticle superstructures with varied diameters (~40 nm, ~75 nm, and ~150 nm) and surface plasmon resonance (SPR) responses have been prepared by using a single peptide conjugate, C_6-AA-PEP_{Au}. The SPR bands red-shift and broaden as the diameters of the spheres and individual gold nanoparticles increase. Medium (75.3 ± 12.4 nm) and large (149.7 ± 30.8 nm) spheres each display broad SPR peaks in the NIR window (650-900 nm), pointing toward their potential for biological applications. A shell model was used to successfully simulate the optical properties of these materials. The success of this model in explaining the large SPR red-shifting of the medium and large spheres implies that they are likely composed of a quasi-continuous shell structure with defects such as pinholes. Moreover, the shell model can be used to develop design rules for synthesizing new superstructures.

3.4 EXPERIMENTAL SECTION

3.4.1 Materials and methods

All solvents and chemicals were obtained from commercial sources and used without further purification. 0.1M HEPES Buffer (HEPES = 4-(2-hydroxyethyl)-1-piperazineethanesulfonic acid) was made by directly diluting 1.0 M HEPES buffer (pH = 7.3 ± 0.1; Fisher Scientific) with water (NANOpure, Barnstead DiamondTM System.; 18.2 MΩ). Peptide (AAAYSSGAPPMPPF or AA-PEP_{Au}) was synthesized and purified by New England Peptide with final purity of 99%. Reverse-phase high-pressure liquid chromatography (HPLC) was performed at ambient

temperature with an Agilent 1200 liquid chromatographic system equipped with diode array and multiple wavelength detectors using a Grace Vydac protein C4 column (214TP1010, 1.0 cm × 25 cm). Matrix-assisted laser desorption ionization time-of-flight (MALDI-TOF) mass spectra were obtained using an Applied Biosystem Voyager System 6174 MALDI-TOF mass spectrometer using α-cyano-4-hydroxy cinnamic acid (CHCA) as the matrix. Transmission electron microscopy (TEM) samples were prepared by pipetting one drop of solution onto a 3-mm-diameter copper grid coated with carbon film; 2% aqueous phosphotungstic acid was used for negative staining. TEM was conducted on either a JEOL 200CX instrument operated at 200 kV and equipped with a Gatan CCD image system or FEI Morgagni 268 operated at 80kV and equipped with an AMT side mount CCD camera system. UV-Vis spectra were collected using an Agilent 8453 UV-Vis Spectrometer with a quartz cuvette (10 mm pass length) at room temperature.

3.4.2 Preparation of N-hydroxyl-succinimide ester and peptide conjugates

N-hydroxyl-succinimide esters. Caproic acid (1.16 g, 10.0 mmol) and N-hydroxysuccinimide (1.18 g, 10.3 mmol) were dissolved in 100 mL dry ethyl acetate under an argon atmosphere. After addition of dicyclohexyl carbodiimide (DCC) (2.16 g, 10.5 mmol) at 0 ℃, the solution was stirred overnight at room temperature. The reaction mixture was processed by removing the precipitate via filtration. The solvent was removed under reduced pressure and the crystalline residue was recrystallized from isopropanol (iPrOH) to yield the N-hydroxyl-succinimide ester (506 mg, 1.44 mmol, 25%).

Peptide conjugates. AAAYSSGAPPMPPF (1.20 mg, 8.80 $\times 10^{-7}$ mol) was dissolved in 60 μL dimethylformamide (DMF). After addition of caproic N-hydroxyl-succinimide ester (0.6 mg,

2.81×10^{-6} mol) in 60 μL DMF and 1 μL Et_3N under stirring, the solution was stirred at room temperature for 17 h. Pure C_6-AA-PEP_{Au} was obtained by conducting reversed-phase HPLC eluting with a linear gradient of 0.05% formic acid in CH_3CN and 0.1% formic acid in water (5/95 to 95/5 over 30 min.) (**Figure A3**). The molecular weight for C_6-AA-PEP_{Au} was confirmed by MALDI-TOF mass spectrometry (**Figure A4**). The concentration of the peptide was determined spectrophotometrically in water/acetonitrile (1:1) using the molar extinction coefficient of tyrosine (1280 $M^{-1}cm^{-1}$) at 280 nm.

3.4.3 Preparation of small spheres

Lyophilized C_6-AA-PEP_{Au} (~3.74×10^{-8} mol) was completely dissolved in 125 μL 0.05 M HEPES buffer (pH = 7.3 ± 0.1) in a plastic vial. This peptide solution was allowed to incubate at room temperature for 30 min. During the 30 min. incubation time, a fresh gold ion precursor solution was prepared: 0.1 M chloroauric acid ($HAuCl_4$) in 1.0 M triethylammonium acetate (TEAA; pH = 7.0) buffer was incubated for 10 min. at room temperature. Thereafter, this mixture was centrifuged (10 min., 5K rpm). After the 30 min. peptide solution incubation period, 0.6 μL of the supernatant of the centrifuged gold ion precursor solution was added to the peptide conjugate solution. A small amount of black precipitate appears after ~2 s. At that point, the mixture was immediately vortexed for 1 min. and then left undisturbed at room temperature for one day. Products from multiple syntheses were studied using TEM and UV-Vis spectroscopy.

3.4.4 Preparation of medium spheres

Lyophilized C_6-AA-PEP_{Au} (~1.87×10^{-8} mol) was completely dissolved in 125 μL 0.1 M HEPES buffer (pH = 7.3 ± 0.1) in a plastic vial. This peptide solution was allowed to incubate for 30 min. at room temperature. During the 30 min. incubation time, a fresh gold ion precursor solution was prepared: 0.1M chloroauric acid ($HAuCl_4$) in 1.0 M triethylammonium acetate (TEAA; pH = 7.0) buffer was incubated for 10 min. at room temperature. Thereafter, this mixture was centrifuged (10 min., 5K rpm). After the 30 min. peptide solution incubation period, 0.7 μL of the supernatant of the centrifuged gold ion precursor solution was added to the peptide conjugate solution. A small amount of black precipitate appears after ~2 s. At that point, the mixture was immediately vortexed for 1 min. and then left undisturbed at room temperature for 3 days. Afterwards, 1 μL of 0.1 M cetyltrimethylammonium bromide (CTAB) solution was added and then vortexed for 1 min., leading to the final concentration of 0.8 mM of CTAB. Products from multiple syntheses were studied using TEM and UV-Vis spectroscopy.

3.4.5 Preparation of large spheres

Lyophilized C_6-AA-PEP_{Au} (~1.87×10^{-8} mol) was completely dissolved in 110 μL 0.1 M HEPES buffer and 15 μl 1.0 M TEAA buffer (pH= 7.3 ± 0.1) in a plastic vial. This peptide solution was allowed to incubate for 30 min. Thereafter, 4 μl of 0.01 M chloroauric acid ($HAuCl_4$) aqueous solution was added to the above solution. The mixture was immediately vortexed for 1 min. and then left undisturbed at room temperature for one day. Products from multiple syntheses were studied using TEM and UV-Vis spectroscopy.

Note on sphere syntheses: Some batch-to-batch variation in product was observed, in particular for the large spheres where I often observe a broad distribution of sphere diameters. I attribute this variation to the small reaction scale and the small amounts of added reagents.

4.0 HOLLOW SPHERICAL GOLD NANOPARTICLE SUPERSTRUCTURES WITH SIZE-DEPENDENT ENZYMATIC STABILITY AND LASER-TRIGGERED DRUG RELEASE

A portion of this work, in collaboration with Thomas Brinzer, Chong Liu, Sean Garrett-Roe, and Nathaniel L. Rosi*, is *a manuscript in preparation*.

4.1 INTRODUCTION

Targeted drug delivery to specific organs and tissues, especially cancer cells, is a critically important challenge that, if achieved, could revolutionize disease treatment.[140-142] Typical nanostructures for drug delivery include vesicles, inorganic nanoparticles, and nanoparticle assemblies. Molecular vesicles, such as liposomes, have shown great potential in drug delivery due to their biocompatibility, easy preparation, non-specificity to drugs, and their ability to enhance the solubility of drugs.[143] However, liposomes encounter difficulties when orally delivered due to their poor stability under physiological conditions.[144] Also, their pharmaceutical use is limited due to drug molecule leakage via diffusion during the delivery process, as well as the low drug loading efficiency and poorly controlled release.[144] Other disadvantages include poor protection of drug molecules, aggregation of vesicles into larger particles, and difficulties in

scale-up production.[145,146] Inorganic nanoparticles emerged decades ago as drug delivery systems as well as imaging and diagnostic agents. Metal nanoparticles, especially gold nanoparticles, such as spherical gold nanoparticles, gold nanorods, gold nanoshells, and gold nanoboxes have been widely studied for drug delivery.[147] The surface of gold nanoparticles can be easily modified with functional molecules bearing thiol groups, which makes gold nanoparticles promising candidates for drug delivery applications. For instance, the modification of PEG can enhance the stability and biocompatibility of gold nanoparticles. In addition, gold nanoparticles can be modified with an antibody or peptide to target specific tissues or conjugated with drug molecules. More importantly, because of the strong SPR absorbance in near-infrared (NIR) region and efficient conversion into local heat, gold nanorods, nanoshells, and nanoboxes can serve as theranostic agents for drug delivery.[147] However, since the drugs are attached to the surface of the gold nanoparticles and exposed to the external environment, the problem of leakage and stability of drugs needs to be considered for these systems. Spherical gold nanoparticle assemblies,[33,74,75,106,108-110,114,148-151] having hollow cores and near-infrared (NIR) extinction represent a third class of nanostructures for drug delivery. They combine the properties of nanoparticles and liposomes. Their exterior surface can be decorated with specific targeting molecules, their hollow interiors can be loaded with therapeutics, and NIR irradiation can be used both to stimulate local heating and to trigger drug release via structural degradation. Furthermore, the relatively large size of spherical gold nanoparticle assemblies may extend their retention time in tumor tissue.[152] After structural degradation triggered by NIR irradiation, the resulting small nanoparticles can be easily cleared out of human body.[152] All of the above suggest that hollow spherical gold nanoparticle assemblies are promising candidates as theranostic materials, which couple imaging, therapeutic deliver, and photothermal therapy.

The Rosi Group have developed peptide-based methods for assembling gold nanoparticles into hollow spherical gold nanoparticle superstructures. Generally, this method utilizes peptide conjugate molecules that consist of inorganic-binding peptide portion and assembly-assisting organic moiety. The peptide portion, which can bind to specific nanoparticle surfaces, is selected initially from phage display,[34,51,52,120-122] while an organic molecule is tethered to influence the assembly of the peptide conjugate.[67,98,153] By using this methodology, the group has successfully prepared a diverse family of nanoparticle superstructures with tunable compositions, morphologies, structural metrics and properties. In Chapter 3, I demonstrated the use of C_6-AA-PEP_{Au} for the syntheses of hollow spherical nanoparticle superstructures with different diameters.[151] Small (~40 nm), medium (~75 nm), and large (~150 nm) spheres were synthesized. In particular, the medium and large spheres attract considerable interest due to their broad surface plasmon resonance (SPR) extinction centered at ~670 nm and ~740 nm respectively, which lies in the NIR window of the spectrum.

In this study, I demonstrated that these gold hollow spheres can be loaded with drug molecules. They exhibit size-dependent stability in the presence of a non-specific enzyme, proteinase K. The medium spheres are much more stable than the large spheres upon incubation with proteinase K. Furthermore, both types of spheres show no obvious structural degradation and resulting drug release in acidic medium. In addition, NIR laser irradiation (805 nm) was used to degrade both large and medium spheres and triggered the release of drug into solution. As one class of the hollow spherical gold nanoparticle assemblies, these innovative structures can be potentially used as theranostic agents for a combination therapy coupling both imaging and therapeutics. Moreover, the composition of these spheres (peptide conjugate and gold nanoparticles) make the structures potentially suitable for applications in biological tissue. It is

noted that the sub-100 nm size and the enzymatic stability of medium spheres make them particularly attractive and potentially advantageous compared to other known hollow spherical gold nanoparticle assemblies.

4.2 RESULTS AND DISCUSSION

In prior chapter, I already showed the NIR extinction of both medium spheres and large spheres.[151] In order to study their potential application as delivery vehicles, I first tested the stability of the spheres in the presence of enzyme and laser irradiation. Thereafter, I synthesized the drug-loaded spheres and studied their drug-release properties upon incubation with enzyme and laser irradiation.

Large spheres and medium spheres were prepared using the reported method in Chapter 3 (see experimental section for details). The diameters of the as-synthesized large and medium spheres are 155.4 ± 33.7 nm and 72.3 ± 15.2 nm (each based on 100 counts). The diameters of nanoparticles of large spheres and medium spheres are 11.0 ± 2.3 nm and 8.3 ± 1.6 nm, respectively (each based on 100 counts).

Compared with soft vesicular drug carriers, such as liposome and vesicles from amphiphilic polymers, which exhibit poor stability under the physiological conditions,[143,144] hollow spherical gold nanoparticle superstructures are much more stable. However, since peptide conjugate molecules were as the structure-directing agents, I was concerned that enzyme in our body may digest the peptide and induce the disassembly of the superstructures and subsequent drug release before they reach the target. I studied the stability of the medium and large spheres upon incubation with Proteinase K. Proteinase K was chosen because it is a non-

specific peptidase with a very high specific activity over a wide range of pH, which is suitable for HEPES buffer (pH=7.4). First, I tested the stability of C_6-AA-PEP_{Au} in the presence of proteinase K in HEPES buffer. An HPLC trace of the sample (**Figure 38**) revealed the disappearance of C_6-AA-PEP_{Au} peak after the addition of proteinase K, indicating that the enzyme can digest the peptide under the reaction conditions studied. Next, 5 μl of 20 mg/ml proteinase K was directly added to the as-synthesized spheres solution. Thereafter, the mixture was incubated at 37 ℃ for 24 h. Transmission electron microscopy (TEM) and UV-Vis spectroscopy were utilized to monitor the degradation process. Surprisingly, I found that proteinase K can only cause the disassembly of large spheres; the medium spheres remain intact. Based on the TEM images before (**Figure 39a** and **39c**) and after (**Figure 39b** and **39d**) enzyme treatment for one day, I observed no obvious change for medium spheres, while for large spheres, spherical gold nanoparticle superstructures fell apart into free nanoparticles. UV-Vis spectroscopy was used to monitor the reaction after the addition of enzyme (**Figure 39e-f**). I found similar results with TEM images: the SPR peak of medium spheres only shows a slight blue-shift in the spectrum, changing from 670 nm to 665 nm after ~3h, and almost no further change after 27 hours, while the large spheres shows decreasing absorption at longer wavelength (650-900 nm) and increasing absorption at shorter wavelength (500-650 nm). After 27 hours, the large sphere solution only displayed a narrow peak at ~540 nm, which is consistent with the presence of free nanoparticles in the TEM image. I speculate that the size of the enzyme (~4 nm)[154] is the limiting factor for the enzyme-induced degradation. Although the average observable interparticle distances of medium spheres (1.4 ± 0.3 nm) and large spheres (1.7 ± 0.5 nm) are both smaller than the size of proteinase K, the medium spheres have more complete and well-defined structures so they are much more stable while the large spheres have more defects

within their structures that allow the entrance and function of enzyme and are therefore not resistant to enzyme degradation.

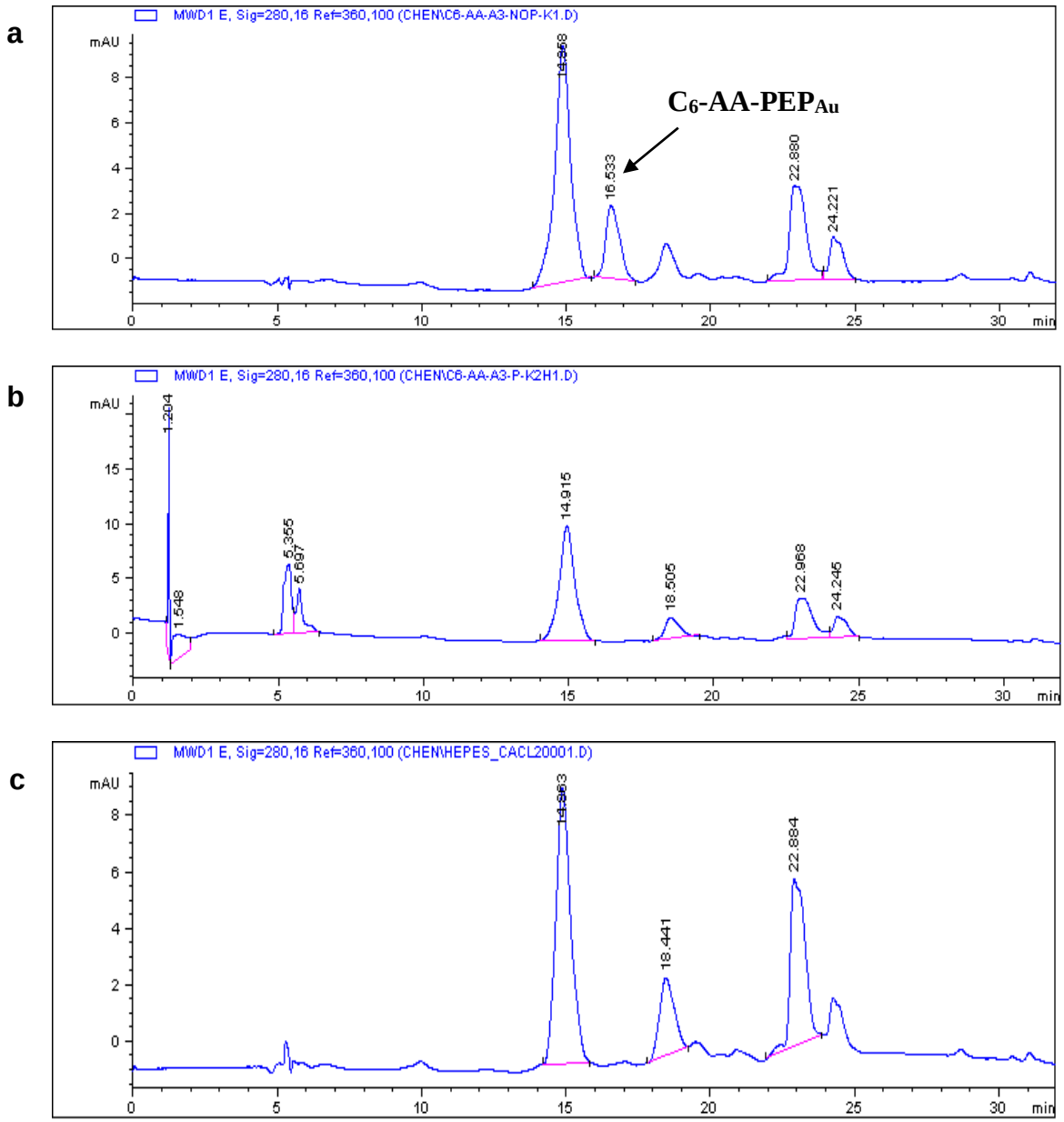

Figure 38. Stability test of C_6-AA-PEP_{Au} in 0.1 M HEPES buffer (pH =7) with the addition of proteinase K using HPLC: a) C_6-AA-PEP_{Au} in 0.1 M HEPES buffer (pH =7); b) C_6-AA-PEP_{Au} in 0.1 M HEPES buffer (pH =7) after the addition of proteinase K for one day at 37 ℃; c) 0.1 M HEPES buffer. The retention time for C_6-AA-PEP_{Au} is around 16.5 min.

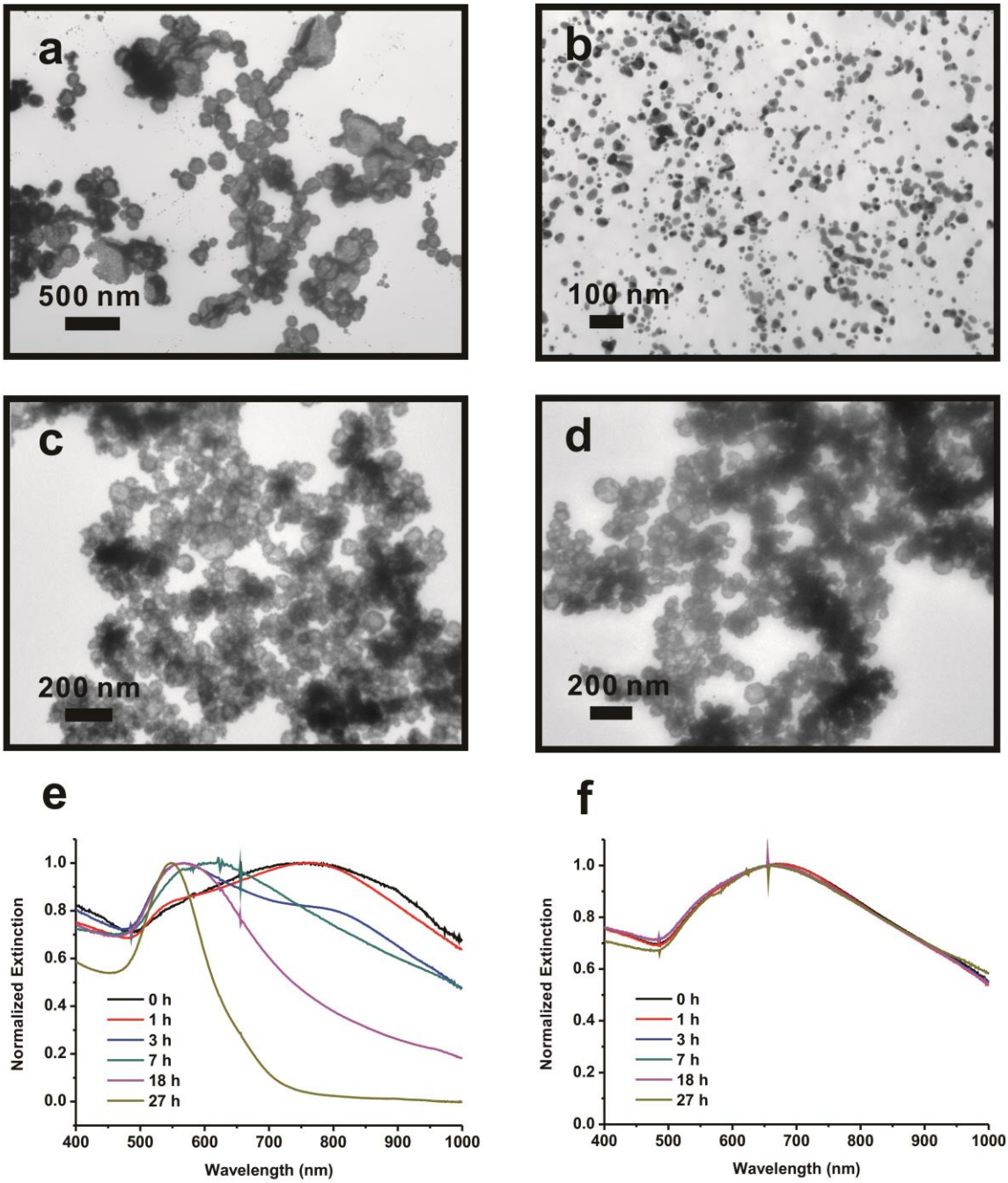

Figure 39. TEM images of large spheres (a) before and (b) after the addition of proteinase K for one day; TEM images of medium spheres (a) before and (b) after the addition of proteinase K for one day; UV-Vis spectra of (e) large spheres and (f) medium spheres after the addition of proteinase K as a function of time.

Gold nanoparticles or assemblies, especially those having strong extinction within NIR window, can be highly promising for photothermal therapy since they can efficiently convert photo energies into heat and increase the local temperature.[152] This produced heat can be utilized to induce the disassembly of nanoparticle superstructures.[33] Therefore, I next investigated the laser-induced degradation of medium and large spheres. First, the solutions of as-synthesized spheres were irradiated with 805 nm pulsed laser for 10 minutes at different average powers: 2.59 W and 1.25 W. Both the large spheres and the medium spheres degrade after extended laser irradiation. TEM images of the solution were taken after laser irradiation (**Figure 40a-d**). Although many free nanoparticles are observed, there are still a few spherical assemblies remaining after irradiation. Irradiation with 2.59 W laser leads to fewer intact spherical assemblies compared to solutions irradiated with 1.25 W lasers. Many medium spheres remained intact after irradiation with the average power of 1.25 W (**Figure 40d**). As shown in UV-Vis spectra (**Figure 39e-f**) of both medium and large spheres, after 10 min irradiation at 805 nm, the sample exposed to the 2.59 W laser power has a narrower extinction and a greater blue-shift compared to the sample exposed to the 1.25 W laser, which indicates the degradation of hollow spherical nanoparticle superstructures. By comparing the UV-Vis spectra of medium spheres and large spheres at the same power, the large sphere samples show a greater blue-shift, indicating that laser irradiation at 805 nm can degrade large spheres more efficiently. I attribute this to the wavelength of extinction peak of these spheres: The maximum extinction of the large spheres is ~740 nm which is closer to 805 nm while the peak of medium spheres is centered at ~670 nm which indicates relatively less absorption at 805 nm.[155,156] All of the above indicate that laser irradiation can lead to efficient degradation of these spherical superstructures.

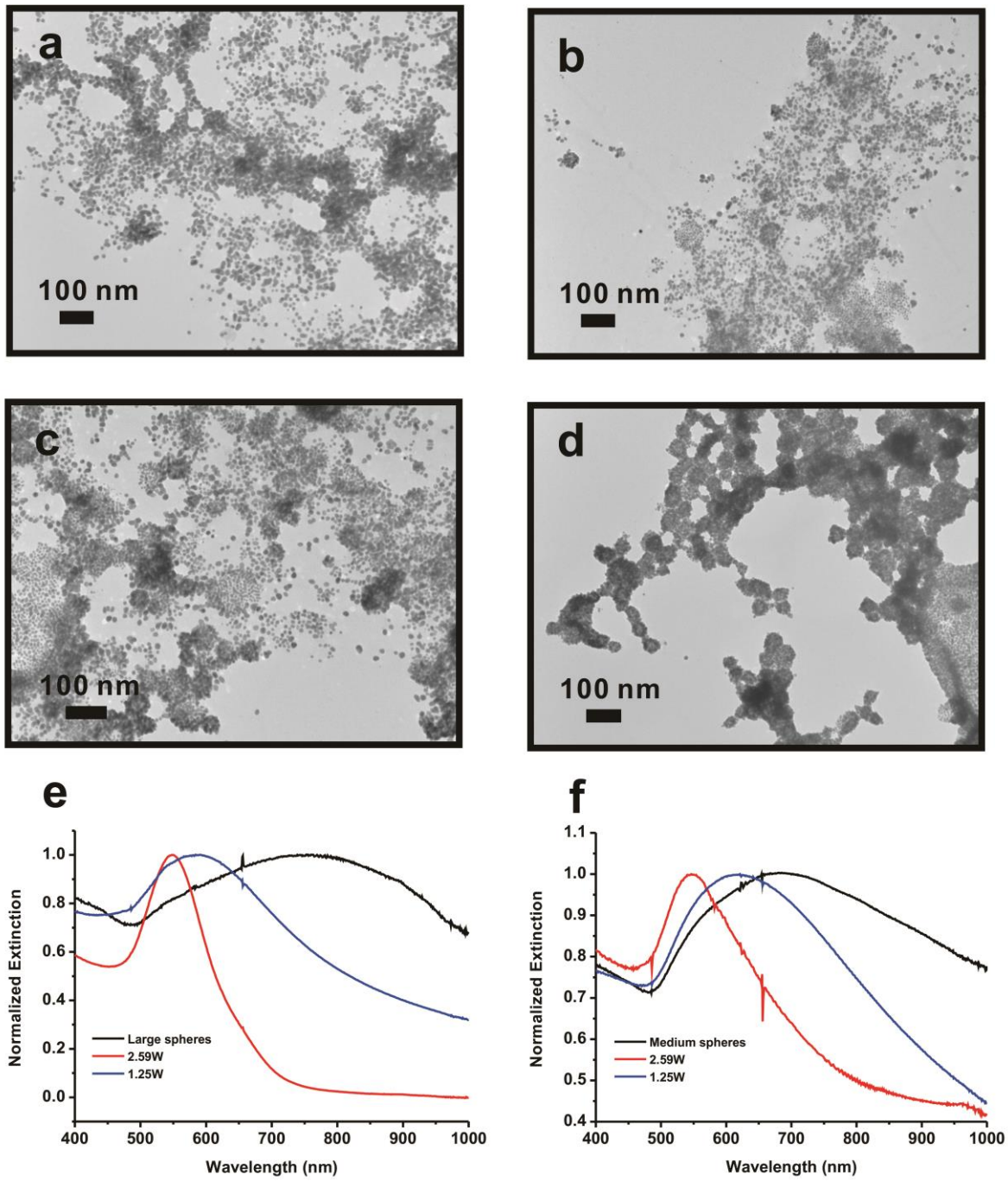

Figure 40. TEM images of (a) large spheres and (b) with 2.59 W laser irradiation for 10 minutes at 805 nm; TEM images of (c) large spheres (d) medium spheres with 1.25 W laser irradiation for 10 minutes at 805 nm; UV-Vis spectra of (e) large spheres and (f) medium spheres at 805 nm with different laser irradiation powers: 2.59 W and 1.25 W.

I also checked the TEM and UV-Vis data at different time points (2, 4, 6, and 8 minutes) during the laser irradiation using 2.59 W at 805 nm (**Figure 41**). Based on this, I found that, with extended laser irradiation times, all the spheres with larger size are degraded, leaving mainly free nanoparticles and a few small spherical assemblies. After 8 min, those smaller spherical assemblies have average diameters of 42.1 ± 9.5 nm and 43.8 ± 10.0 nm (each based on 20 counts) for large spheres and medium spheres, respectively.

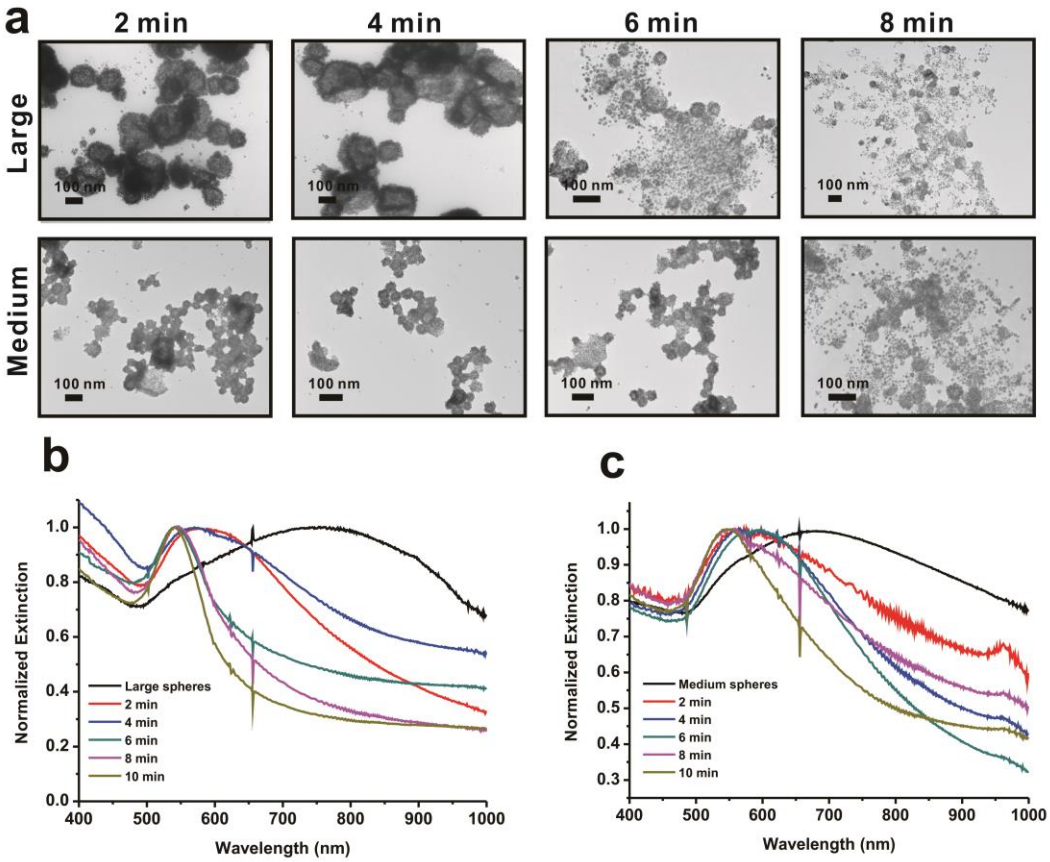

Figure 41. (a) TEM image of large spheres and medium spheres with 2.59 W laser irradiation at 805 nm at different time points: 2 min., 4 min., 6 min., and 8 min.; (b) UV-Vis spectra of large spheres with 2.59 W laser irradiation at 805 nm as a function of time; (c) UV-Vis spectra of medium spheres with 2.59 W laser irradiation at 805 nm as a function of time.

Next, I began to study triggered drug release from these spheres upon the decomposition of the superstructure. Doxorubicin (DOX) was selected as the cargo molecule because it is a fluorescent anti-cancer drug and it has a peak centered at 485 nm in the UV-Vis spectrum[33,109,157] First, I synthesized the drug loaded large spheres and medium spheres by either loading the drugs after the synthesis of spheres (post-synthetic loading) or *in situ* with the synthesis (see experimental section for details). The *in situ* loading method is commonly used for drug encapsulation system, such as liposome, where drug encapsulation and superstructure formation occur at the same time.[143] I used TEM to confirm the formation of spherical gold nanoparticle superstructures when using *in situ* loading method (**Figure 42a-b**). The average diameters of large spheres and medium spheres are 152.3 $\pm$ 32.8 nm and 74.5 $\pm$ 14.6 nm (each based on 100 counts). The diameters of nanoparticles for large spheres and medium spheres are 10.5 $\pm$ 2.0 nm and 8.5 $\pm$ 1.8 nm (each based on 100 counts). This is comparable to the diameters of spheres without loading drugs. Next, the loading efficiency was determined by calculating the difference between the amount of doxorubicin added and the amount of doxorubicin washed out after loading (see experimental section for details). The amount of doxorubicin is determined by the absorption at 485 nm in the UV-Vis spectrum and the calibration curve. I found that the loading efficiency of post-synthetic loading is 4% for large spheres and 2% for medium spheres, while the loading efficiency of *in situ* loading is 51% for large spheres and 43% for medium spheres respectively, which is much higher than encapsulation efficiency using liposome (e.g., 5-15% by using the method of thin-film hydration).[143] The post-synthetic loading is mainly due to physical absorption and slow diffusion of DOX into spherical assemblies while the *in situ* loading is based on *in situ* absorption and capturing of DOX within the hollow interior, which gives more efficient loading of drug molecules. Since the fluorescence of DOX would be quenched within

proximity of gold nanoparticles, I measured the fluorescence of the as-synthesized solution to evaluate the extent of drug loading. Using doxorubicin in HEPES buffer at the same concentration as a control, post-synthesis loading shows a small loss of fluorescence while *in situ* loading method shows much more quenching by gold nanoparticles (**Figure 42c-d**). In addition, large spheres show more quenching than medium spheres. All of these are consistent with the loading efficiency determined by UV-Vis spectroscopy.

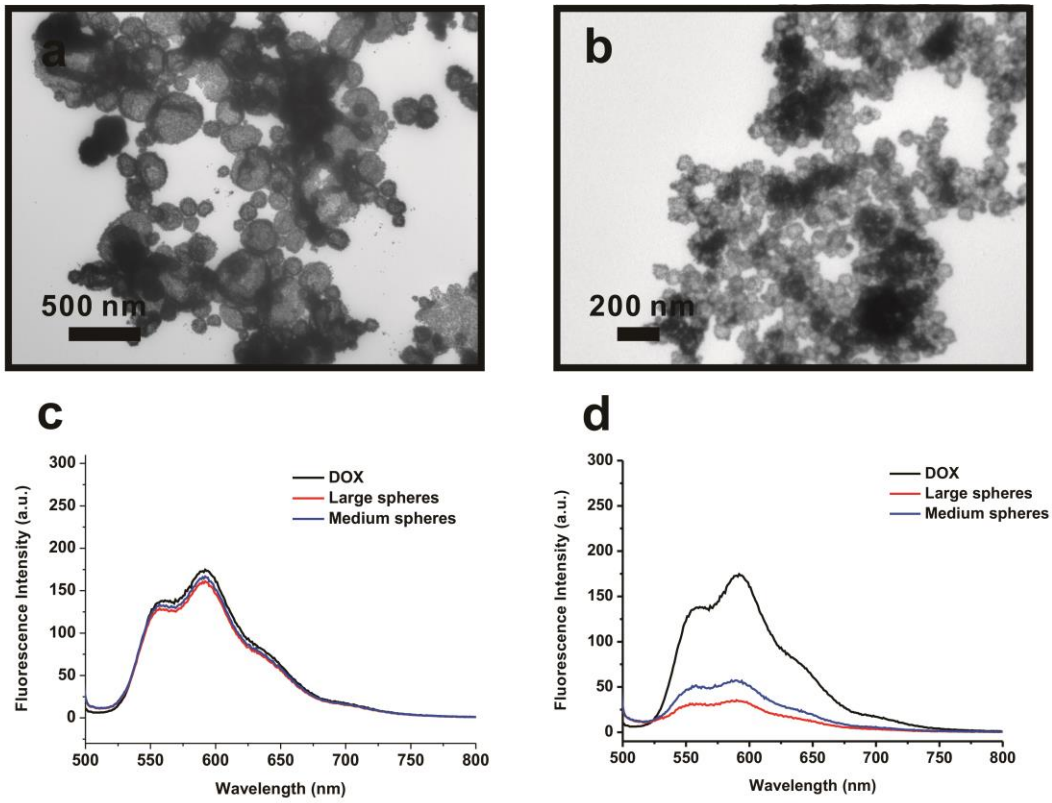

Figure 42. TEM images of DOX-loaded (a) large spheres and (b) medium spheres using *in situ* loading method; (c) Fluorescence spectra of large spheres and medium spheres using post-synthetic loading method; (d) Fluorescence spectra of as-synthesized large spheres and medium spheres using *in situ* loading method.

Ideally, the drugs should stay within the spheres without leaking during the delivery process and before they reach the targeted location. Being aware of the gaps between constitutional nanoparticles within the superstructures, I was concerned about the leakage of the drug molecules. Therefore, I performed drug leakage tests in different buffers. The DOX-loaded spheres were prepared, separated and washed by centrifugation. The remaining solid was re-dispersed in fresh 0.1 M HEPES buffer (pH = 7) or 0.1 M PBS buffer (pH = 7). The cumulative leakage was investigated at different time points. At each time point, the solution was centrifuged and the amount of DOX released in the supernatant was determined by comparing its absorbance at 485 nm with the calibration curves of DOX using UV-Vis spectrometer. After each time point, the remaining solid was re-dispersed in fresh buffers. I did observe some leakage of drugs for both large spheres and medium spheres in HEPES buffer and PBS buffer (**Figure 43a-b**). The cumulative release profiles indicate continuous leakage within the first 9 hours for both large spheres and medium spheres in either HEPES buffer or PBS buffer. In both buffers, large spheres show faster and slightly more leakage than medium spheres. After 32 hours, the final cumulative leakage for large spheres and medium spheres are ~17% and ~13% in HEPES buffer, and ~16% and ~14% in PBS buffer. Since tumor tissues are usually acidic by hypoxia,[152] I also performed the leakage test in acetate buffer (pH = 5) to check whether acidic conditions could induce the degradation of these spherical assemblies to release more drug (**Figure 43c**). However, the test shows similar result with those performed in HEPES buffer and PBS buffer. In acetate buffer, the final cumulative leakage for large spheres and medium spheres are ~20% and ~16%, respectively. The leakage for both large and medium spheres in all three buffers are comparable with the reported vesicular gold nanorod assemblies,[33] but much smaller

than the leakage for soft vesicular drug carriers, such as liposomes which exhibit poor stability under the physiological conditions.[143,158]

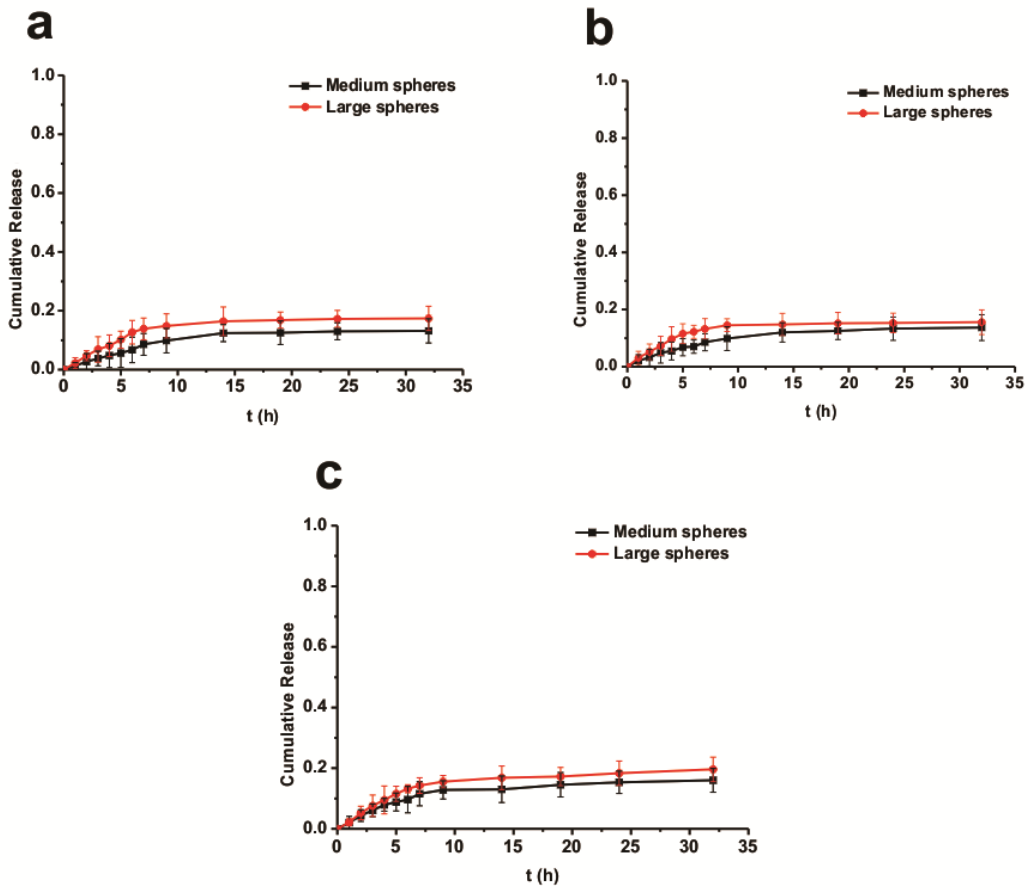

Figure 43. Leakage test of large spheres and medium spheres in different buffers: (a) HEPES buffer (pH = 7); (b) PBS buffer (pH =7); (c) Acetate buffer (pH = 5).

I already demonstrated that proteinase K can induce the degradation of large spheres but is not effective against medium spheres. I next tested whether proteinase K has a similar influence on drug-loaded spheres. To the as-synthesized DOX-loaded spheres solution, 5 μl of 20 mg/ml proteinase K was directly added. Thereafter, the mixture was incubated at 37 ℃ for up

to 34 h. The release of DOX was determined by measuring the absorption of free DOX at 485 nm in the supernatant after centrifugation. For the large spheres, the cumulative release profile shows continuous release of DOX until it reaches ~70% after 7 hours. Thereafter, DOX continues to be released, albeit much more slowly compared to the initial rapid release. (**Figure 44a**). A cumulative DOX release of ~73% is achieved after 37 hours. However, DOX-loaded medium spheres show only limited release within the first ~6 hours and a final cumulative DOX release of 15%, which is comparative to result of the leakage test in HPEPS buffer and PBS buffer (**Figure 44a**). Therefore, I speculate that the drug release from the medium spheres is mainly due to leakage rather than degradation of the superstructure. Cumulative release profiles of large spheres and medium spheres in PBS buffer (pH = 7) with the addition of proteinase K were also collected and gave similar results with those in HEPES buffer (**Figure 44b**). The final cumulative release of DOX after 32 hours is ~71% for large spheres and ~14% for medium spheres, respectively. Fluorescence spectrometry was utilized to monitor the release of DOX from as-synthesized drug-loaded spheres upon the addition of proteinase K (**Figure 44c-d**). The fluorescence spectra show consistent results with the cumulative release profiles of large spheres and medium spheres. All of these results indicate the drug-loaded medium spheres are stable in the presence of enzyme while large spheres are not.

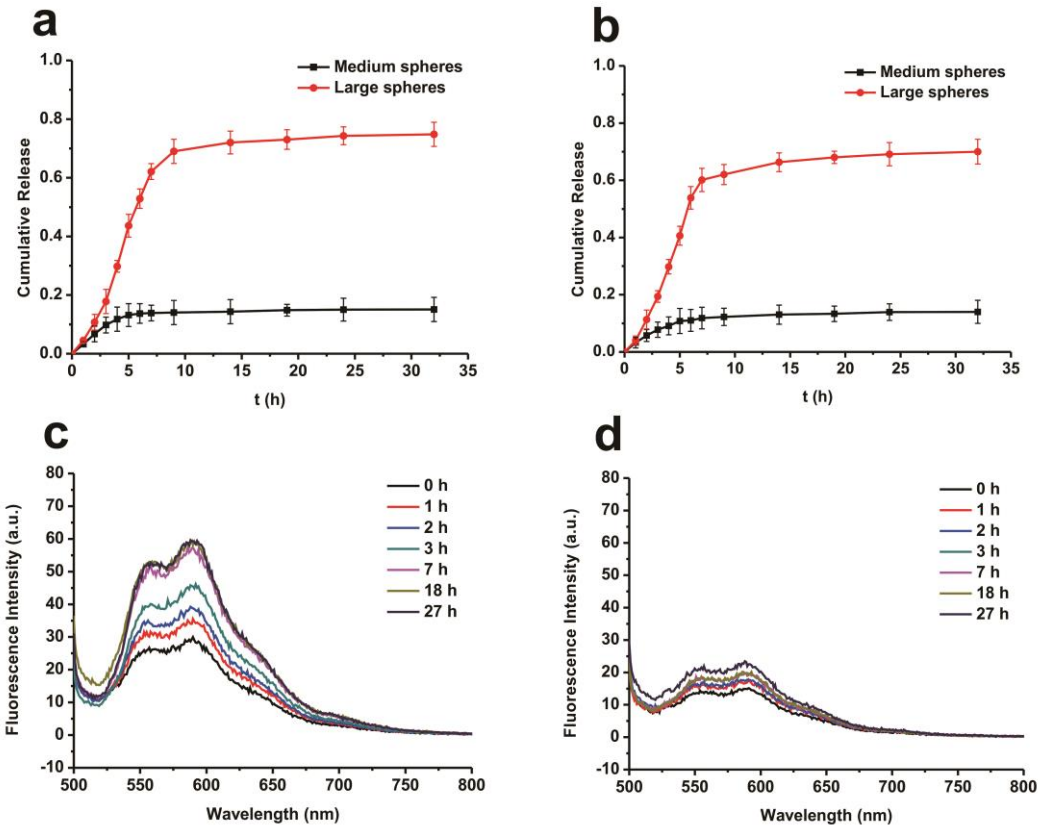

Figure 44. Cumulative release profile with the addition of proteinase K for large spheres and medium spheres in (a) HEPES buffer or (b) PBS buffer. Time-dependent fluorescence spectra with the addition of proteinase K for (c) large spheres and (d) medium spheres.

Next, I applied laser irradiation at 805 nm and power of 2.49 W to the drug-loaded spheres for 10 minutes. Large spheres show a final drug release of 82% and medium spheres show the release of 69%. TEM indicates that the spheres degrade under this condition (**Figure 45a-b**). In addition, fluorescence spectra show that the fluorescence of DOX is recovered after laser irradiation for both large spheres and medium spheres (**Figure 45c-d**). All of these data indicate that laser irradiation in this condition is effective to induce the degradation of both large spheres and medium spheres and triggers drug release.

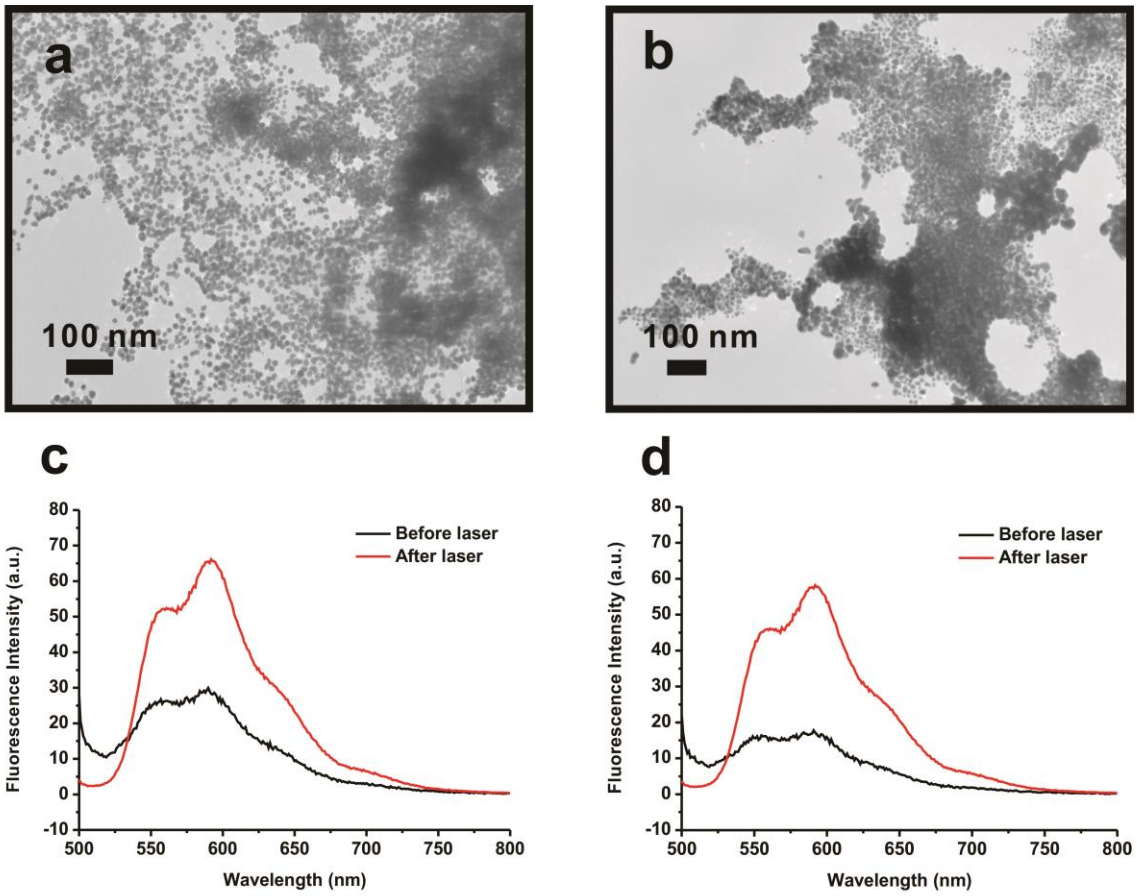

Figure 45. TEM images of (a) large spheres and (b) medium spheres with laser irradiation at 805 nm for 10 minutes. Fluorescence spectra of (c) large spheres and (d) medium spheres before and after laser irradiation at 805 nm for 10 minutes.

4.3 CONCLUSION

In summary, I have successfully prepared spherical gold nanoparticle superstructures with varied diameters and Vis-NIR extinction and loaded the spheres with an anticancer drug during the synthesis. Their size-dependent enzymatic stability and triggered drug release using laser irradiation are demonstrated.

4.4 EXPERIMENTAL SECTION

4.4.1 Materials and methods

All solvents and chemicals were obtained from commercial sources and used without further purification. 0.1M HEPES Buffer (HEPES = 4-(2-hydroxyethyl)-1-piperazineethanesulfonic acid) was made by directly diluting 1.0 M HEPES buffer (pH = 7.3 ± 0.1; Fisher Scientific) with water (NANOpure, Barnstead DiamondTM System.; 18.2 MΩ). Peptide (AAAYSSGAPPMPPF or AA-PEP_{Au}) was synthesized and purified by New England Peptide with final purity of 99%. Reverse-phase high-pressure liquid chromatography (HPLC) was performed at ambient temperature with an Agilent 1200 liquid chromatographic system equipped with diode array and multiple wavelength detectors using a Grace Vydac protein C4 column (214TP1010, 1.0 cm × 25 cm). Transmission electron microscopy (TEM) samples were prepared by pipetting one drop of solution onto a 3-mm-diameter copper grid coated with carbon film. TEM was conducted on either a JEOL 200CX instrument operated at 200 kV and equipped with a Gatan CCD image system or FEI Morgagni 268 operated at 80kV and equipped with an AMT side mount CCD camera system. UV-Vis spectra were collected using an Agilent 8453 UV-Vis Spectrometer with a quartz cuvette (10 mm path length) at room temperature. A commercial Ti:Sapphire laser with a 5 kHz repetition rate was used to generate 100 fs 805 nm laser pulses. A seed pulse from a mode-locked Ti:Sapphire oscillator (Coherent Vitesse) is amplified by a chirped-pulsed system (Coherent Legend Elite), which is pumped by a frequency doubled Nd:YLF laser. The resulting pulses were directed through a 1 cm iris immediately before the sample. Average laser power

was measured at the sample, using a thermopile detector (Coherent PowerMax). The 2.59 W average power is 0.660 mJ cm^{-2} / pulse and the 1.25 W average power is 0.318 mJ cm^{-2} / pulse.

4.4.2 Preparation of large spheres or DOX-loaded large spheres using *in situ* loading method

C_6-AA-PEP_{Au} was synthesized using the previously reported method. Lyophilized C_6-AA-PEP_{Au} (~1.87×10^{-8} mol) was completely dissolved in 110 μL 0.1 M HEPES buffer and 15 μl 1.0 M TEAA buffer in a plastic vial. (For DOX-loaded large spheres, 2 μL 1 mg/mL aqueous doxorubicin hydrochloride solution was added and vortexed at this time.) This solution was allowed to incubate for 30 min. Thereafter, 4 μl of 0.01 M chloroauric acid ($HAuCl_4$) aqueous solution was added to the above solution. The mixture was immediately vortexed for 1 min. and then left undisturbed at room temperature for one day. Products from multiple syntheses were studied using TEM and UV-Vis spectroscopy.

4.4.3 Preparation of medium spheres or DOX-loaded medium spheres using *in situ* loading method

Lyophilized C_6-AA-PEP_{Au} (~1.87×10^{-8} mol) was completely dissolved in 125 μL 0.1 M HEPES buffer in a plastic vial. (For DOX-loaded medium spheres, 2 μL 1 mg/mL aqueous doxorubicin hydrochloride solution was added and vortexed at this time.) This solution was allowed to incubate for 30 min. During the 30 min. incubation time, a fresh gold ion precursor solution was prepared: 0.1M chloroauric acid ($HAuCl_4$) in 1.0 M triethylammonium acetate (TEAA; pH = 7.0) buffer was incubated for 10 min. at room temperature. Thereafter, this

mixture was centrifuged (10 min., 5K rpm). After the 30 min. peptide solution incubation period, 0.7 μL of the supernatant of the centrifuged gold ion precursor solution was added to the peptide conjugate solution. The mixture was immediately vortexed for 1 min. and then left undisturbed at room temperature for one day. Products from multiple syntheses were studied using TEM and UV-Vis spectroscopy.

4.4.4 Enzyme treatment of spheres

To the as-synthesized spheres or DOX-loaded spheres solution, 5 μl of 20 mg/ml Proteinase K was directly added. The mixture was incubated at 37 ℃ for up to 27 h. UV-Vis spectrum was taken at different time points.

4.4.5 Enzyme treatment of DOX-loaded spheres

To the as-synthesized spheres or DOX-loaded spheres solution, 5 μl of 20 mg/ml Proteinase K was directly added. The mixture was incubated at 37 ℃ for up to 32 h. The release profiles of DOX were investigated in HEPES buffer (pH = 7) and PBS buffer (pH = 7). At each time point, the solution was centrifuged and the amount of DOX released in the supernatant was determined by comparing its absorbance at 485 nm with the calibration curves of DOX using UV-Vis spectrometer. After each time points, the remained solid was re-disperseded in fresh buffer solution with the addition of 5 μl of 20 mg/ml Proteinase K (1~2 seconds of sonication were employed for better dipersion). Leakage test were performed in HEPES buffer (pH = 7), PBS buffer (pH = 7) and acetate buffer (pH = 5). All measurements were conducted in triplicate.

4.4.6 Laser treatment of spheres or DOX-loaded spheres

To the as-synthesized spheres or DOX-loaded spheres solution, laser irradiation at 805 nm was applied. Tests with different powers and irradiation time were performed.

4.4.7 Determination of loading efficiency

See **Scheme 4**, where m_0 is the initial amount of DOX added, m_1, m_2, and m_3 are the amount of DOX washed away after centrifugation.

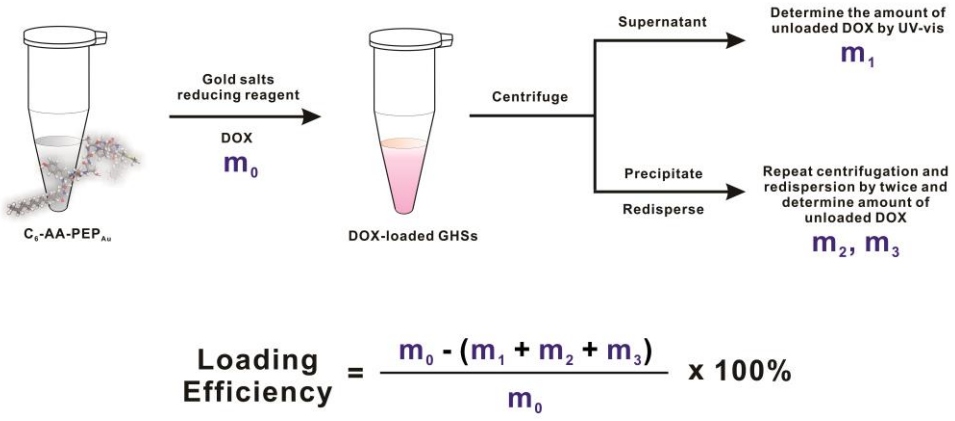

$$\text{Loading Efficiency} = \frac{m_0 - (m_1 + m_2 + m_3)}{m_0} \times 100\%$$

Scheme 4. Scheme demonstrating the determination of loading efficiency.

5.0 SUMMARY

The work presented in this thesis focused on assembling and controlling the morphologies, metrics, and properties of gold nanoparticle superstructures and studying their applications. I demonstrated that modifications to the peptide sequences and careful control over the reaction conditions can affect the final structure of nanoparticle assemblies.

In Chapter 2, I showed that the inter-fiber interaction was enhanced by modifying the C-terminus of C_{12}-PEP_{Au} with additional hydrophobic phenylalanine residues, leading to fiber bundling and in turn the formation of thick or intertwined 1-D nanoparticle superstructures. This is an example of how modifications to the C-terminus of peptide conjugates can be utilized as another way to affect the structure of nanoparticle superstructures and their co-assembly into larger-scale structures.

In Chapter 3, I emphasized the significance of controlling reaction conditions in order to control the diameters of hollow spherical gold nanoparticle superstructures. By using a single peptide conjugate, C_6-AA-PEP_{Au}, hollow spherical gold nanoparticle superstructures with varied diameters (~40 nm, ~75 nm, and ~150 nm) and SPR responses were prepared. Medium (~75 nm) and large (~150 nm) spheres exhibit broad SPR extinction in the NIR window (650-900 nm). By coupling the experiment and theoretical simulation, I concluded that the large SPR red-shifting of the medium and large spheres might be due to their possible quasi-continuous shell structure with defects such as pinholes.

In Chapter 4, I utilized these spherical nanoparticle superstructures as drug carriers and studied their size-dependent enzymatic stability and laser-induced drug release properties, which was the first demonstrated application of these spherical nanoparticle superstructures. I found that large spheres can be deconstructed by enzymatic degradation and laser irradiation while the disassembly of medium spheres can only occur under laser irradiation. I also showed that NIR irradiation induces drug-release from both medium and large spheres, which points toward their potential as materials for biomedicine related applications.

Grouped with previous work in Rosi Group, I have demonstrated the use of peptide-based approaches for the synthesis and assembly of complex nanoparticle-based superstructures with controlled morphologies, compositions, metrics, and properties. Modifications to the molecular structure of peptide conjugates and control over the reaction conditions have been introduced as two major ways to affect the final structure and properties of the nanoparticle assemblies, which can be further explored in the future. For example, modifications to the N- or C-terminus of peptide sequences with different numbers of hydrophobic (e.g., phenylalanine) or hydrophilic (e.g., glutamic acid) amino acids will significantly affect the assembling ability of peptide conjugates. More importantly, the organic tail can be tuned to bring new assembly morphologies and properties. Segments responsive to external stimuli can be coupled with peptide conjugates to potentially prepare ‘dynamic’ structures. Other biomolecules such as DNA strands and biotinylated molecules can be attached to the peptide sequences to endow the bioconjugates with new properties. As for tuning the reaction conditions, various buffer ingredients (HEPES buffer, citrate buffer, TEAA buffer, Tris buffer, PBS buffer, etc.), solvent (aqueous buffer, THF, DMF, mixed solvents, etc.) and other factors (pH, temperature, light, magnetic field, etc.) can be explored.

APPENDIX

a

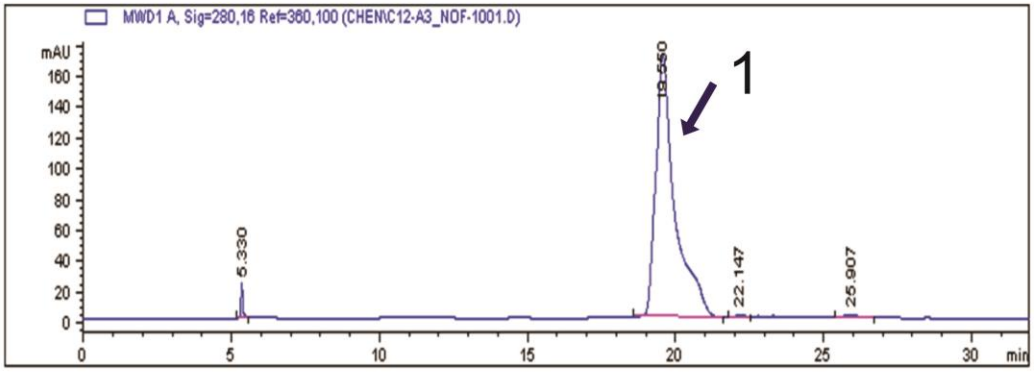
MWD1 A, Sig=280,16 Ref=360,100 (CHEN\C12-A3_NOF-1001.D)
mAU
19.560
1
5.330
22.147
25.907
min

b

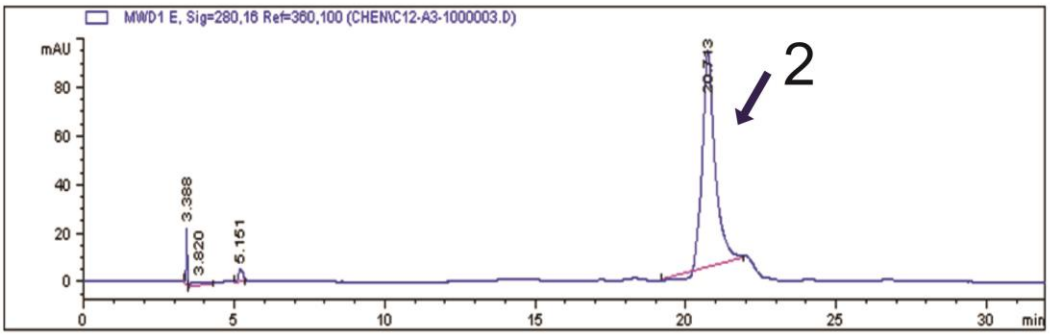
MWD1 E, Sig=280,16 Ref=360,100 (CHEN\C12-A3-1000003.D)
mAU
20.343
2
3.388
3.820
5.151
min

c

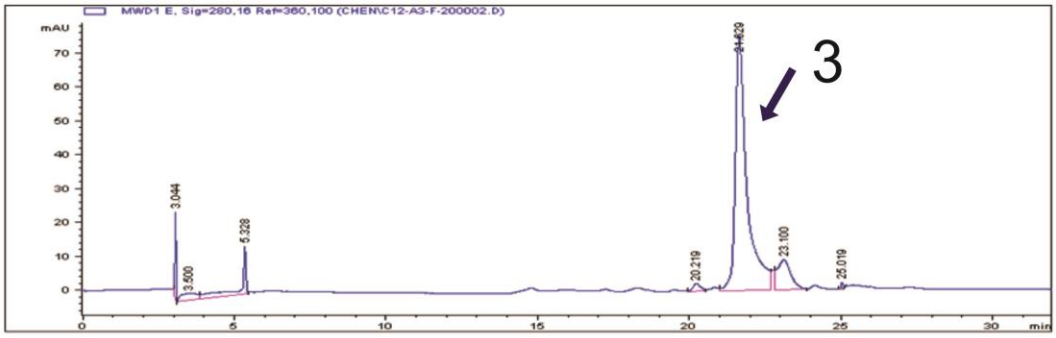
MWD1 E, Sig=280,16 Ref=360,100 (CHEN\C12-A3-F-200002.D)
mAU
3
3.044
3.500
5.328
20.219
23.100
25.019
min

d

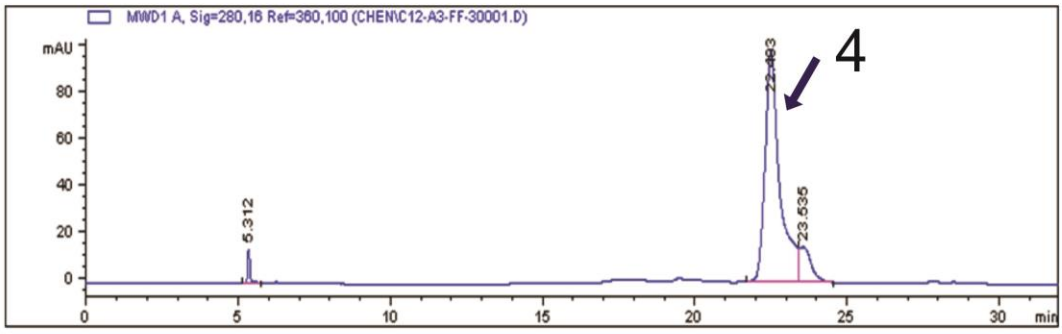
MWD1 A, Sig=280,16 Ref=360,100 (CHEN\C12-A3-FF-30001.D)
mAU
22.483
4
5.312
23.535
min

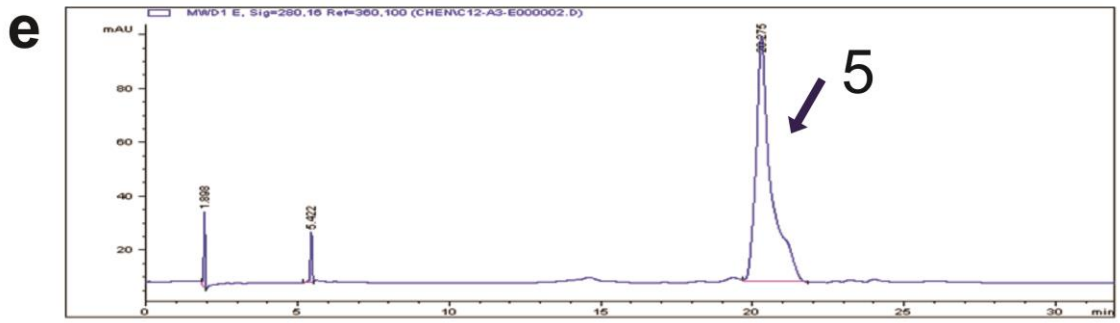

Figure 46.The reverse-phase HPLC charts for the purification of peptide conjugates **1** (a), **2** (b), **3** (c), **4** (d) and **5** (e).

a

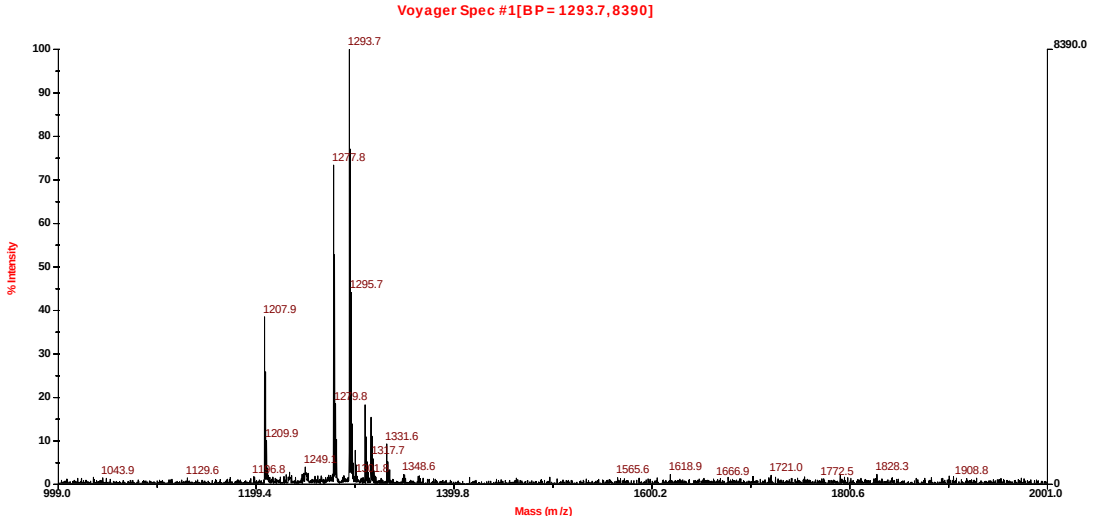
Voyager Spec #1[BP = 1293.7, 8390]
% Intensity
Mass (m/z)
1293.7
8390.0
1277.8
1295.7
1207.9
1209.9
1331.6
1317.7
1348.6
1043.9
1129.6
1565.6
1618.9
1666.9
1721.0
1772.5
1828.3
1908.8

b

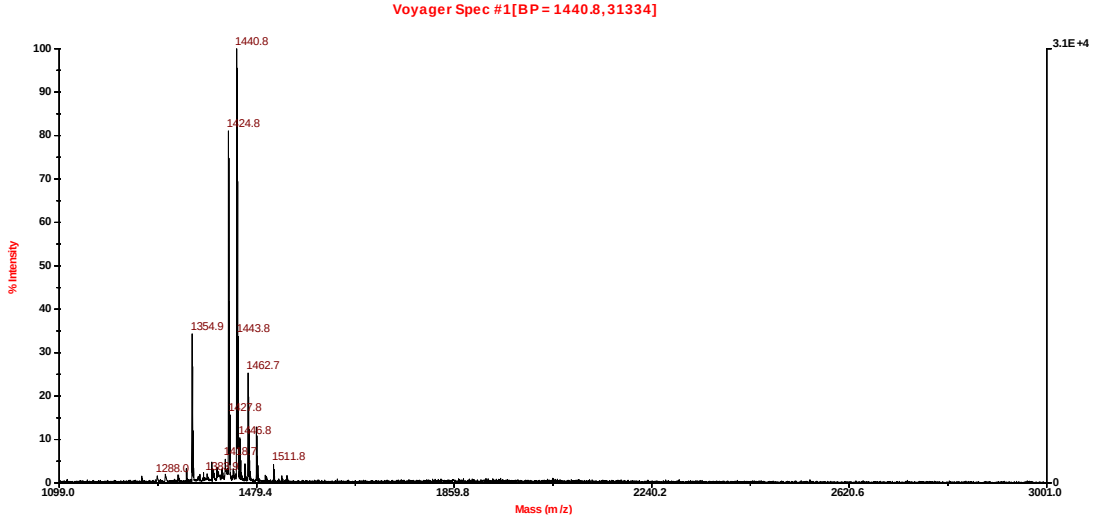
Voyager Spec #1[BP = 1440.8, 31334]
% Intensity
Mass (m/z)
1440.8
3.1E+4
1424.8
1354.9
1443.8
1462.7
1427.8
1446.8
1511.8
1288.0

c

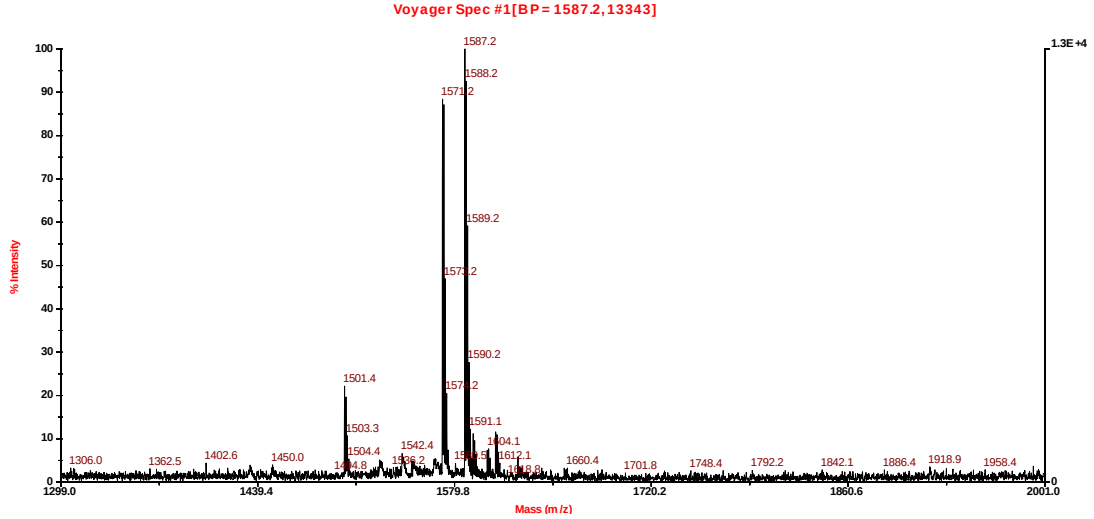
Voyager Spec #1[BP = 1587.2, 13343]
% Intensity
Mass (m/z)
1587.2
1.3E+4
1588.2
1589.2
1590.2
1591.1
1501.4
1503.3
1504.4
1542.4
1604.1
1612.1
1306.0
1362.5
1402.6
1450.0
1660.4
1701.8
1748.4
1792.2
1842.1
1886.4
1918.9
1958.4

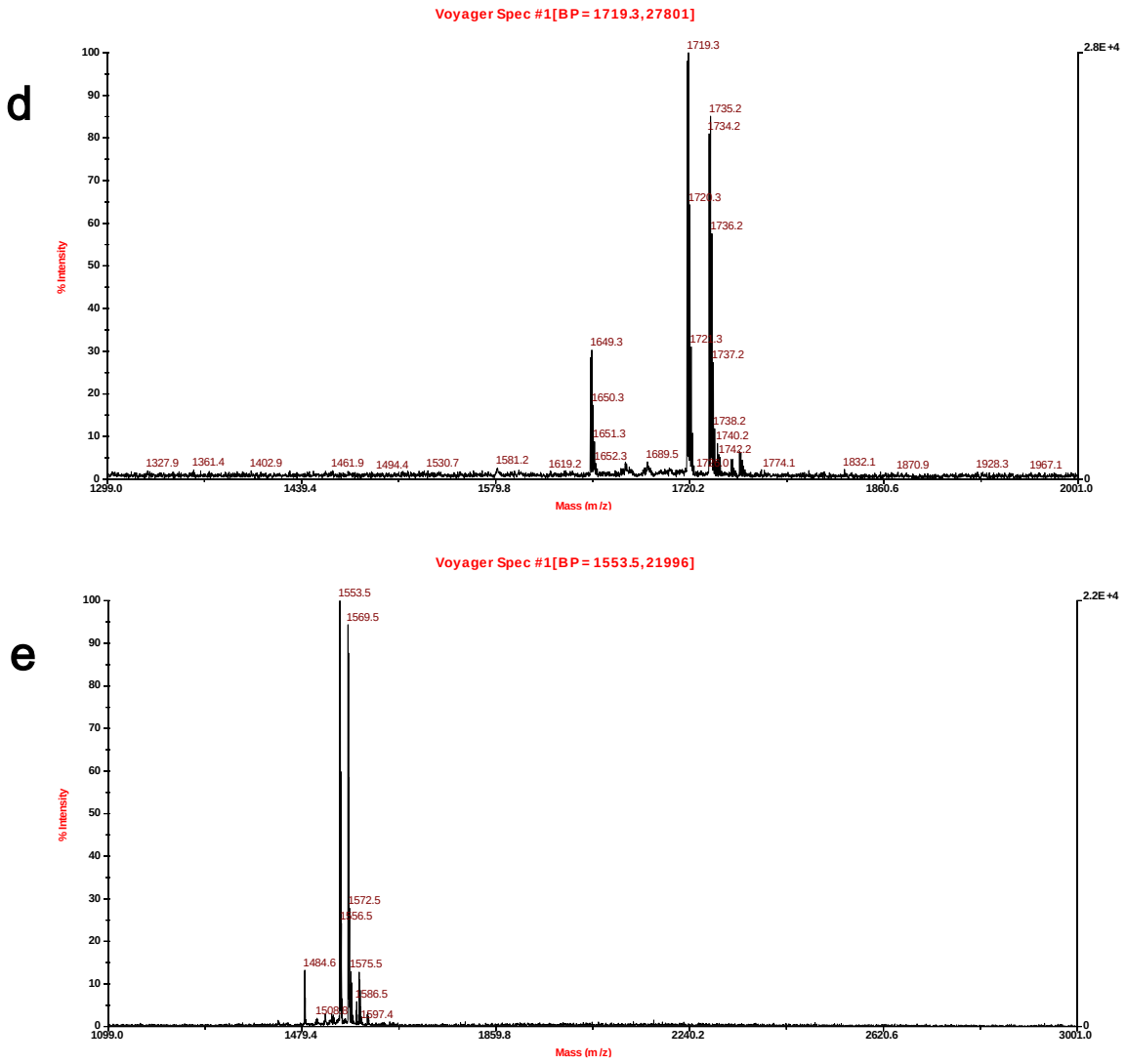

Figure 47. MALDI-TOF mass spectrum of purified peptide conjugates **1**, **2**, **3**, **4** and **5** (m/z): (a) **1**, 1277.8 (M + Na), 1293.7 (M + K); (b) **2**, 1424.8 (M + Na), 1440.8 (M + K); (c) **3**, 1571.2 (M + Na), 1587.2 (M + K); (d) **4**, 1719.3 (M + Na), 1735.2 (M + K); (e) **5**, 1553.5 (M + Na), 1569.5 (M + K).

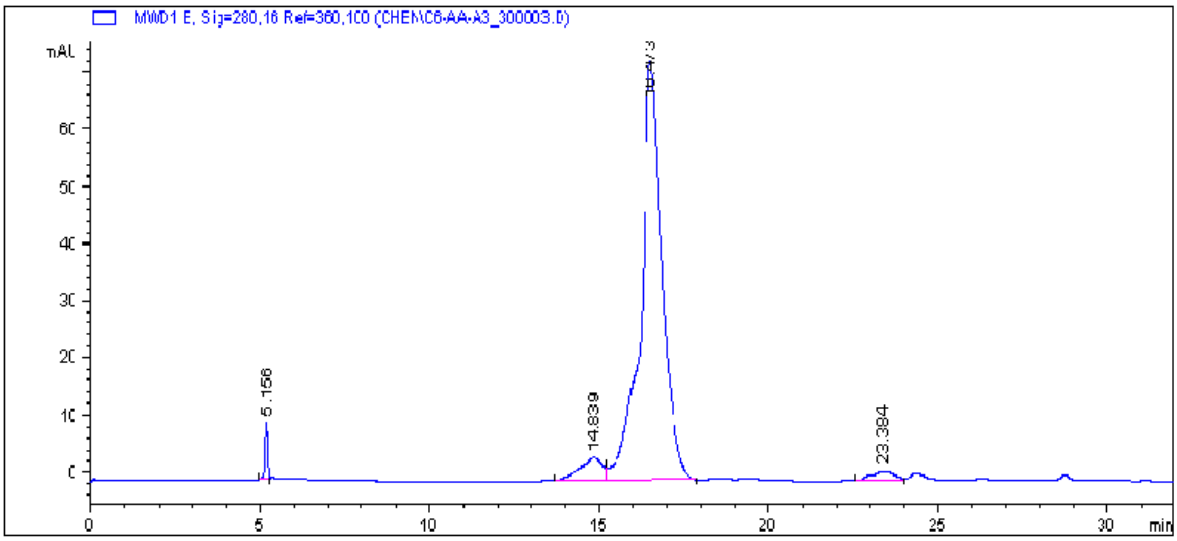

Figure 48. The reverse-phase HPLC chart for the coupling reaction of AAAYSSGAPPMPPF with caproic N-hydroxyl-succinimide ester (retention time = 16.5 min).

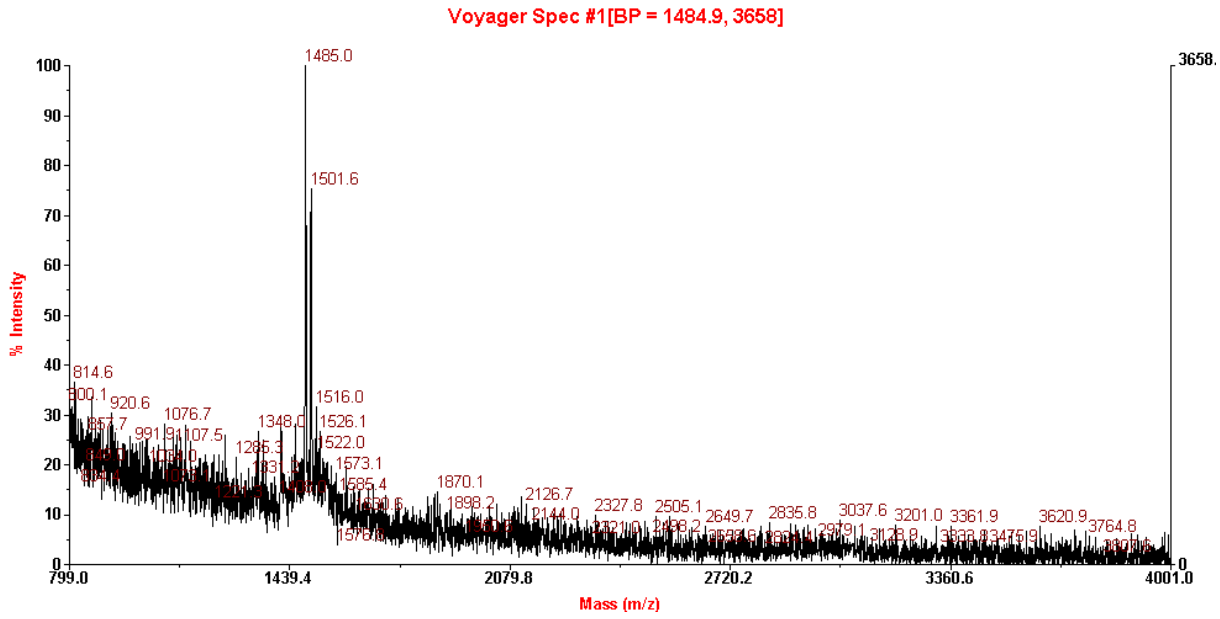

Figure 49. MALDI-TOF mass spectrum of purified C_6-AA-PEP_{Au} (m/z): 1485.0 (M + Na), 1501.6 (M + K).

BIBLIOGRAPHY

(1) Yin, Y.; Talapin, D. *Chemical Society Reviews* **2013**, *42*, 2484.

(2) Gūnes, S.; Neugebauer, H.; Sariciftci, N. S. *Chemical Reviews* **2007**, *107*, 1324.

(3) Michalet, X.; Pinaud, F. F.; Bentolila, L. A.; Tsay, J. M.; Doose, S.; Li, J. J.; Sundaresan, G.; Wu, A. M.; Gambhir, S. S.; Weiss, S. *Science* **2005**, *307*, 538.

(4) Sokolova, V.; Epple, M. *Angewandte Chemie International Edition* **2008**, *47*, 1382.

(5) Wilson, R. *Chemical Society Reviews* **2008**, *37*, 2028.

(6) Daniel, M.-C.; Astruc, D. *Chemical Reviews* **2003**, *104*, 293.

(7) Kelly, K. L.; Coronado, E.; Zhao, L. L.; Schatz, G. C. *The Journal of Physical Chemistry B* **2002**, *107*, 668.

(8) Cobley, C. M.; Chen, J.; Cho, E. C.; Wang, L. V.; Xia, Y. *Chemical Society Reviews* **2011**, *40*, 44.

(9) Link, S.; El-Sayed, M. A. *The Journal of Physical Chemistry B* **1999**, *103*, 4212.

(10) Link, S.; El-Sayed, M. A. *The Journal of Physical Chemistry B* **1999**, *103*, 8410.

(11) Brioude, A.; Jiang, X. C.; Pileni, M. P. *The Journal of Physical Chemistry B* **2005**, *109*, 13138.

(12) Burda, C.; Chen, X.; Narayanan, R.; El-Sayed, M. A. *Chemical Reviews* **2005**, *105*, 1025.

(13) Murphy, C. J.; Sau, T. K.; Gole, A. M.; Orendorff, C. J.; Gao, J.; Gou, L.; Hunyadi, S. E.; Li, T. *The Journal of Physical Chemistry B* **2005**, *109*, 13857.

(14) Hu, M.; Chen, J.; Li, Z.-Y.; Au, L.; Hartland, G. V.; Li, X.; Marquez, M.; Xia, Y. *Chemical Society Reviews* **2006**, *35*, 1084.

(15) Oldenburg, S. J.; Averitt, R. D.; Westcott, S. L.; Halas, N. J. *Chemical Physics Letters* **1998**, *288*, 243.

(16) Weissleder, R. *Nature Biotechnology* **2001**, *19*, 316.

(17) Dreaden, E. C.; Mackey, M. A.; Huang, X.; Kang, B.; El-Sayed, M. A. *Chemical Society Reviews* **2011**, *40*, 3391.

(18) Yavuz, M. S.; Cheng, Y.; Chen, J.; Cobley, C. M.; Zhang, Q.; Rycenga, M.; Xie, J.; Kim, C.; Song, K. H.; Schwartz, A. G.; Wang, L. V.; Xia, Y. *Nature Materials* **2009**, *8*, 935.

(19) Ozbay, E. *Science* **2006**, *311*, 189.

(20) Tang, Z.; Wang, Y.; Podsiadlo, P.; Kotov, N. A. *Advanced Materials* **2006**, *18*, 3203.

(21) Koole, R.; Liljeroth, P.; de Mello Donegá, C.; Vanmaekelbergh, D.; Meijerink, A. *Journal of the American Chemical Society* **2006**, *128*, 10436.

(22) Crooker, S. A.; Hollingsworth, J. A.; Tretiak, S.; Klimov, V. I. *Physical Review Letters* **2002**, *89*, 186802.

(23) Lisiecki, I.; Parker, D.; Salzemann, C.; Pileni, M. P. *Chemistry of Materials* **2007**, *19*, 4030.

(24) Lalatonne, Y.; Motte, L.; Russier, V.; Ngo, A. T.; Bonville, P.; Pileni, M. P. *The Journal of Physical Chemistry B* **2004**, *108*, 1848.

(25) Stewart, M. E.; Anderton, C. R.; Thompson, L. B.; Maria, J.; Gray, S. K.; Rogers, J. A.; Nuzzo, R. G. *Chemical Reviews* **2008**, *108*, 494.

(26) Medintz, I. L.; Uyeda, H. T.; Goldman, E. R.; Mattoussi, H. *Nature Materials* **2005**, *4*, 435.

(27) Tong, L.; Wei, Q.; Wei, A.; Cheng, J.-X. *Photochemistry and Photobiology* **2009**, *85*, 21.

(28) Srivastava, S.; Frankamp, B. L.; Rotello, V. M. *Chemistry of Materials* **2005**, *17*, 487.

(29) Ghosh, S. K.; Pal, T. *Chemical Reviews* **2007**, *107*, 4797.

(30) Klein, W. P.; Schmidt, C. N.; Rapp, B.; Takabayashi, S.; Knowlton, W. B.; Lee, J.; Yurke, B.; Hughes, W. L.; Graugnard, E.; Kuang, W. *Nano Letters* **2013**, *13*, 3850.

(31) Yao, Y.; Xue, M.; Zhang, Z.; Zhang, M.; Wang, Y.; Huang, F. *Chemical Science* **2013**, *4*, 3667.

(32) Wang, H.; Levin, C. S.; Halas, N. J. *Journal of the American Chemical Society* **2005**, *127*, 14992.

(33) Song, J.; Pu, L.; Zhou, J.; Duan, B.; Duan, H. *ACS Nano* **2013**, *7*, 9947.

(34) Chen, C.-L.; Rosi, N. L. *Angewandte Chemie International Edition* **2010**, *49*, 1924.

(35) Hildebrand, M. *Chemical Reviews* **2008**, *108*, 4855.

(36) Correa-Duarte, M. A.; Pérez-Juste, J.; Sánchez-Iglesias, A.; Giersig, M.; Liz-Marzán, L. M. *Angewandte Chemie International Edition* **2005**, *44*, 4375.

(37) Kim, Y.-H.; Nedeljković, J. M.; Ahrenkiel, S. P.; Gilbert, K. E. H.; Alleman, J. L.; Zhang, S. B.; Mićić, O. I.; Nozik, A. J.; Heben, M. J. *The Journal of Physical Chemistry B* **2006**, *110*, 25153.

(38) Wang, H.; Lin, W.; Fritz, K. P.; Scholes, G. D.; Winnik, M. A.; Manners, I. *Journal of the American Chemical Society* **2007**, *129*, 12924.

(39) Dujardin, E.; Peet, C.; Stubbs, G.; Culver, J. N.; Mann, S. *Nano Letters* **2003**, *3*, 413.

(40) Djalali, R.; Chen, Y.-f.; Matsui, H. *Journal of the American Chemical Society* **2002**, *124*, 13660.

(41) Tao, A. R.; Huang, J.; Yang, P. *Accounts of Chemical Research* **2008**, *41*, 1662.

(42) Collier, C. P.; Saykally, R. J.; Shiang, J. J.; Henrichs, S. E.; Heath, J. R. *Science* **1997**, *277*, 1978.

(43) Tao, A.; Sinsermsuksakul, P.; Yang, P. *Nature Nanotechnology* **2007**, *2*, 435.

(44) Shevchenko, E. V.; Talapin, D. V.; Kotov, N. A.; O'Brien, S.; Murray, C. B. *Nature* **2006**, *439*, 55.

(45) Courty, A.; Mermet, A.; Albouy, P. A.; Duval, E.; Pileni, M. P. *Nature Materials* **2005**, *4*, 395.

(46) Cheng, W.; Campolongo, M. J.; Cha, J. J.; Tan, S. J.; Umbach, C. C.; Muller, D. A.; Luo, D. *Nature Materials* **2009**, *8*, 519.

(47) Nie, Z.; Petukhova, A.; Kumacheva, E. *Nature Nanotechnology* **2010**, *5*, 15.

(48) Lalatonne, Y.; Richardi, J.; Pileni, M. P. *Nature Materials* **2004**, *3*, 121.

(49) Kitching, H.; Shiers, M. J.; Kenyon, A. J.; Parkin, I. P. *Journal of Materials Chemistry A* **2013**, *1*, 6985.

(50) Nie, Z.; Fava, D.; Kumacheva, E.; Zou, S.; Walker, G. C.; Rubinstein, M. *Nature Materials* **2007**, *6*, 609.

(51) Dickerson, M. B.; Sandhage, K. H.; Naik, R. R. *Chemical Reviews* **2008**, *108*, 4935.

(52) Slocik, J. M.; Stone, M. O.; Naik, R. R. *Small* **2005**, *1*, 1048.

(53) Chen, C.-L.; Zhang, P.; Rosi, N. L. *Journal of the American Chemical Society* **2008**, *130*, 13555.

(54) Naik, R. R.; Stringer, S. J.; Agarwal, G.; Jones, S. E.; Stone, M. O. *Nature Materials* **2002**, *1*, 169.

(55) Lee, S.-W.; Mao, C.; Flynn, C. E.; Belcher, A. M. *Science* **2002**, *296*, 892.

(56) Banerjee, I. A.; Yu, L.; Matsui, H. *Proceedings of the National Academy of Sciences of the United States of America* **2003**, *100*, 14678.

(57) Yu, L.; Banerjee, I. A.; Shima, M.; Rajan, K.; Matsui, H. *Advanced Materials* **2004**, *16*, 709.

(58) Reiss, B. D.; Mao, C.; Solis, D. J.; Ryan, K. S.; Thomson, T.; Belcher, A. M. *Nano Letters* **2004**, *4*, 1127.

(59) Peelle, B. R.; Krauland, E. M.; Wittrup, K. D.; Belcher, A. M. *Acta Biomaterialia* **2005**, *1*, 145.

(60) Sewell, S. L.; Wright, D. W. *Chemistry of Materials* **2006**, *18*, 3108.

(61) Lee, J.-Y.; Choo, J.-E.; Choi, Y.-S.; Park, J.-B.; Min, D.-S.; Lee, S.-J.; Rhyu, H. K.; Jo, I.-H.; Chung, C.-P.; Park, Y.-J. *Biomaterials* **2007**, *28*, 4257.

(62) Penna, M. J.; Mijajlovic, M.; Biggs, M. J. *Journal of the American Chemical Society* **2014**, *136*, 5323.

(63) Patwardhan, S. V.; Emami, F. S.; Berry, R. J.; Jones, S. E.; Naik, R. R.; Deschaume, O.; Heinz, H.; Perry, C. C. *Journal of the American Chemical Society* **2012**, *134*, 6244.

(64) Rothenstein, D.; Claasen, B.; Omiecienski, B.; Lammel, P.; Bill, J. *Journal of the American Chemical Society* **2012**, *134*, 12547.

(65) Heinz, H.; Farmer, B. L.; Pandey, R. B.; Slocik, J. M.; Patnaik, S. S.; Pachter, R.; Naik, R. R. *Journal of the American Chemical Society* **2009**, *131*, 9704.

(66) Reches, M.; Gazit, E. *Science* **2003**, *300*, 625.

(67) Hartgerink, J. D.; Beniash, E.; Stupp, S. I. *Science* **2001**, *294*, 1684.

(68) Zhao, X.; Pan, F.; Xu, H.; Yaseen, M.; Shan, H.; Hauser, C. A. E.; Zhang, S.; Lu, J. R. *Chemical Society Reviews* **2010**, *39*, 3480.

(69) Holowka, E. P.; Pochan, D. J.; Deming, T. J. *Journal of the American Chemical Society* **2005**, *127*, 12423.

(70) Silva, G. A.; Czeisler, C.; Niece, K. L.; Beniash, E.; Harrington, D. A.; Kessler, J. A.; Stupp, S. I. *Science* **2004**, *303*, 1352.

(71) Niece, K. L.; Hartgerink, J. D.; Donners, J. J. J. M.; Stupp, S. I. *Journal of the American Chemical Society* **2003**, *125*, 7146.

(72) Chen, C.-L.; Rosi, N. L. *Journal of the American Chemical Society* **2010**, *132*, 6902.

(73) Song, C.; Blaber, M. G.; Zhao, G.; Zhang, P.; Fry, H. C.; Schatz, G. C.; Rosi, N. L. *Nano Letters* **2013**, *13*, 3256.

(74) Song, C.; Zhao, G.; Zhang, P.; Rosi, N. L. *Journal of the American Chemical Society* **2010**, *132*, 14033.
(75) Hwang, L.; Zhao, G.; Zhang, P.; Rosi, N. L. *Small* **2011**, *7*, 1939.
(76) Cortie, M. B.; McDonagh, A. M. *Chemical Reviews* **2011**, *111*, 3713.
(77) Ray, P. C. *Chemical Reviews* **2010**, *110*, 5332.
(78) Buck, M. R.; Bondi, J. F.; Schaak, R. E. *Nature Chemistry* **2012**, *4*, 37.
(79) Jones, M. R.; Osberg, K. D.; Macfarlane, R. J.; Langille, M. R.; Mirkin, C. A. *Chemical Reviews* **2011**, *111*, 3736.
(80) Ofir, Y.; Samanta, B.; Rotello, V. M. *Chemical Society Reviews* **2008**, *37*, 1814.
(81) Kotov, N. A.; Stellacci, F. *Advanced Materials* **2008**, *20*, 4221.
(82) Rubio-Martínez, M.; Puigmartí-Luis, J.; Imaz, I.; Dittrich, P. S.; Maspoch, D. *Small* **2013**, *24*, 4160.
(83) Hwang, L.; Chen, C.-L.; Rosi, N. L. *Chemical Communications* **2011**, *47*, 185.
(84) Song, C.; Wang, Y.; Rosi, N. L. *Angewandte Chemie International Edition* **2013**, *52*, 3993.
(85) Dong, H.; Paramonov, S. E.; Hartgerink, J. D. *Journal of the American Chemical Society* **2008**, *130*, 13691.
(86) Nonoyama, T.; Tanaka, M.; Inai, Y.; Higuchi, M.; Kinoshita, T. *ACS Nano* **2011**, *5*, 6174.
(87) Bowerman, C. J.; Nilsson, B. L. *Journal of the American Chemical Society* **2010**, *132*, 9526.
(88) Dong, J.; Shokes, J. E.; Scott, R. A.; Lynn, D. G. *Journal of the American Chemical Society* **2006**, *128*, 3540.
(89) Dublin, S. N.; Conticello, V. P. *Journal of the American Chemical Society* **2007**, *130*, 49.
(90) Kühnle, R. I.; Börner, H. G. *Angewandte Chemie International Edition* **2011**, *50*, 4499.
(91) Aggeli, A.; Bell, M.; Carrick, L. M.; Fishwick, C. W. G.; Harding, R.; Mawer, P. J.; Radford, S. E.; Strong, A. E.; Boden, N. *Journal of the American Chemical Society* **2003**, *125*, 9619.
(92) Muraoka, T.; Cui, H.; Stupp, S. I. *Journal of the American Chemical Society* **2008**, *130*, 2946.
(93) Collier, J. H.; Hu, B. à; Ruberti, J. W.; Zhang, J.; Shum, P.; Thompson, D. H.; Messersmith, P. B. *Journal of the American Chemical Society* **2001**, *123*, 9463.
(94) Pires, M. M.; Chmielewski, J. *Journal of the American Chemical Society* **2009**, *131*, 2706.
(95) Lee, O.-S.; Stupp, S. I.; Schatz, G. C. *Journal of the American Chemical Society* **2011**, *133*, 3677.
(96) Fry, H. C.; Garcia, J. M.; Medina, M. J.; Ricoy, U. M.; Gosztola, D. J.; Nikiforov, M. P.; Palmer, L. C.; Stupp, S. I. *Journal of the American Chemical Society* **2012**, *134*, 14646.
(97) Aida, T.; Meijer, E. W.; Stupp, S. I. *Science* **2012**, *335*, 813.
(98) Paramonov, S. E.; Jun, H.-W.; Hartgerink, J. D. *Journal of the American Chemical Society* **2006**, *128*, 7291.
(99) Soukoulis, C. M.; Wegener, M. *Nature Photonics* **2011**, *5*, 523.
(100) Pendry, J. B. *Science* **2004**, *306*, 1353.

(101) Aravinda, S.; Shamala, N.; Das, C.; Sriranjini, A.; Karle, I. L.; Balaram, P. *Journal of the American Chemical Society* **2003**, *125*, 5308.

(102) Kar, K.; Ibrar, S.; Nanda, V.; Getz, T. M.; Kunapuli, S. P.; Brodsky, B. *Biochemistry* **2009**, *48*, 7959.

(103) Stendahl, J. C.; Rao, M. S.; Guler, M. O.; Stupp, S. I. *Advanced Functional Materials* **2006**, *16*, 499.

(104) Xie, J.; Lee, J. Y.; Wang, D. I. C. *Chemistry of Materials* **2007**, *19*, 2823.

(105) Yu, J.; Becker, M. L.; Carri, G. A. *Small* **2010**, *6*, 2242.

(106) He, J.; Huang, X.; Li, Y.-C.; Liu, Y.; Babu, T.; Aronova, M. A.; Wang, S.; Lu, Z.; Chen, X.; Nie, Z. *Journal of the American Chemical Society* **2013**, *135*, 7974.

(107) Huang, P.; Lin, J.; Li, W.; Rong, P.; Wang, Z.; Wang, S.; Wang, X.; Sun, X.; Aronova, M.; Niu, G.; Leapman, R. D.; Nie, Z.; Chen, X. *Angewandte Chemie International Edition* **2013**, *52*, 13958.

(108) Song, J.; Cheng, L.; Liu, A.; Yin, J.; Kuang, M.; Duan, H. *Journal of the American Chemical Society* **2011**, *133*, 10760.

(109) Song, J.; Zhou, J.; Duan, H. *Journal of the American Chemical Society* **2012**, *134*, 13458.

(110) Niikura, K.; Iyo, N.; Higuchi, T.; Nishio, T.; Jinnai, H.; Fujitani, N.; Ijiro, K. *Journal of the American Chemical Society* **2012**, *134*, 7632.

(111) Sanson, C.; Diou, O.; Thévenot, J.; Ibarboure, E.; Soum, A.; Brûlet, A.; Miraux, S.; Thiaudière, E.; Tan, S.; Brisson, A.; Dupuis, V.; Sandre, O.; Lecommandoux, S. *ACS Nano* **2011**, *5*, 1122.

(112) Hickey, R. J.; Haynes, A. S.; Kikkawa, J. M.; Park, S.-J. *Journal of the American Chemical Society* **2011**, *133*, 1517.

(113) Caruso, F.; Caruso, R. A.; Mohwald, H. *Science* **1998**, *282*, 1111.

(114) He, J.; Liu, Y.; Babu, T.; Wei, Z.; Nie, Z. *Journal of the American Chemical Society* **2012**, *134*, 11342.

(115) Yeh, Y.-C.; Tang, R.; Mout, R.; Jeong, Y.; Rotello, V. M. *Angewandte Chemie International Edition* **2014**, *53*, 5137.

(116) Song, C.; Wang, Y.; Rosi, N. L. *Angewandte Chemie International Edition* **2013**, 52, 3993.

(117) Mühlig, S.; Cunningham, A.; Scheeler, S.; Pacholski, C.; Bürgi, T.; Rockstuhl, C.; Lederer, F. *ACS Nano* **2011**, *5*, 6586.

(118) Sheikholeslami, S. N.; Alaeian, H.; Koh, A. L.; Dionne, J. A. *Nano Letters* **2013**, *13*, 4137.

(119) Nie, Z. H.; Petukhova, A.; Kumacheva, E. *Nature Nanotechnology* **2010**, *5*, 15.

(120) Whaley, S. R.; English, D. S.; Hu, E. L.; Barbara, P. F.; Belcher, A. M. *Nature* **2000**, *405*, 665.

(121) Pacardo, D. B.; Sethi, M.; Jones, S. E.; Naik, R. R.; Knecht, M. R. *ACS Nano* **2009**, *3*, 1288.

(122) Chiu, C.-Y.; Li, Y.; Ruan, L.; Ye, X.; Murray, C. B.; Huang, Y. *Nature Chemistry* **2011**, *3*, 393.

(123) Zhang, C.; Song, C.; Fry, H. C.; Rosi, N. L. *Chemistry – A European Journal* **2014**, *20*, 941.

(124) Habib, A.; Tabata, M.; Wu, Y. G. *Bulletin of the Chemical Society of Japan* **2005**, *78*, 262.

(125) Wang, H.; Kundu, J.; Halas, N. J. *Angewandte Chemie International Edition* **2007**, *46*, 9040.

(126) Xu, Y. L. *Applied Optics* **1995**, *34*, 4573.

(127) Xu, Y. L. *Applied Optics* **1997**, *36*, 9496.

(128) Xu, Y. L.; Wang, R. T. *Physical Review E* **1998**, *58*, 3931.

(129) Yoon, J. H.; Zhou, Y.; Blaber, M. G.; Schatz, G. C.; Yoon, S. *Journal of Physical Chemistry Letters* **2013**, *4*, 1371.

(130) Johnson, P. B.; Christy, R. W. *Physical Review B* **1972**, *6*, 4370.

(131) Kreibig, U.; Fragstein, C. V. *Zeitschrift für Physik* **1969**, *224*, 307.

(132) Coronado, E. A.; Schatz, G. C. *Journal of Chemical Physics* **2003**, *119*, 3926.

(133) Moroz, A. *Journal of Physical Chemistry C* **2008**, *112*, 10641.

(134) Reinhard, B. M.; Siu, M.; Agarwal, H.; Alivisatos, A. P.; Liphardt, J. *Nano Letters* **2005**, *5*, 2246.

(135) Zuloaga, J.; Prodan, E.; Nordlander, P. *Nano Letters* **2009**, *9*, 887.

(136) Tan, S. F.; Wu, L.; Yang, J. K. W.; Bai, P.; Bosman, M.; Nijhuis, C. A. *Science* **2014**, *343*, 1496.

(137) Esteban, R.; Borisov, A. G.; Nordlander, P.; Aizpurua, J. *Nature Communications* **2012**, *3*.

(138) Hao, E.; Li, S. Y.; Bailey, R. C.; Zou, S. L.; Schatz, G. C.; Hupp, J. T. *Journal of Physical Chemistry B* **2004**, *108*, 1224.

(139) Bohren, C. F.; Huffman, D. R. *Absorption and scattering of light by small particles*; Wiley Interscience: New York, 1983.

(140) *Journal of Nanomaterials* **2011**, *2011*.

(141) Haag, R.; Kratz, F. *Angewandte Chemie International Edition* **2006**, *45*, 1198.

(142) Semete, B.; Booysen, L.; Lemmer, Y.; Kalombo, L.; Katata, L.; Verschoor, J.; Swai, H. S. *Nanomedicine : nanotechnology, biology, and medicine* **2010**, *6*, 662.

(143) Sharma, A.; Sharma, U. S. *International Journal of Pharmaceutics* **1997**, *154*, 123.

(144) Fricker, G.; Kromp, T.; Wendel, A.; Blume, A.; Zirkel, J.; Rebmann, H.; Setzer, C.; Quinkert, R.-O.; Martin, F.; Müller-Goymann, C. *Pharmaceutical Research* **2010**, *27*, 1469.

(145) Castro, G. A.; Orefice, R. L.; Vilela, J. M. C.; Andrade, M. S.; Ferreira, L. A. M. *Journal of Microencapsulation* **2007**, *24*, 395.

(146) Schaffazick, S. R.; Pohlmann, A. R.; de Cordova, C. A. S.; Creczynski-Pasa, T. B.; Guterres, S. S. *International Journal of Pharmaceutics* **2005**, *289*, 209.

(147) Dreaden, E. C.; Austin, L. A.; Mackey, M. A.; El-Sayed, M. A. *Therapeutic Delivery* **2012**, *3*, 457.

(148) Hu, J.; Wu, T.; Zhang, G.; Liu, S. *Journal of the American Chemical Society* **2012**, *134*, 7624.

(149) He, J.; Wei, Z.; Wang, L.; Tomova, Z.; Babu, T.; Wang, C.; Han, X.; Fourkas, J. T.; Nie, Z. *Angewandte Chemie International Edition* **2013**, *52*, 2463.

(150) Rasch, M. R.; Rossinyol, E.; Hueso, J. L.; Goodfellow, B. W.; Arbiol, J.; Korgel, B. A. *Nano Letters* **2010**, *10*, 3733.

(151) Zhang, C.; Zhou, Y.; Merg, A.; Song, C.; Schatz, G. C.; Rosi, N. L. *Nanoscale* **2014**, *6*, 12328.

(152) Nam, J.; Won, N.; Jin, H.; Chung, H.; Kim, S. *Journal of the American Chemical Society* **2009**, *131*, 13639.

(153) Hartgerink, J. D.; Beniash, E.; Stupp, S. I. *Proceedings of the National Academy of Sciences* **2002**, *99*, 5133.

(154) Betzel, C.; Pal, G. P.; Saenger, W. *European Journal of Biochemistry* **1988**, *178*, 155.

(155) Lucas, T. M.; James, K. T.; Beharic, J.; Moiseeva, E. V.; Keynton, R. S.; apos; Toole, M. G.; Harnett, C. K. *Applied Physics Letters* **2014**, *104*, 011909.

(156) Leung, S. J.; Kachur, X. M.; Bobnick, M. C.; Romanowski, M. *Advanced Functional Materials* **2011**, *21*, 1113.

(157) Jin, Y.; Gao, X. *Journal of the American Chemical Society* **2009**, *131*, 17774.

(158) Guoting, Q.; Zheng, L.; Rongmin, X.; Feng, L.; Brian, E. O. N.; Jessica, T. G.; Htet, A. K.; Wah, C.; King, C. L. *Nanotechnology* **2011**, *22*, 155605.